Determination of the CKM matrix element $|V_{cb}|$ from exclusive $B^0 \to D^{*-}\ell^+\nu_\ell$ decays with the Belle experiment

Author:

Eiasha Waheed

A thesis submitted in fulfilment of the requirements

for the degree of Doctor of Philosophy (Physics)

in

Experimental Particle Physics

School of Physics

Abstract

The magnitude of of the CKM matrix element $|V_{cb}|$ is determined based on the exclusive semileptonic $B^0 \to D^{*-}\ell^+\nu_\ell$ decay with data from the Belle experiment at KEKB. Two different parameterisations of the hadronic transition form factors are used in the extraction of the form factor parameters and $\mathcal{F}(1)|V_{cb}|\eta_{\rm EW}$. We find that the commonly used model dependent Caprini-Lellouch-Neubert form factor parameterisation yielded $|V_{cb}|$ results 10% lower than the model independent Boyd-Grinstein-Lebed approach. The latter are in good agreement with the inclusive approach for the determination of $|V_{cb}|$, suggesting the long standing inclusive-exclusive tension may be solved. The branching fraction of $B^0 \to D^{*-}\ell^+\nu_\ell$ decays and the lepton universality ratio $\mathcal{B}(B^0 \to D^{*-}e^+\nu_e)/\mathcal{B}(B^0 \to D^{*-}\mu^+\nu_\mu)$ are also measured. Results compatible with the world average for the former, and with the SM for the latter are found. This thesis presents the most precise measurements of $B^0 \to D^{*-}\ell^+\nu_\ell$ and exclusive $|V_{cb}|$ ever performed.

Declaration

This is to certify that:

- this thesis comprises only my original work towards the PhD except where indicated,
- due acknowledgement has been made in the text to all other material used,
- the thesis is less than 100,000 words in length, exclusive of tables, bibliographies and appendices.

Eiasha Waheed

Preface

In recent years, accomplishments in experimental particle physics have been the result of increasingly large international scientific collaborative efforts as in Belle experiment. As a result of these collaborative undertakings, it is incredibly rare that any substantial body of work is done in isolation. The standard procedure is to work in groups, each carrying out a specific purpose within the wider collaboration such as data acquisition, detector monitoring and development, particle reconstruction and event simulation. All these activities represent essential inputs to any scientific measurement in Belle. The results presented in this thesis are detailed here.

Chapters 1 and 2 and 4 are original reviews of CKM flavour theory.

Chapter 3 is an original investigation of theoretical form factor parameterisations for semileptonic B decays, forming the basis for the personal work of the author.

Chapter 4 is an original review of new physics contributions to tree level semileptonic B decays.

Chapter 5 is a summary of the Belle experiment, with extracts from a number of public results about the Belle detector design and performance.

The author's original work is described in Chapters 6 to 10 which illustrate the work of the author conducted within the Belle collaboration under the supervision of Dr. Phillip Urquijo. Unless specifically stated, all the information provided these chapters and the scientific results represent original work of the author.

Acknowledgements

First and foremost, my deep gratitude to my supervisor Phillip Urquijo for his valuable advice, positive attitude and selfless facilitation that kept me going through the challenging phases of my PhD. It would not have been possible without his constant support and encouragement. His extensive expertise in the research field aided me to grow as a researcher. I am grateful to my second supervisor Elisabetta Barberio for her persistent support, encouragement and motivation. Her constructive suggestions have not only inspired me during the demanding thesis writing phase but also to be a better person with positive attitude in future.

I would like to pay my special thanks to my fellow colleagues Laurence Spiller, Marco Milesi, Brian Le, Chialing Hsu, Giacomo Cario, Francesco Nuti, Millie McDonald, Tristan Bloomfield, and Chunhua Li in Physics for enabling me to share concerns and worries with them.

Special thanks go to Geoffory Taylor for giving me the chance to join the outstanding particle physics community at the University of Melbourne in the CoEPP group. I wish to acknowledge the help provided by the administrative and technical staff of my department especially Lucien Boland and Sean Crosby. I highly appreciate their collective efforts for making the work environment a suitable place to work.

Last but not the least, I would like to acknowledge my parents' (Abu and Ami) lifelong efforts to create those facilitating circumstances that paved the challenging phases of my educational career (and my life in general) and brought me to the University of Melbourne for a PhD. The words of appreciation cannot express how much grateful I am to my elder brother Bilal Waheed for his immense support. I am thankful to my brothers Qasim Abbas and Shamim Haider and my sisters Asma Qasim and Zubaida Butt for being my strength regardless of where I am and what I am doing.

Contents

List of Figures

List of Tables

1. Introduction

The Standard Model of particle physics is a theory that describes the properties and the interactions of fundamental particles. Although it is very successful, it is incomplete. It fails to account for most of the mass in the universe called the dark matter, which is inferred from observations in astrophysics. It also fails to account for non-zero neutrino masses, which are implied by neutrino oscillation experiments. Even within the domains of its applicability, it has about two dozen free parameters to be determined by experiment. Quantitative tests of the Standard Model, as well as the searches for physics beyond the standard model, require precise knowledge of these parameters. This thesis address the determination of one of these parameters. In the Standard Model, there are three families of fundamental matter particles. The second and the third families are more massive partners of the first. The families are differentiated by a quantity called "flavour". Among the fundamental interactions described by the Standard Model, only the charged weak interaction can change flavour. The flavour changing interaction produces many phenomena like for example Charge-Parity symmetry violation. In the quark sector these phenomena are described by a complex 3×3 CKM matrix in the Standard Model. This matrix mixes the different flavours of quarks and can accommodate the violation of CP symmetry with a complex phase.

In this thesis we will study the transition of a b-quark to a c-quark, in B meson decay. There are experimental facilities which are built to investigate the properties of the B mesons. Two prominent examples are the Belle experiment at KEK (High Energy Accelerator Research Organization, Tsukuba, Japan) and LHCb at CERN, Geneva. KEKB is called a B-factory because as it produce B mesons with high rate near the kinematic threshold for production with no additional particles in the event.

The primary targets of B-factories are to quantitatively determine the mechanism of CP-violation in B meson decay and mixing, and to measure the fundamental parameters of the Standard Model related to B physics with high precision. In this thesis, we are interested in semileptonic B decays of the type $B \to X_c \ell \nu$, where ℓ is an electron or a muon, ν is a neutrino and X_c is a hadronic system including a charm quark. Details of these particles and semileptonic decays are explained in chapter 3. The main features of these decays are

- They are experimentally accessible and theoretically clean;
- They can be used to extract one of the fundamental parameters of the Standard Model,$|V_{cb}|$;
- They can be used to study deviation from the Standard Model expectation, due to new types of weak interactions.

2. Theory

The Standard Model (SM) of particle physics is a coherent theory of nature at the fundamental level and it is the best human effort that explains all the fundamental constituents of matter and their interactions. The SM describes the interactions between elementary quarks and leptons (matter particles) and three of the fundamental forces (weak, strong and electromagnetic) using a gauge group $SU(3)_C \times SU(2)_L \times U(1)_Y$. The $SU(3)$ part describes the strong interaction while the $SU(2)_L \times U(1)_Y$ part corresponds to the electroweak interaction. The matter particles (quarks and leptons) are spin 1/2 fermions, while the force carriers (photon, gluons, Z^0 and $W^{\pm}$) are spin 1 bosons. Every particle has an associated anti-particle which has the same mass but opposite quantum number such as charge. The Higgs is responsible for particles' mass and is a scalar, hence it has spin 0. The known matter particles described by the SM are listed in Table 2.1.

Table 2.1: Leptons and Quarks in the Standard Model.

		Name	Symbol	Charge (e)	Mass (MeV/c^2)
First generation	Quark	Up	u	$+\frac{2}{3}$	$1.5 - 3.3$
		Down	d	$-\frac{1}{3}$	$3.5 - 6.0$
	Lepton	Electron	e	-1	0.511
		Electron neutrino	ν_e	0	< 0.0000022
Second generation	Quark	Charm	c	$+\frac{2}{3}$	$1160 - 1340$
		Strange	s	$-\frac{1}{3}$	$70 - 130$
	Lepton	Muon	μ	-1	105.7
		Muon neutrino	ν_μ	0	< 0.17
Third generation	Quark	Top	t	$+\frac{2}{3}$	$169100 - 173300$
		Bottom	b	$-\frac{1}{3}$	$4130 - 4370$
	Lepton	Tau	τ	-1	1777
		Tau neutrino	ν_τ	0	< 15.5

2.1 Strong Interactions

Quantum Chromodynamics (QCD) is the quantum theory of the strong interaction between quarks. Strong interactions are mediated by massless gluons, which couple to the 'strong' charge. Since quarks are the only fundamental particles with nonzero 'strong' charge, these are the only particles to feel the strong interaction – leptons do not interact via the strong interaction. The strong interaction charge is called the colour charge. Colour is a conserved quantum number with three values, labeled red, green and blue. Quarks are said to carry a colour (r, g or b), while anti-quarks are said to carry an anti-colour (anti-r, anti-g and anti-b). As mentioned earlier, strong interactions have the group structure, $SU(3)_c$ in which c denotes the colour of the quarks and gluons. Experimentally, we have never observed a free quark or gluon, they are always confined within hadrons. Confinement is an important feature in QCD. The confinement of gluons and quarks is a consequence of the very nature of the strong interaction, but there is no direct and straightforward explanation. The effect of confinement is to make all coloured particles bound into states that have no net colour. They are either colourless (a combination of a colour and an anti-colour) or white (a combination of red, green and blue). B mesons are an example of the colourless states, being mesons (composed of a quark-antiquark pair) and protons and neutrons are examples of white states, being baryons (composed of three quarks). Quarkonia are flavourless mesons consisting of a quark and anti-quark of the same flavour, for example the $\Upsilon(4S)$ is bound states of bottom and anti-bottom quarks. A B^0 meson consists of d and $\bar{b}$ (anti-b) quarks, and a B^+ meson is made of u and $\bar{b}$ quarks. A proton is a baryon and is made of two u quarks and one d quark. Baryons and mesons are both called hadrons. As quarks are confined in hadrons, all fundamental particles we can isolate are divided into two categories: leptons and hadrons.

2.2 Electroweak Interaction

Every fundamental particle of the Standard Model feels the weak interaction. Electromagnetic and weak interactions are unified into electroweak interactions, whose group structure is $SU(2) \times U(1)_Y$. The Y represents the weak hypercharge, and the charge of $SU(2)$ is the weak isospin. Weak hypercharge and weak isospin are not conserved because the $SU(2) \times U(1)_Y$ symmetry is broken. The only conserved charge is the electric charge. There are two types of weak interactions: neutral weak interactions, which are mediated by Z^0 and charged weak interactions, which are mediated by $W^{\pm}$. The mass of the $W^{\pm}$ bosons are $80.40\text{GeV}/c^2$, and the mass of the Z^0 is $91.2\text{GeV}/c^2$, the photon is massless. The processes in which a $W^{\pm}$ boson is emitted or absorbed are the only ones in which a quark's flavour may be changed. In fact the appearance of a $W^{\pm}$ boson is always related to the creation or loss of a quark and differently charged anti-quark, or of a lepton and neutrino (or their anti-particle counterparts). The charged weak interaction is the only fundamental interaction that does not conserve flavour and CP symmetry.

2.3 The Cabibbo-Kobayashi-Maskawa (CKM) matrix

Charged weak interactions, allows for quarks to swap their flavour for another, i.e. a up-type quark can transform into a down-type quark. This happens because the weak eigenstates and the mass eigenstate do not coincide. The left-handed fermions transform as weak $SU(2)_L$ doublets where the right handed components anti-fermion transform as weak singlets $SU(2)_L$.

$$Q_L^i = \begin{pmatrix} u_L^i \\ d_L^i \end{pmatrix}, L_L^i = \begin{pmatrix} \nu_L^i \\ e_L^i \end{pmatrix}, H^0, \tag{2.1}$$

and

$$u_R^i, d_R^i, e_R^i, \tag{2.2}$$

where the index i represents the three fermion generations. The couplings of quarks and leptons for $SU(2)_L$ and the couplings of right handed singlets are given by the Lagrangian [10],

$$\mathcal{L}_{Yukawa} = -g_u^{i,j}\bar{u}_R^i\langle H^0\rangle u_L^i - g_d^{1,j}\bar{d}_R^j\langle H^0\rangle d_L^j - g_e^{i,j}\bar{e}_R^i\langle H^0\rangle e_L^i. \tag{2.3}$$

The mixing matrix is formed by applying the unitarity transformation on the two components of each $SU(2)_L$ doublet, acting on the three generation of quarks in the Cabibbo Kobayashi Maskawa (CKM) mixing matrix i.e. $V_{CKM} = U_u^\dagger U_d$:

$$\begin{pmatrix} d' \\ s' \\ b' \end{pmatrix} = \begin{pmatrix} V_{ud} & V_{us} & V_{ub} \\ V_{cd} & V_{cs} & V_{cb} \\ V_{td} & V_{ts} & V_{tb} \end{pmatrix} \begin{pmatrix} d \\ s \\ b \end{pmatrix} \tag{2.4}$$

The states denoted with prime are the weak eigenstates and the states without the prime are the mass eigenstates of the down type quark, where V_{CKM} denotes the strength of the coupling. The flavour transition from one generation of an up-type quark to another generation down-type quark is a measure of probability, which is proportional to square of the magnitude of the CKM matrix element $|V_{qq'}|^2$. The CKM matrix elements are fundamental parameters of the Standard Model and cannot be predicted.

Most values of the CKM matrix element magnitudes are measured directly with tree level processes. The magnitude of the CKM element V_{cb} is measured from the tree level process of b to c decay while V_{td} is determined indirectly from the mixing oscillation frequency of $B_d - \bar{B}_d$ using loop diagrams, as shown in Figure 2.1.

The bottom quark transformation into a charm quark and a electron electron-neutrino pair via a weak W boson is an example of a charged current interaction. This transition is written in terms of CKM matrix elements as:

$$s' = V_{cd}d + V_{cs}s + V_{cb}b. \tag{2.5}$$

Here the b quark couples to the weak eigenstate of the quark in the same family, s',

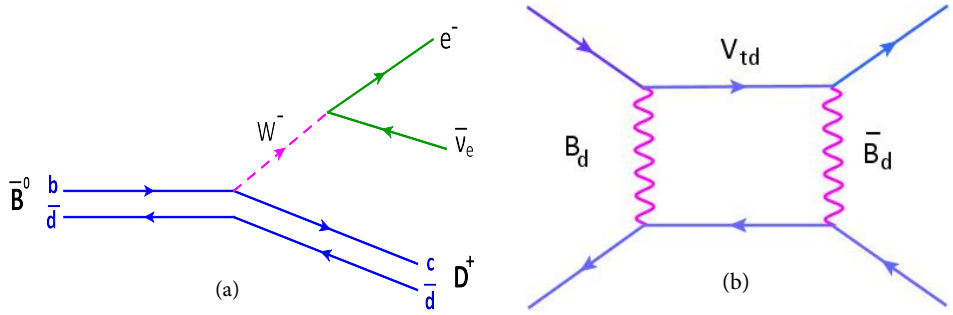

Figure 2.1: A tree level $b \to c$ diagram with V_{cb} dependence (left) and a loop level mixing diagram with V_{td} and V_{tb} dependence (right).

when the W boson interacts with the c quark. Thus the amplitude of this decay is proportional to only one CKM matrix element V_{cb}. When the amplitude of the decay does not change under CP transformation, the elements of the CKM matrix are real, the imaginary phase appearing in the CKM matrix is responsible for CP violation. CP asymmetry is suppressed in the case of meson mixing.

2.3.1 Parameterisation of the (CKM) Matrix

The CKM matrix is a complex 3×3 matrix consisting of 18 real parameters. The unitarity condition imposes 3^2 constraints. Furthermore, the rotations of quark fields removes 5 phases. Hence the total independent parameters are four. So, the CKM matrix can be parameterised using 4 parameters that includes three real parameters and one complex phase. In the matrix, the diagonal elements are almost equal to one where as the off diagonal elements are very small. There are many parameterisations of the CKM matrix. The most commonly used is the Wolfenstein parameterisation, that at third order in λ (Cabibbo mixing angle) is denoted as [11],

$$V_{CKM} = \begin{pmatrix} 1 - \frac{\lambda^2}{2} & \lambda & A\lambda^3(\bar{\rho} - i\eta) \\ -\lambda & 1 - \frac{\lambda^2}{2} & A\lambda^2 \\ A\lambda^3(1 - \bar{\rho} - i\bar{\eta}) & -A\lambda^2 & 1 \end{pmatrix} + \mathcal{O}(\lambda^4), \tag{2.6}$$

This parametrisation is an expansion in the powers of λ, A, ρ, and η. The CKM matrix element $|V_{cb}|$ is related to λ as $A\lambda^2 = |V_{cb}|$. It is common to express $\bar{\rho}$ and $\bar{\eta}$

in terms of A and λ,

$$\bar{\rho} = \rho\left(1 - \frac{\lambda^2}{2}\right), \bar{\eta} = \eta\left(1 - \frac{\lambda^2}{2}\right), \tag{2.7}$$

The complex phase is a representation of CP violation.

2.3.2 Unitarity Conditions of the CKM Matrix

The CKM is a unitarity matrix , which means that all elements in the matrix are related by the following relations

$$\sum_i V_{ij} V_{ik}^* = \delta_{jk}, \tag{2.8}$$

$$\sum_j V_{ij} V_{kj}^* = \delta_{ik}. \tag{2.9}$$

In the complex plane, this unitarity condition can be expressed as triangles. The area of these triangles is proportional to the amount of CP violation. The more significant triangles from the experimental point of view are those where the sides are of similar length, e.g. in the Wolfsentein parameterisation same order of λ, gives following relations

$$V_{ud} V_{ub}^* + V_{cd} V_{cb}^* + V_{td} V_{tb}^* = 0. \tag{2.10}$$

$$V_{ud} V_{td}^* + V_{us} V_{ts}^* + V_{ub} V_{tb}^* = 0. \tag{2.11}$$

Taking Equation 2.10, to make $(V_{cd}V_{cb})$ real, a phase convention is chosen by dividing it with $|V_{cd}V_{cb}^*|$, which normalises one of the sides of the triangle as shown in Figure 2.2. The vertices of this normalised triangle are $(0, 0)$, which is fixed, and vertices $(0, 1)$ in the $(\bar{\rho}, \bar{\eta})$ plane which are determined experimentally. The angles of this triangle are as defined as follows

$$\phi_1 \equiv \beta = \arg\left[- \frac{\mathrm{V_{td}V_{tb}^*}}{\mathrm{V_{ud}V_{ub}^*}} \right], \tag{2.12}$$

$$\phi_2 \equiv \alpha = \arg\left[- \frac{\mathrm{V_{cd}V_{cb}^*}}{\mathrm{V_{td}V_{tb}^*}} \right], \tag{2.13}$$

$$\phi_3 \equiv \gamma = \arg\left[- \frac{\mathrm{V_{ud}V_{ub}^*}}{\mathrm{V_{cd}V_{cb}^*}} \right]. \tag{2.14}$$

To test the consistency of the Standard Model both the sides and the the angles

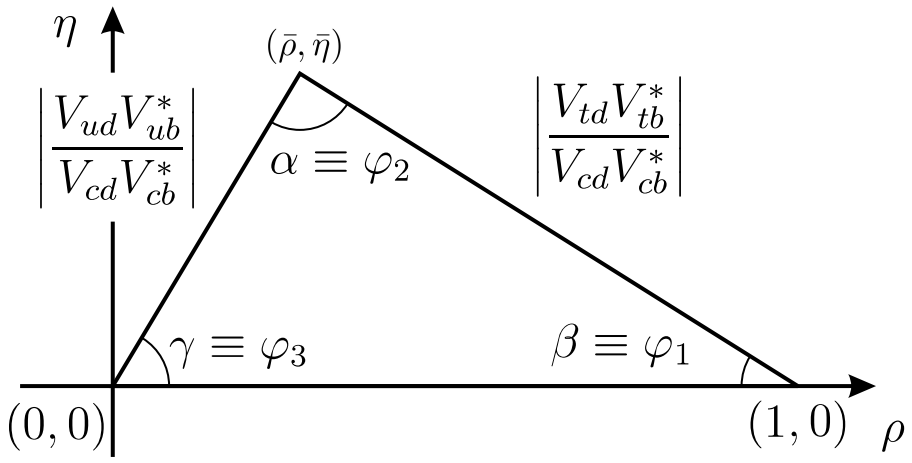

Figure 2.2: Normalised Unitarity Triangle.

of the unitary triangles need to be measured. The decays of B mesons can be used to measure both the sides and the angles. The CKM matrix elements $|V_{cb}|$ and $|V_{ub}|$ are extracted from tree level processes. $|V_{cb}|$ is extracted with greater precision as it is a more abundant process, whereas $|V_{ub}|$ is the smallest of the CKM elements and more challenging to experimentally extract. The consistency of CKM measurements with the expectation of the SM is done by performing a global fit that combines measurements from different B, D, K and τ decay processes constraining the the unitarity triangle as shown in Figure 2.3.

The precise determination of the angle β sets tight constraints on the measurement of the side of the triangle opposite the angle. These experimental results require input from lattice QCD calculations since the precision of matrix elements $|V_{cb}|$ and $|V_{ub}|$ depends on precise determination of hadronic transition form factors [12]. In the next chapter, the theory behind the determination $|V_{cb}|$ is discussed for the measurement based on exclusive decays of the B meson. In this thesis, the measurement of CKM matrix element $|V_{cb}|$ is presented, as well as some tests of lepton flavour universality and CP symmetry in semileptonic B decays. The latter are generally considered sub-sample cross-checks of the main $|V_{cb}|$ analysis.

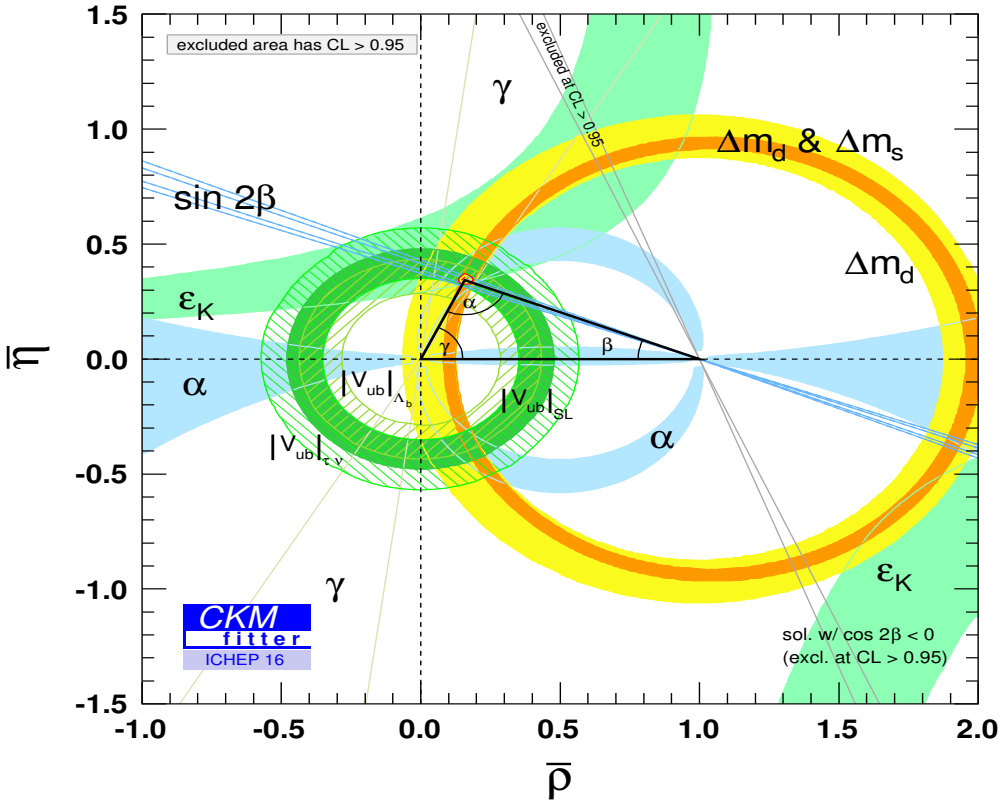

Figure 2.3: Constraints on the unitarity triangle by different measurements by CKM-Fitter 2016 [1]

3. Exclusive Semileptonic decays of Mesons

Decays of B mesons are instrumental in flavour physics as they can be used to address many fundamental questions of particle physics, such as the amount of CP violation in quark interactions, and the value of of CKM matrix elements. B mesons are made of a b-quark and a light anti-quark (u or d) whereas a $\bar{B}$ meson is made up of charge conjugated quarks. B mesons can be produced at B factories, such as Belle and BaBar, at centre-of-mass energies near the mass of the $\Upsilon(4S)$ (10.58 GeV) resonance. B factories produce a large number of B meson pairs that are used to understand the properties of b quark transitions. We can classify the B meson weak decays as follows:

- Leptonic decays
- Semileptonic decays
- Non-leptonic decays (hadronic and radiative decay)

Here, we will focus on semileptonic B decays. While all processes depend on the CKM matrix element in the corresponding weak decay, they vary in their theoretical and experimental cleanliness. While leptonic decays are theoretically very clean, they are helicity suppressed and therefore statistics limited at B-factories. Non-leptonic decays are abundant, but the rates depend on strong interaction effects that are difficult to theoretically predict. Semileptonic decays are abundant, and due to the presence of only one hadronic current, they are precisely calculable.

The decay rates of $b \to c\ell\nu$ semileptonic decays are proportional to $|V_{cb}|^2$ (ℓ

denotes both electrons and muons). Two different methods have been used to extract this parameter from data: the exclusive measurement, where $|V_{cb}|$ is extracted by studying $B \to D^*\ell\nu$ or $B \to D\ell\nu$ decay processes; and the inclusive measurement, which uses the semileptonic width of b-hadron decays ($BtoX\ell\nu$). Theoretical estimates play a crucial role in extracting $|V_{cb}|$, and an understanding of their uncertainties is very important.

The inclusive method requires measurements of the B lifetimes and the semileptonic branching fraction $Br(B \to X_c\ell\nu)$ [13]. In this case, quark-hadron duality bridges the gap between theoretical calculations and experimental observables [14]. The modern theoretical formulation based on the Operator Product Expansion (OPE) determines the inclusive decay amplitudes in inverse powers of $1/m_Q$ [15]. Non-perturbative corrections to the leading term, given by the spectator decay amplitude, arise only to order $1/m_b^2$.

The exclusive method is obtained studying $B \to D^*\ell\nu$ or $B \to D\ell\nu$ decays, shown in Figure 2.1. Heavy Quark Effective Theory (HQET), an exact theory in the limit of infinite quark masses is used to relate the rate measurements to $|V_{cb}|$. Currently, the $B \to D\ell\nu$ transition provides a less precise value, due to large feed-down background from $B \to D^*\ell\nu$, and is used primarily as a check. In using HQET, we take a full theory process of interest and expand in terms of the local operators, using the effective theory formalism. The resulting theoretical description for a particular process of interest is expressed in terms of matrix elements of these local operators.

3.1 Heavy Quark Effective Theory (HQET)

Heavy Quark Effective Theory (HQET), is an exact theory in the limit of infinite quark masses. Light quarks (u, d, s) have masses that are small compared to the scale of non-perturbative strong dynamics. In the limit $m_q \to 0$, QCD has an unbroken $SU(3)_L \times SU(3)_R$ chiral symmetry, which can be used to predict the properties of hadrons containing light quarks. For quarks with masses m_Q greater than the scale of non perturbative strong dynamics (Λ_{QCD} [16, 17]) i.e. in the $m_q \to \infty$ limit, in the

leading approximation, the heavy quark is considered as a static source of the gluon field. In this limit, the light degrees of freedom are preserved, i.e. spin-flavour heavy quark symmetry [18], with important implications for calculations of the transitions of heavy quarks and to obtain relations among heavy hadron form factors. HQET also simplifies lattice simulation and sum rules analysis of heavy hadrons.

In HQET, the heavy quark behaves like a static external source of colour charge that transforms as a colour triplet, and the meson dynamics reduces to that of light degrees of freedom interacting with this colour source. At leading order, the heavy quarks interact same way within heavy mesons. This is the only effective theory that provides a description of the transitions from the very high energy scale (100 GeV) of weak decays to the light meson energy scale of Λ_{QCD} [16, 17]. This is used to calculate the $b \to c$ transition in the case of semileptonic B decays. HQET maintains the light degree of freedom, i.e. the flavour symmetry and spin symmetry, which helps to reduce large hadronic uncertainties that arise due to the the lack of information we have for the QCD bound state problem. In HQET, a particular process of interest is expressed in terms of matrix elements of operators that are derived from an effective theory formalism. In the next section, $(b \to c)$ processes are explained in terms of their decay amplitudes. Also, the expansion of $1/m_Q$ is formulated as an effective field theory which enables us to use the corrections to the mass limit of the quark. Therefore, in semileptonic B decays ($b \to c$ transition), the heavy quark symmetries work effectively for the heavy B meson and the D meson (using a $1/m_Q$ expansion in a model independent manner) and will allow us to determine the CKM matrix element $|V_{cb}|$. The spin-flavour symmetry is exhibited at the leading order and is broken by terms of order $(\lambda_{QCD}/m_Q)^n$ when $n \geqslant 1$.

3.2 Decay Amplitude for $(b \to c)$ and Shape Functions

The semileptonic $\bar{B}$ meson decay amplitude is calculated from the matrix elements of the weak Hamiltonion:

$$\mathcal{M} = -i\frac{G_F}{\sqrt{2}}V_{cb}L^{\mu}H_{\mu}, \tag{3.1}$$

where L^{μ} is the leptonic current, G_F is the Fermi constant, H_{μ} is the hadronic current and the μ is the Lorentz invariant index. The leptonic current gives us the electroweak hyper charge from the lepton neutrino to the lepton (e, μ) whereas the quark current gives us the hadronic current from the b-flavour meson to the c-flavour meson.

Another representation for the leptonic current and the quark current is given by Dirac spinors as:

$$L^{\mu} = \bar{\mu_{\ell}}\gamma^{\mu}(1-\gamma_5)\mu_{\nu}, \tag{3.2}$$

$$H^{\mu} = \bar{c}\gamma^{\mu}(1-\gamma_5)b. \tag{3.3}$$

In the above equation, γ^{μ} and γ_5 are Dirac matrices of dimension 4. H^{μ} is the hadronic current where the quarks are confined in the hadrons and cannot be accessed separately. When momentum transfer is large compared to $\lambda_{QCD} > 0.5$ GeV, the cross section of these strong interactions are calculated perturbatively.

The hadronic current can be given in terms of vector and axial-vector currents as:

$$H^{\mu} = \langle D|\bar{c}\gamma^{\mu}(1-\gamma_5)b|B\rangle = \langle D|V^{\mu}|B\rangle - \langle D|A^{\mu}|B\rangle \tag{3.4}$$

The matrix elements for the vector and axial vector are written in terms of certain functions called form factors. Thus, the matrix elements for $B \to D^*\ell\nu$ decays is given by

$$\langle D^*(p^{'})|V^{\mu}|B(p)\rangle = f_+(p+p^{'})^{\mu} + f_-(p-p^{'})^{\mu}, \tag{3.5}$$

$$\langle D^*(p^{'})|A^{\mu}|B(p)\rangle = 0, \tag{3.6}$$

where $V^\mu = \bar{c}\gamma^\mu b$ is the vector current, $A^\mu = \bar{c}\gamma^\mu\gamma_5 b$ is the axial-vector current and $f_\pm$, are form factors. These form factors are calculated with HQET due to the quark content of B and D^* mesons. It follows that the effective Hamiltonian is,

$$\mathcal{H}_{\text{eff}} = \frac{G_F}{\sqrt{2}} \sum_{q=c} V_{cb}(\bar{q}\gamma_\mu(1-\gamma_5)b)\ (\ell\gamma^\mu(1-\gamma_5)\nu_\ell). \tag{3.7}$$

The CKM matrix element is directly measured from the differential decay rate,

$$d\Gamma \propto G_F^2|V_{cb}|^2|L^\mu\langle X|\bar{q}\gamma_\mu P_L b|B\rangle|^2. \tag{3.8}$$

Semileptonic B decays are comprised of leptonic and hadronic currents, however the leptonic current and the matrix element $|V_{cb}|$ factorise from the hadronic part. The hadronic matrix element is described with form factors from QCD, which are functions of the hadronic recoil. Along with the QCD effects, electromagnetic corrections must be taken into account for the measurement of $|V_{cb}|$. In the case of $B^0 \to D^{*-}\ell^+\nu_\ell$ decays, both the vector and axial-vector currents contribute. In Equation 3.8, the transition matrix element of the weak current is integrated in terms of a Lorentz invariant form. For the vector final state D^* we have,

$$\begin{aligned}\langle V|\,\bar{q}\gamma^\mu\gamma^5 b|\bar{B}\rangle = i\epsilon_v^*\Bigg[A_0(q^2)\frac{2mvq^\mu q^\nu}{q^2} + A_1(q^2)(m_B+m_v)\eta^{\mu\nu} \\ -A_2(q^2)\frac{(p_B+p_V)\sigma q^\nu}{(m_B+m_V)}\eta^{\mu\nu}\Bigg],\end{aligned} \tag{3.9}$$

where ϵ_ν is the polarisation vector of the vector meson, $\eta^{\mu\nu}$ is the Levi-Civita tensor and V, A_i are the traditional form factors of HQET. The determination of form factors is important in order to calculate the decay rate and the kinematic variables. These form factors describe the strong part of the decay, and hence the recoil of the quarks in the D^* meson. Therefore, if the recoil velocity of D^* is smaller it implies that the momentum transfer between the B and D^* mesons is maximised. The quark model which can be used for $B^0 \to D^*\ell\nu$ decays is called the Isgur-Wise (ISGW) model [19]. From the $\bar{B} \to D^*\ell\nu_\ell$ semileptonic decay, q^2 is not small compared with $m_{c,b}^2$. However, q^2 does not determine the typical momentum transfer to the light

degrees of freedom. An approximate measure of that is the momentum transfer that must be given to the light degrees of freedom so that they recoil with the D^*. The light degrees of freedom in the initial and final hadrons have momentum of order $\lambda_{\rm QCD}\ v$ and $\lambda_{\rm QCD}\ v^{'}$, respectively, since their velocity is fixed to be the same as the heavy quark velocity. The momentum transfer for the light system is then $q^2_{\rm light} \sim (\lambda_{\rm QCD} v - \lambda_{\rm QCD} v^{'})^2 = 2\lambda^2_{\rm QCD}(1-w)$. Heavy quark symmetry should hold, provided

$$2\lambda^2 a_{\rm QCD}(w-1) << m^2_{b,c}. \tag{3.10}$$

The calculations performed in the ISGW quark model provide the matrix elements of the hadronic form factors for a particular value of the recoil w i.e. $w = 1$ or $w = w_{max}$. The ISGW model is based on the assumption of the non-relativistic quark potential model. The HQET model has consistently corrected the heavy quark limit of Quantum Field Theory (QFT). The HQET form factors are related to vector and axial-vector form factors by

$$A_2(w) = \frac{R_2(w)}{R^{*2}}\frac{2}{w+1}A_1(w), \tag{3.11}$$

$$V(w) = \frac{R_1(w)}{R^{*2}}\frac{2}{w+1}A_1(w), \tag{3.12}$$

$$h_{A_1}(w) = \frac{1}{R^*}\frac{2}{w+1}A_1(w), \tag{3.13}$$

where $R_1(w)$ and $R_2(w)$ are the ratios of a set of form factors ($h_V(w)$, $h_{A_1}(w)$, $h_{A_2}(w)$, $h_{A_3}(w)$) written as

$$R_1(w) = \frac{h_V(w)}{h_{A_1}(w)}, \tag{3.14}$$

$$R_2(w) = \frac{h_{A_3}(w) + r h_{A_2}(w)}{h_{A_1}(w)} \tag{3.15}$$

and

$$r = \frac{m_{D^*}}{m_B}, \tag{3.16}$$

$$R^* = \frac{2\sqrt{m_B m_{D^*}}}{(m_B + m_{D^*})}. \tag{3.17}$$

The spin-flavour symmetry of heavy quark effective theory can be used to derive relations between the form factors h_{A_1}, h_V and h_{A_2}. A transition to heavy quark effective theory is possible provided the typical momentum transfer to the light degrees of freedom is small is compared to the heavy quark masses. The heavy meson form factors are expected to vary on the scale $q^2_{light} \sim \lambda^2_{QCD}$, i.e. on the scale $w \sim 1$.

3.3 Parameterisation of the Form Factors

In B mesons the high mass of the b quark means that HQET [20] provides a valid expansion for describing the approximate decoupling of the b quark from the rest of the meson. This leads to a considerable simplification of the strong-interaction dynamics. Semileptonic decays of b-hadrons are particularly tractable from the theoretical point of view, since the leptonic current may be trivially separated from the hadronic current. Exclusive processes must be described in terms of a number of non-perturbative form factors that encapsulate the physics of the hadronisation process. These form factors possess a well-defined normalisation at zero recoil. In $B \to D^*$ transitions, the form factor appearing in the hadron wave function is proportional to a single form factor which is function of momentum transfer [20, 21]. QCD sum rules restrict the slope and magnitude of these form factors [21, 22] but they are predominantly undetermined. In the case of $B \to D^*$ transitions, the combinations of form factors most easily obtained from data appear as a sum of squares in the differential rates as the helicity amplitudes.

The $B^0 \to D^* \ell \nu_\ell$ decay amplitude can be expressed in terms of three physically intuitive amplitudes (H_+, H_- and H_0), which correspond to the three allowed polarisation states of the D^* (two transverse states and one longitudinal state). These

amplitudes are related to the axial and vector form factors as follows:

$$H_+(w) = -(m_B + m_{D^*})A_1(w) + 2\frac{p_{D^*} m_B}{m_B + m_{D^*}} V(w), \tag{3.18}$$

$$H_-(w) = -(m_B + m_{D^*})A_1(w) - 2\frac{p_{D^*} m_B}{m_B + m_{D^*}} V(w), \tag{3.19}$$

$$H_0(w) = -\frac{1}{2m_{D^*}\sqrt{w}}[A_1(w)(m_B + m_{D^*})(m_B^2 - m_{D^*}^2 - w) - 4\frac{m_B^2 + p_{D^*}^2}{m_B + m_{D^*}} A_2(w)]. \tag{3.20}$$

Constraints on a generic $B \to D^* \ell \nu_\ell$ form factor $\mathcal{F}(w)$ are obtained by noting that the amplitude for production of $B \to D^*$ from a virtual W boson is determined by the analytic continuation of $\mathcal{F}(q^2)$ from the semileptonic region of momentum-transfer $m_\ell \leq q^2 \leq (m_B - m_{D^*})^2$ to the pair-production region $(m_B + m_{D^*})^2 \leq (m_B - m_{D^*})^2$. The dispersion relation constrains $\mathcal{F}(q^2)$ in the region where B and D^* are created using perturbative QCD, and one then uses analyticity to translate that constraint into one valid in the semileptonic region [23]. Generating a parameterisation for a particular form factor requires three ingredients, the perturbative evaluation of the dispersion relations derived from the two-point function for a $(V - A)$ current. The computation of the functional form of the weighting function ϕ and the masses of sub-threshold resonances with the same quantum numbers as $(V - A)$ must be extracted from experiment or potential models. The function ϕ depends on the form factor under consideration, while dispersion relations depend only on the $(V - A)$ current.

3.3.1 BGL Parameterisation of the Form Factors

The parameterisation obtained by Boyd, Grinstein and Lebed (BGL) [24] follows from dispersion relations, analyticity, and crossing symmetry. In the case of semileptonic B decays q^2 ranges from m_ℓ^2 to $(m_B - m_{D^*})^2$ but the form factors can be continued analytically in the q^2 plane. They have a cut at $q^2 = (m_B - m_{D^*})^2$ and various poles corresponding to B_c resonances with the appropriate quantum numbers. The

helicity amplitudes are given by

$$H_0(w) = \frac{\mathcal{F}(w)}{\sqrt{q^2}}, \tag{3.21}$$

$$H_\pm(w) = f(w) \mp m_B m_{D^*}\sqrt{w^2-1}\,g(w). \tag{3.22}$$

These form factors ($\mathcal{F}(w)$, $g(w)$, $f(w)$) are written as a series in a z expansion,

$$f(w) = \frac{1}{P_{1^+}(w)\phi_f(w)}\sum_{n=0}^{N} a_n^f z^n, \tag{3.23}$$

$$\mathcal{F}_1(w) = \frac{1}{P_{1^+}(w)\phi_{\mathcal{F}}(w)}\sum_{n=0}^{N} a_n^{\mathcal{F}_1} z^n, \tag{3.24}$$

$$g(w) = \frac{1}{P_{1^-}(w)\phi_g(w)}\sum_{n=0}^{N} a_n^g z^n. \tag{3.25}$$

where z is defined as,

$$z = \frac{\sqrt{w+1}-\sqrt{2}}{\sqrt{w+1}+\sqrt{2}}, \tag{3.26}$$

and a is the coefficient of the expansion. The series is presumed to be truncated at $N = 2$ for accurate determination of $|V_{cb}|$, beyond which experimental data cannot easily constrain the expansion parameters. $P_{1\pm}$ are the Blaschke factors and are given as

$$P_{1\pm}(z) = \prod_{p=1}^{n}\frac{z-z_p}{1-zz_p}, \tag{3.27}$$

where

$$z_p = \frac{\sqrt{t_+ - m_p^2}-\sqrt{t_+-t_-}}{\sqrt{t_+ - m_p^2}+\sqrt{t_+-t_-}}, \qquad \text{and} \qquad \mathrm{t_\pm} = (\mathrm{m_B} \pm \mathrm{m_{D^*}})^2. \tag{3.28}$$

The outer functions ϕ_i for $i = g$, f, $\mathcal{F}_1$ are

$$\phi_g(z) = \sqrt{\frac{n_I}{3\pi\tilde{\chi}_{1^-}^T(0)}}\frac{2^4 r^2(1+z)^2(1-z)^{\frac{1}{2}}}{[(1+r)(1-z)+2\sqrt{r}(1+z)]^4}, \tag{3.29}$$

$$\phi_f(z) = \frac{4r}{m_B^2}\sqrt{\frac{n_I}{3\pi\chi_{1^-}^T(0)}}\frac{(1+z)(1-z)^{\frac{3}{2}}}{[(1+r)(1-z)+2\sqrt{r},(1+z)]^4}, \tag{3.30}$$

$$\phi_{\mathcal{F}_1}(z) = \frac{4r}{m_B^3}\sqrt{\frac{n_I}{6\pi\chi_{1^-}^T(0)}}\frac{(1+z)(1-z)^{\frac{5}{2}}}{[(1+r)(1-z)+2\sqrt{r}(1+z)]^5}, \tag{3.31}$$

where $\tilde{\chi}^T_{1^+}(0)$ and $\chi^T_{1^-}(0)$ are constants and n_I represents the number of light valence quarks also called isospin factors. The two form factors $f(0)$ and $\mathcal{F}_1(0)$ are related at the point of zero recoil $w = 1$,

$$\mathcal{F}_1(0) = (m_B - m_{D^*}) f(0). \tag{3.32}$$

The main advantage of the BGL parameterisation is that the parameters a_n of Equation 3.23 are constrained by unitarity conditions only,

$$\sum_{i=0} (a^g_n)^2 < 1, \tag{3.33a}$$

$$\sum_{i=0} [(a^f_n)^2 + (a^{\mathcal{F}_1})^2] < 1. \tag{3.33b}$$

The unitarity bounds of Equation 3.33a assume that the hadronic transition $B \to D^*$ saturates the so called weak unitarity bounds whereas heavy quark symmetry is used to connect the form factors and only amplitudes of fixed spin-parity enter each dispersion relation, leading to the strong unitarity condition in Equation 3.33b.

3.3.2 CLN Parameterisation of the Form Factors

The Caprini-Lellouch-Neubert (CLN) parametrisation [25] has been used in the literature extensively. It is based on dispersion relations and unitarity constraints. These unitarity bounds are implemented by exploiting HQET. The form factors of the two-meson states contributing to the two point function are related by heavy quark symmetry and in the heavy quark limit either vanish or are proportional to the Isgur-Wise function [19]. It also includes $\mathcal{O}(1/m)$ heavy quark symmetry breaking corrections, computed with input from light-cone sum-rules [26], and leading short distance corrections to these relations. The differential decay rate as a function of variable w is [25],

$$\begin{aligned} \frac{d\Gamma(B^0 \to D^{*-} \ell^+ \nu_\ell)}{dw} = & \frac{G_F^2 |V_{cb}|^2}{48\pi^3} (m_B - m_{D^*})^2 m_{D^*} \sqrt{w^2 - 1} (w+1)^2 \\ & \times \left[1 + \frac{4w}{w+1} \frac{m_B^2 - 2w m_B m_{D^*} + m_{D^*}^2}{(m_B - mD)^2} \right] |\mathcal{F}(w)|^2. \end{aligned} \tag{3.34}$$

where $\mathcal{F}(w)$ is the hadronic form factor. In the heavy-quark limit, $\mathcal{F}(w)$ coincides with the Isgur-Wise function, which describes the long-distance physics associated with the light degrees of freedom in the heavy mesons [27]. This function is normalised to unity at zero recoil, corresponding to $w = 1$. Corrections to this limit can be calculated using HQET [28]. Hence, $|V_{cb}|$ is obtained by by extrapolating the differential decay rates to $w = 1$ and unitarity constraints have been applied to establish approximate relations between the slope and the higher power coefficients of the the form factors to reduce the uncertainty associated with these form factors. At the point of zero recoil, the bounds on the form factors and their derivatives are obtained. The parameterisation of these Isgur-Wise function is given by

$$h_{A_1}(w) = h_{A_1}(1)[1 - 8\rho^2 z + (53\rho^2 - 15)z^2 - (231\rho^2 - 91)z^3], \tag{3.35}$$

$$R_1(w) = R_1(1) - 0.12(w - 1) + 0.05(w - 1)^2, \tag{3.36}$$

$$R_2(w) = R_2(1) + 0.11(w - 1) - 0.06(w - 1)^2, \tag{3.37}$$

and ρ^2 is the slope of the form factor. The important thing to remember is that the three experimental parameters we will be measuring in this analysis are the two helicity amplitude ratios $R_1(1)$, $R_2(1)$, and the slope ρ, which collectively are termed as the three "form factor" parameters. This condition essentially means that in the $B^0 \to D^*$ transition, the light quarks remain the same since the b and c quark are heavier and thus are dominant terms in the momentum transfer q^2. Hence the product of $|V_{cb}|$ and normalisation factor $\mathcal{F}(1)$ is extracted experimentally from the extrapolation of data at $w = 1$ in the B^0 rest frame. The corrections (including electroweak corrections) applied to the Heavy Quark Symmetry (HQS) limit gives [12]

$$\eta_{EW}\mathcal{F}(1) = 0.912 \pm 0.013, \tag{3.38}$$

where η_{EW} is the electroweak correction [29]. The expressions given in Equations 3.35, 3.36, and 3.37 contain three free parameters ρ^2, $R_1(1)$ and $R_2(1)$ which are not determined theoretically but rather from experiment using the fit. As long as the CLN parameterisation is used to describe the shape of a single form factor, like in

Equation 3.35, it provides a simple and effective parameterisation, unless of course the experimental or theoretical constraints reach the $\sim 1\%$ precision. HQS relates $B \to D^*$ form factors in such a way that they are proportional to the Isgur-Wise function or vanish (in heavy quark limit). In the CLN parameterisation the zero recoil value of the form factor parameters are calculated using experimental data whereas the BGL parameterisation does not utilise any assumptions from HQS. It might be possible to implement strong unitarity bounds using lattice calculations of different form factors, rather than HQET approximations only with the development of lattice QCD. The CLN parameterisation, which has been an important tool for the measurement of $|V_{cb}|$ and is subject of this thesis, may no longer be adequate to cope with the present accuracy of experiment and lattice calculations.

3.3.3 Determination of $|V_{cb}|$

The measurement of kinematic variables for the decay $B^0 \to D^*\ell\nu$ is crucial for the accurate measurement of the CKM matrix element $|V_{cb}|$. These include three angular variables, shown in Figure 3.1, and the hadronic recoil which is a function of the lepton system momentum transfer, q^2. They are defined as follows.

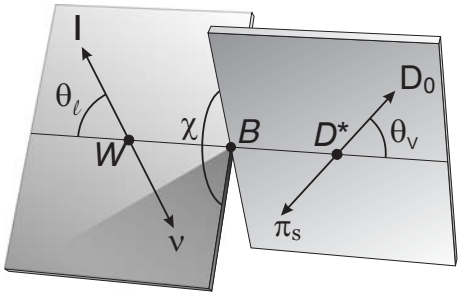

Figure 3.1: The definition of the angles θ_ℓ, $\theta_{\rm v}$ and χ for the decay $B^0 \to D^{*-}\ell^+\nu_\ell$.

- Recoil w: is a function of the momentum transfer q^2 between B^0 and D^* and is defined as the dot product of the four velocities, $\nu^\mu = p^\mu/m_B$ and ν'^μ/m_{D^*}, of the B^0 and D^* meson, respectively,

$$w \equiv v_B.v_{D^*} = \frac{P_B.P_{D^*}}{m_B m_{D*}} = \frac{m_B^2 + m_{D^*}^2 - q^2}{2m_B m_{D^*}}. \tag{3.39}$$

The allowed kinematic limit for w is found by setting $q^2 = 0$, thus

$$0 \leqslant w - 1 \leqslant \frac{(m_B - m_{D^*})}{2m_B m_{D^*}}. \tag{3.40}$$

At the point of maximum recoil ($w_{max} = 1.504$) and for zero recoil ($w = 1$) maximum momentum is transferred i.e. D^* is at rest in the B^0 rest frame. In the rest frame of B^0 meson, the w definition reduces to the relativistic boost factor γ of D^*,

$$w \equiv \frac{\left(m_{B^0}, 0\right) \cdot \left(E_{D^*}, p_{D^*}\right)}{m_{B^0} m_{D^*}} = \frac{E_{D^*}}{m_{D^*}}. \tag{3.41}$$

- $\cos\theta_\ell$: is defined in the rest frame of W the boson, as the angle between the D^* and the lepton.

- $\cos\theta_{\rm v}$: is defined in the rest frame of D^* meson, $\theta_{\rm v}$ as the angle between the D^0 and the D^*.

- χ: is defined in the rest frame of the B^0 meson, and is the angle between the two planes formed by the decays of the W and the D^* meson.

The full differential decay rate for exclusive semileptonic decays $B \to D^*\ell\nu_\ell$ is written in terms of three helicity amplitudes and is defined as [27],

$$\begin{aligned}
&\frac{d^4\Gamma(B^0 \to D^{*-}\ell^+\nu_\ell)}{dw d(\cos\theta_\ell) d(\cos\theta_{\rm v}) d\chi} = \frac{6 m_B m_{D^*}^2}{8(4\pi)^4}\sqrt{w^2-1}(1 - 2wr + r^2) G_F^2 |V_{cb}|^2 \\
&\times\{(1-\cos\theta_\ell)^2 \sin^2\theta_{\rm v} H_+^2(w) + (1+\cos\theta_\ell)^2 \sin^2\theta_{\rm v} H_-^2(w) \\
&+4\sin^2\theta_\ell \cos^2\theta_{\rm v} H_0^2(w) - 2\sin^2\theta_\ell \sin^2\theta_{\rm v} \cos 2\chi H_+(w) H_-(w) \\
&-4\sin\theta_\ell(1-\cos\theta_\ell) sin\theta_{\rm v} \cos\theta_{\rm v} \cos\chi H_+(w) H_0(w) \\
&+4\sin\theta_\ell(1+\cos\theta_\ell)\sin\theta_{\rm v}\cos\theta_{\rm v}\cos\chi H_-(w) H_0(w)\}.
\end{aligned} \tag{3.42}$$

The helicity amplitudes ($H_\pm$,H_0) are defined in terms of ratios of form factors as [30]

$$H_i(w) = m_B \frac{R^*(1-r^2)(w+1)}{2\sqrt{1-2wr+r^2}} h_{A_1}(w) |\tilde{H}_i(w)|, \tag{3.43}$$

where $i = +, -, 0$ and $\tilde{H}_{\pm}(w)$ and $\tilde{H}_evince0(w)$ are defined as

$$\tilde{H}_{\pm}(w) = \frac{\sqrt{1-2wr+r^2}(1 \mp \sqrt{\frac{w-1}{w+1}}R_1(w))}{(1-r)}, \quad (3.44)$$

$$\tilde{H}_0(w) = 1 + \frac{(w-1)(1-R_2(w))}{(1-r)}. \quad (3.45)$$

The four dimensional decay distribution in Equation 3.34, is integrated over three variables leaving any one of the four $(w, \cos\theta_\ell, \cos\theta_v, \chi)$ and we get four one dimensional decay distributions. $H_0(w)$ dominates at the point of zero recoil $w = 1$ while c quark inherits the helicity of the b quark upon decay, $H_-(w)$ dominates for the (V-A) interaction. A nearly stationary decay D^* is unpolarised and thus is a combination of all three states equally, as the velocity of the ejected c quark becomes higher and the c quark approaches more closely a massless state, it becomes preferentially left-handed, and combining its helicity of $-1/2$ with the light spectator d quark leads to a helicity of 0 or -1 for the resultant D^*. The light spectator quark has an equal probability of being helicity $1/2$ or $-1/2$. When w approaches the maximum value, the negatively charged lepton and its corresponding anti-neutrino combine to form a zero helicity state forcing D^* into zero helicity projection which leads to suppression of -1 amplitude. These two states are described in Figures 3.2 and 3.3.

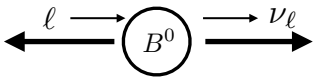

Figure 3.2: Configuration at zero recoil $w_{min} = 1.0$.

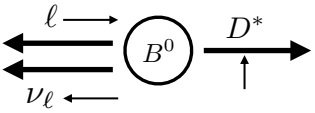

Figure 3.3: Configuration at maximum recoil $w_{max} = 1.504$.

The helicity functions defined in the BGL and CLN paramterisations are plotted using the values from Ref. [2] are given in Table 3.1.

Table 3.1: Input values used in the calculation of $H_0(w)$, $H_+(w)$ and $H_-(w)$.

Variables/Parameters	**Values**
a_0^f	0.01224
a_1^f	-0.052
a_2^f	1.0
a_1^{F1}	-0.0070
a_2^{F1}	0.089
a_0^g	0.0289
a_1^g	0.08
a_2^g	-1.0
$\|V_{cb}\|$	0.0404
nI	2.6
w_{max}	1.50

3.4 Review of measurements of $|V_{cb}|$ with $B \to D^*\ell\nu$ decays

The measurement of $|V_{cb}|$ in semileptonic B decays has primarily been performed at electron-positron collider experiments, namely CLEO, DELPHI and more recently BaBar and Belle. These experiments are considered to be the most suited to the study of semileptonic B decays as the four-momentum of the initial state is well known. CLEO and Belle calculated $|V_{cb}|$ using the decay width of both neutral and charged B mesons where the signal yield is calculated from the variable $\cos\theta_{B,D^*\ell}$ which determines the B direction. BaBar calculated the signal yields from the fit to the missing mass squared (M^2_{miss}) in the tagged measurement of $B \to D$. The decay width was calculated as function of w. DELPHI used $B^0 \to D^{*-}\ell^+\nu_\ell$ decays to calculate $|V_{cb}|$ and ρ^2 from the decay width as a function of q^2 [31]. The measurements by the CLEO and the DELPHI experiments as well as the first B-factory analyses of $B \to D^*\ell\nu$ decays determined $|V_{cb}|$ and the form factor parameter

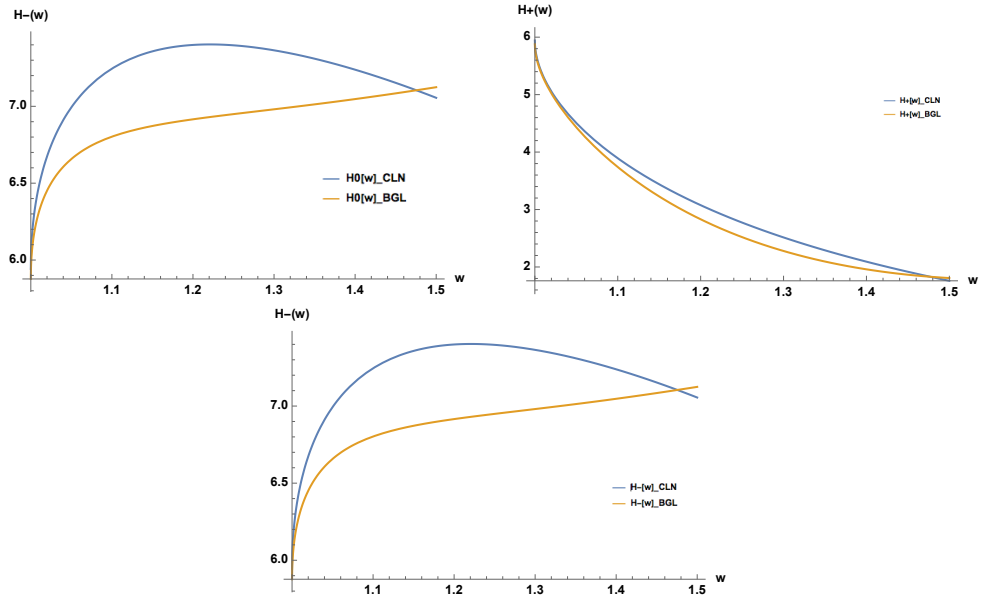

Figure 3.4: Helicity functions $H_0(w)$ (top left), $H_+(w)$ (top right), and $H_-(w)$ (bottom), using parameter values reported in Ref [2].

ρ^2 by measuring the differential decay rate as a function of w only. BABAR and later Belle made the measurement of $|V_{cb}|$ and the CLN form factor parameters (ρ^2, $R_1(1)$ and $R_2(1)$) using exclusive $B^0 \to D^{*-}\ell^+\nu_\ell$ decays using differential decay rates as a function of all four variables $(w, \cos\theta_\ell, \cos\theta_v, \chi)$. Table 3.2 shows the value of $\eta_{EW}\mathcal{F}(1)|V_{cb}|$ measured from different experiments where η_{EW} is the small electroweak correction and $\mathcal{F}(1)$ is the form factor normalisation at zero recoil.

3.5 Inclusive-exclusive tension

Despite the good agreement among $B \to D^*\ell\nu$ results for $|V_{cb}|$, there is a persistent tension between these results and those for inclusive determinations. Table 3.4 summarises the recent results for Belle, and the world averages for $|V_{cb}|$ in inclusive, $B \to X\ell\nu$ and exclusive $B \to D\ell\nu$ and $B \to D^*\ell\nu$ determinations. The inclusive determinations are approximately 10% larger, with a significance of more than 3σ. Several solutions to this puzzle have been put forward: new right handed currents that primarily affect the acceptance of $B \to D^*\ell\nu$, possible problems in the form factor normalisation input from LQCD, possible problems in the use of the CLN parameterisation, or possibly a problem in the inclusive approaches. In this thesis we thoroughly test the use of different form factor paramterisations, and

Table 3.2: Summary of measurements of $F(1)|V_{cb}|\eta_{\rm EW}$ in the CLN scheme.

Experiment (Year)	$\mathcal{L}$ [fb^{-1}]	$\eta_{\rm EW}\mathcal{F}(1)\lvert V_{cb}\rvert \times 10^{-3}$	ρ^2 (rescaled)
CLEO (2002) [32]	3.1	$39.94 \pm 1.23 \pm 1.62$	$1.367 \pm 0.085 \pm 0.086$
DELPHI excl. (2004) [33]	3.5	$36.10 \pm 1.70 \pm 1.97$	$1.081 \pm 0.142 \pm 0.152$
BABAR excl. (2008) [34]	79	$33.94 \pm 0.30 \pm 0.99$	$1.185 \pm 0.048 \pm 0.029$
BABAR D^{*0} (2008) [35]	225	$35.22 \pm 0.59 \pm 1.33$	$1.128 \pm 0.058 \pm 0.055$
BABAR global fit (2008) [36]	207	$35.76 \pm 0.20 \pm 1.10$	$1.193 \pm 0.020 \pm 0.061$
Belle (2010) [37]	711	$34.60 \pm 0.17 \pm 1.02$	$1.212 \pm 0.034 \pm 0.009$
Belle tag. (2016) [38]	711	$35.75 \pm 0.17 \pm 1.01$	1.03 ± 0.13
HFLAV average	-	$35.61 \pm 0.11 \pm 0.41$	$1.205 \pm 0.015 \pm 0.021$

Table 3.3: Summary of measurements of $\mathcal{B}(B^0 \to D^{*-}\ell^+\nu_\ell)$.

Experiment (Year)	$\mathcal{L}$ [fb^{-1}]	$\mathcal{B}.\mathcal{F}(B^0 \to D^{*-}\ell^+\nu_\ell)\%$
CLEO (2002) [32]	3.1	$5.62 \pm 0.18 \pm 0.26$
DELPHI excl. (2004) [33]	3.5	$5.35 \pm 0.20 \pm 0.37$
BABAR excl. (2008) [34]	79	$4.54 \pm 0.04 \pm 0.25$
BABAR global fit (2008) [36]	207	$4.95 \pm 0.02 \pm 0.20$
Belle (2010) [37]	711	$4.56 \pm 0.03 \pm 0.26$
Belle tag. (2016) [38]	711	$4.95 \pm 0.11 \pm 0.21$
HFLAV average	-	$4.88 \pm 0.01 \pm 0.10$

investigate the impact of new right handed currents on the kinematics of the decay.

The aims of this analysis are to measure $|V_{cb}|$, $B \to D^*$ transition hadronic form factor parameters, and perform a fundamental test of lepton flavour universality. The study must take into account various modelling effects such as $q\bar{q}$ continuum, B and fake lepton background contributions, the effects of final state radiation on electrons, and the effect of the finite mass of muons.

In this thesis, two separate form factor parameterisations have been compared in the extraction of $|V_{cb}|$ for the first time in a direct analysis of experiment data. One is the typical model dependent CLN approach used by all experiments for the past 20 years, while the other is a model independent approach that requires large data set for fit con-

Table 3.4: Summary of $|V_{cb}|$ measurements with inclusive and exclusive approaches from the B factories.

Method	Experiment or HFLAV	$\lvert V_{cb}\rvert \times 10^3$
Inclusive kinetic scheme	HFLAV	42.19 ± 0.78
Inclusive $1S$ scheme	HFLAV	42.39 ± 0.52
Exclusive $B \to D\ell\nu$ CLN	Belle	39.85 ± 1.33
Exclusive $B \to D\ell\nu$ CLN	HFLAV	39.44 ± 1.01
Exclusive $B \to D\ell\nu$ BGL	Belle	40.83 ± 1.13
Exclusive $B \to D^*\ell\nu$ CLN	Belle	37.95 ± 1.34
Exclusive $B \to D^*\ell\nu$ CLN	HFLAV	39.04 ± 0.85

version. The comparison of these approaches in a single analysis is a crucial aspect to the interpretation and measurement of $|V_{cb}|$.

The reconstruction efficiency of the analysis is approximately 10% higher than the earlier published untagged Belle analysis, owing to improved track finding algorithms for the 4-layer SVD2 data. In particular the efficiency of D^* slow pions was enhanced, which have a mean momentum of approximately 100 MeV/c in the laboratory frame.

A novel approach to continuum modelling was introduced, to correct off-resonance data for finite effects of translating the 60 MeV/c shift in centre of mass energies using MC simulation.

A new, more precise approach to the evaluation of fake lepton background rate determination was employed. This is particularly important in the evaluation of the LFUV test. The fake rates were are calculated based on a D^* tagged sample of $D^0 \to K\pi$ events.

The effect of finite mass of muon is taking into account by applying a bound on the w distribution. The effects of final state and Bremsstrahlung radiation were taken into account during analysis by searching for nearby electrons. These effects can modify the lepton momentum spectra and hence potentially bias measurements if not carefully taken into account.

Finally, lepton flavour violation universality is tested to unprecedented levels in a B-decay. All previous published analyses of this channel did not present a ratio measurement, making this an important new constraint on physics beyond the standard model.

4. New Physics in $B \to D^* \ell \nu_\ell$

The tension between inclusive and exclusive determinations of $|V_{cb}|$ indicate the possibility of new physics contributions [39]. This includes the possibility right handed currents, or new currents from scalar or tensor particles mediating the decay. There may even be the possibility of lepton flavour universality (LFU) violating effects.

In this chapter, we will briefly discuss the scenarios of presence of new physics in semileptonic B decays.

4.1 Chirality and V-A Interactions

For an interaction corresponding to the exchange of a spin-1 particle, the most general form of an interaction vertex is a linear combination of vector and axial-vector. Parity is not conserved under electroweak interactions, so in electroweak decays the $W^{\pm}$ couples to the weak current which has both vector and axial vector components. An axial-vector is a quantity whose direction is unchanged under parity. This is a spin dependent interaction called a (V-A) interaction. In the relativistic limit, only the LH fermions and RH anti-fermions are emitted in charged current interactions which are the chiral states of electroweak interaction and these chiral states make the helicity states. For a fermion of mass m and energy E, these helicity states are suppressed by a factor of order of $(mc/c^2)^2$. Having a massless fermion, a certain left handed or right handed helicity state is achieved when two component spinors are applied to the operator:

$$\begin{aligned} P_R &= \frac{1}{2}\left(1 + \frac{\sigma.p}{E}\right)(\psi_L + \psi_R) = \psi_R, \\ P_L &= \frac{1}{2}\left(1 - \frac{\sigma.p}{E}\right)(\psi_L + \psi_R) = \psi_L, \end{aligned} \tag{4.1}$$

where ψ_L and ψ_R are positive and negative chirality states for ψ being a solution of the Dirac equation and $P_{R,L}$ are operators that project out states of particular helicity from two component spinors. The (V-A) theory was postulated keeping in view the fact that for massless fermions $H = -1$.

4.2 Right Handed Currents and other New Physics in Semileptonic Decays

In the $B \to D^*$ transition, the hadronic current is a left handed $(V-A)$ interaction where both vector and axial vector currents contribute to the decay. The tension between the exclusive and inclusive determinations of $|V_{cb}|$ could be explained by the presence of an interfering right handed current $(V+A)$ contributions. Such right handed currents would effect the inclusive and exclusive measurement of $|V_{cb}|$ differently, and modify both the rate and the decay kinematics.

In order to accommodate parity violation observed in the weak force, the left and right-handed fermions are assigned to different representations of $SU(2)_L \times U(1)_Y$, with the right-handed fields being singlets of SU(2). Extending the gauge structure of SM involves an additional U(1) gauge symmetry (e.g. a $Z^{'}$). One of the next simplest extensions involves an additional RH $SU(2)$: $SU(2)_L \times SU(2)_R \times U(1)_{B-L}$. According to SM, the quark level semileptonic B decay is described by the four-Fermi interaction of charged left-handed currents while in the presence of NP the effective Hamiltonion is written as [40],

$$\begin{aligned} -\mathcal{H}_{eff} = \frac{4G_F V_{cb}}{\sqrt{2}} \Big[& (1+V_L)[\bar{c}\gamma_\mu P_L b][\bar{l}\gamma^\mu P_L \nu_l] + V_R[\bar{c}\gamma^\mu P_R b][\bar{l}\gamma_\mu P_L \nu_l] \\ & + S_L[\bar{c}P_L b][\bar{l}P_L \nu_l] + S_R[\bar{c}P_R b][\bar{l}P_L \nu_l] + T_L[\bar{c}\sigma\mu\nu P_L b][\bar{l}\sigma_{\mu\nu} P_L \nu_l] \Big] \end{aligned} \tag{4.2}$$

where G_F is the Fermi constant, $P_{L,R} = \frac{1 \mp \gamma_5}{2}$ are the propagators of the positive and negative chirality states with the assumption that the neutrinos are left chiral and $V_{L,R}$ $S_{L,R}$,T_L are vector, scalar and tensor couplings. This effective Hamiltonian is consistent with the SM form if $V_L = V_R = S_L = S_R = T_L = T_R = 0$. The vector and axial vector couplings are written in terms of a left and a right handed contribution by setting

$g_{V,A} = V_R \pm V_L$. Therefore, the Hamiltonian becomes,

$$\mathcal{H}_{eff} = \frac{G_F V_{cb}}{\sqrt{2}} \Big\{ \Big[\bar{c}\gamma_\mu(1-\gamma_5)b + g_V \bar{c}\gamma^\mu b + g_A \bar{c}\gamma_\mu\gamma_5 b \Big] \bar{l}\gamma^\mu(1-\gamma_5)\nu_l + \Big[g_S \bar{c}b + g_P \bar{c}\gamma_5 b \Big] \bar{l}(1-\gamma_5)\nu_l + h.c \Big\}. \tag{4.3}$$

In the presence of new types of charged current interactions such as a charged Higgs or a W' gauge boson, the scalar and pseudoscalar terms would respectively be non-zero [41].

Right handed charged currents were first studied in the context of left right symmetry models by having an additional $SU(2)_R$ symmetry between right handed doublets. This implies the existence of a SM like W-boson which has dominant left handed component with a small admixture of W_R appearing as $W^{'}, Z^{'}$ [42]. The left handed current contribution in the process involving axial-vector and vector current ($B \to D\ell\nu$) is written as,

$$|V_{cb}^L| = |V_{cb}| + |V_{cb}^R|, \tag{4.4}$$

while for the decays involving only the vector current ($B \to D^*\ell\nu$), the right handed contribution is written as,

$$|V_{cb}^L| = |V_{cb}| - |V_{cb}^R|. \tag{4.5}$$

While a right handed current solution to the $|V_{cb}|$ tension is appealing, it has been disfavoured by other analyses based on total rates alone [39]. Typically those analyses did not take into account the effects of different acceptance in the presence of new physics.

4.3 Scalar and Tensor Operators

The differential decay distribution contain information about possible scalar contribution. These contributions come from the lepton-mass-suppressed terms in the decay width of inclusive and exclusive decays. These mass suppressed terms implies that there is no qualitative difference between operators having $\ell = e, \mu, \tau$. In $B \to D^*\ell\nu$ decay, tensor operators apply more precise constraints on the measurement. The point of maximum recoil ($w = 1$), in the case of $B \to D^*\ell\nu$ decay has longitudinal D^* meson which is not possible in the case of a tensor operator. Therefore the momentum transfer observable is very sensitive to the tensor operator near the point of maximum recoil ($w = w_{max}$).

4.4 Lepton Flavour Universality Violation (LFUV)

In the SM, it is predicted that the coupling of the electroweak W boson is independent of the lepton flavour. This referred to as lepton flavour universality (LFU).Two examples of such ratios are the τ to light lepton ratio, and the μ to e atio, define as

$$R(D^*)_{\ell,\tau} = \frac{\mathcal{B}(\bar{B} \to D^* \tau^- \bar{\nu_\tau})}{\mathcal{BF}(\bar{B} \to D^* \ell^- \bar{\nu_\ell})} \ , \tag{4.6}$$

and

$$R(D^*)e, \mu = \frac{\mathcal{B}(\bar{B} \to D^* \mu^- \bar{\nu_\mu})}{\mathcal{BF}(\bar{B} \to D^* e^- \bar{\nu_e}).} \tag{4.7}$$

Recent observed tensions with the SM expectation in the measurement of $b \to c\tau\nu$ and $b \to s\ell\ell$ transitions motivates the study of electron and muon universality in $b \to c\ell\nu$ decays and is an important measurement. Although many experimental measurements assume LFU holds true, there are certain theoretical models that predict violation of LFU, such as those with a charged Higgs boson.

In this thesis, precise measurements of rates, decay kinematics differentials, and lepton flavour universality.

5. The Belle Experiment

The Belle experiment is a B meson factory and is designed to investigate CP violation, perform precision measurements of CKM matrix elements and study rare decays. These studies require large data samples of B mesons. Thus, the accelerator and detector setup of the Belle experiment enables us to analyse more than 772 million $B\bar{B}$ pairs via $\Upsilon(4S)$ decays [43]. The Belle experiment is located in Tsukuba, Japan and is managed by the High Energy Accelerator Research Organisation known as KEK. It is operated by the collaboration of 18 countries and more than 60 institutions from all over the world. It became operational in 1999 when the Belle detector was able to start taking data, and completed data taking in 2010.

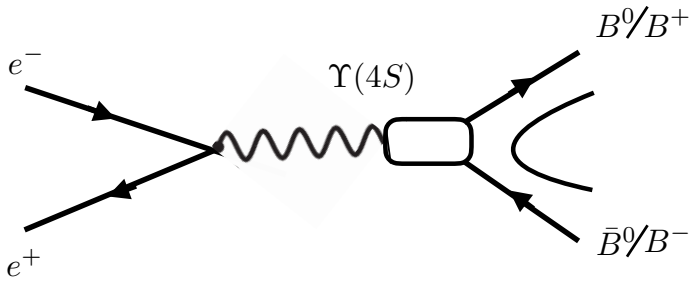

Figure 5.1: B-meson production in e^+e^- collisions at the $\Upsilon(4S)$ resonance.

5.1 KEK-B Accelerator

KEK-B is a circular electron-positron collider with beam energies of 8 GeV for the electron, High Energy Ring (HER) and 3.5 GeV for the positron, Low Energy Ring (LER). The total center-of-mass energy is 10.58 GeV [44]. The decay diagram is shown in Figure 5.1 and a schematic of the accelerator layout is shown in Figure. 5.2.

$$\sqrt{s} = 2\sqrt{E_{\mathrm{HER}} E_{\mathrm{LER}}} \approx 10.58\,\mathrm{GeV}, \tag{5.1}$$

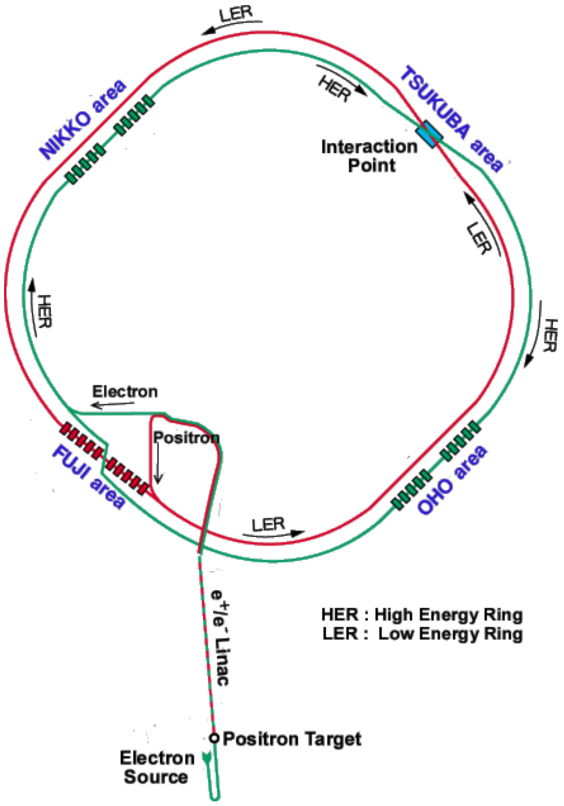

Figure 5.2: The KEKB Collider Rings, and the interaction point where the Belle experiment is located [3].

This is the rest mass of $\Upsilon(4S)$ which decays to $B\bar{B}$ pairs as shown in Figure 5.1. These beam energies are accelerated in the HER and LER each of length 3 km. The electron and positron beams are not of equal energy, which allows the production of boosted B mesons. This energy asymmetry lets the time dependent features of B meson decays to be studied with high precision. This includes CP violation. $B\bar{B}$ pairs produced by the asymmetric e^+e^- collider move along the beam axis in the lab frame. The boost parameter is defined as

$$\beta_\gamma = \frac{E_- - E_+}{\sqrt{s}}, \tag{5.2}$$

where E_- is the electron energy and E_+ is the positron energy. The collision happens at the Interaction Point (IP) where the particles in both the rings collide simultaneously with a crossing angle of 2 mrad. The total design luminosity was 1.0×10^{34} cm^{-2} s^{-1} while the maximum reached was two times that figure. The design beam currents are 2.6 A for LER and 1.1 A for HER. The electrons and positrons interact with each other through various processes at the IP. The rate at which the electrons and positrons collide

is defined as the product of luminosity and the total interaction cross section,

$$R = \mathcal{L}\sigma_{e^+e^-}, \tag{5.3}$$

where $\sigma_{e^+e^-}$ is the cross section is measured in units of cm^2 and luminosity is measured in units of $\mathrm{cm}^{-2}\mathrm{c}^{-1}$. The center-of-mass energy is designed to produce the $\Upsilon(4S)$ resonance (the excited state of $B\bar{B}$), where the cross section for $\Upsilon(4S)$ is given by,

$$\sigma(e^+e^- \to \Upsilon(4S)) = 1.1\,\mathrm{nb}. \tag{5.4}$$

here nb means nano barn (barn is the standard unit for measurement for cross section and is defined as $\mathrm{b} = 10^{-24}\mathrm{cm}^2$). The time integrated luminosity achieved by Belle is 711 fb^{-1} [45] and is defined as

$$\mathcal{L} = \int \mathcal{L}dt. \tag{5.5}$$

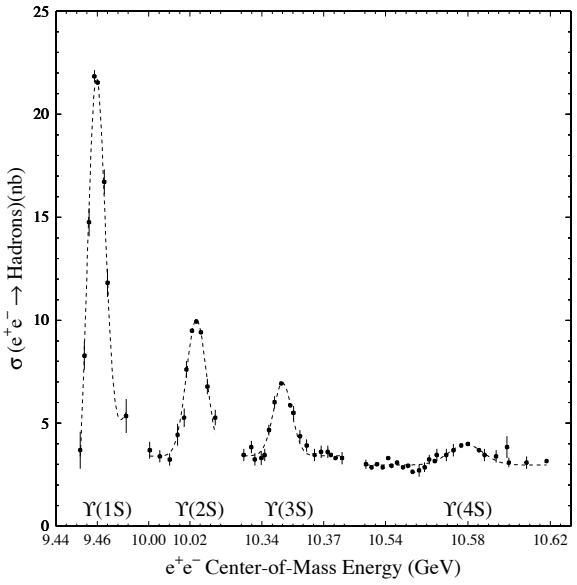

Figure 5.3: Cross-section of Υ production in e^+e^- collisions.

Quarkonia resonances with a mass lower than that of the $\Upsilon(4S)$ are also recorded as shown in Figure. 5.3. This is important because data samples taken at different center-of-mass energies are used for energy scan so that the data is taken at the most efficient energy for $\Upsilon(4S)$. Therefore, additionally $\approx$ 90 fb^{-1} of "off-resonance" data recorded at $\sqrt{s} = 10.52$ GeV to study non-BB backgrounds. This consists mainly of events where

light quarks are produced (q = u, d, s, c) to understand $e^+e^- \to q\bar{q}$ continuum events. This continuum analysis is very important for the decays in which continuum is a large background. $\Upsilon(5S)$ decays are also important for example to study B_s decays. In such events, the energy asymmetry is kept constant at $B_\gamma = 0.425$.

5.2 Belle Detector

The Belle detector, is a particle spectrometer surrounding the interaction point (IP). It is configured in a magnetic field of 1.5 T. and covers the interaction region of the KEKB beams. The detector consists of following sub detectors: Silicon Vertex Detector (SVD), Central Drift Chamber (CDC), Aerogel Čherenkov Counters (ACC), Time of Flight (TOF), Electromagnetic Calorimeter (ECL), K_L and μ detector (KLM) [4]. A schematic of the Belle detector is shown in Figure.5.4.

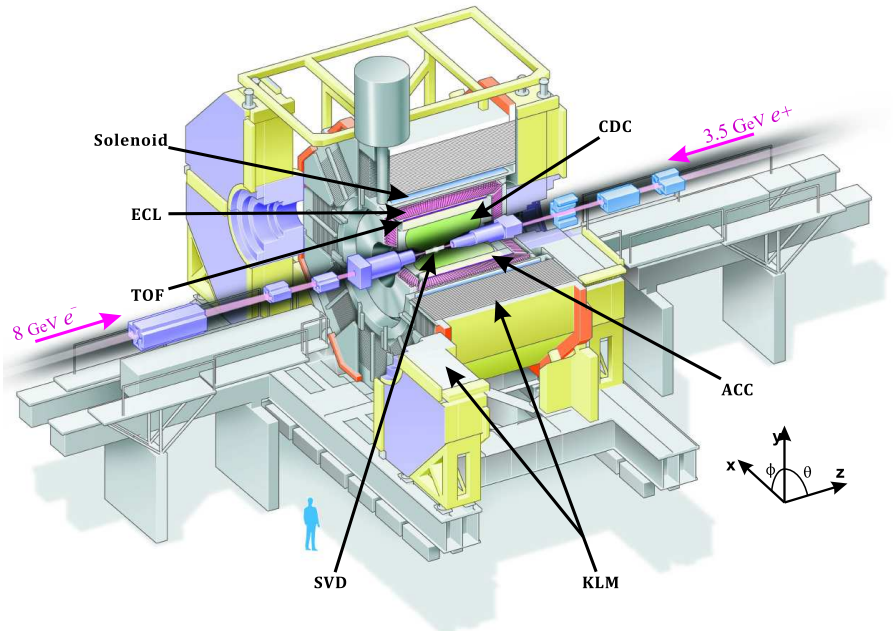

Figure 5.4: The Belle Detector Schematic [4].

Before discussing the sub-detectors, it is important to understand the coordinate system of the Belle detector. The origin coordinates of the system are defined by the location of the IP. The z-axis is defined to be along the axis of the magnetic field within the solenoid, the x-axis is the horizontal axis and the y-axis is the perpendicular axis in a right-handed coordinate system. The polar angle θ is measured relative to the positive z-axis whereas the azimuthal angle ϕ is defined with respect to positive x-axis in the x-y plane. The

radius in the cylindrical coordinate system is then defined as r = $\sqrt{x^2 + y^2}$. The polar angle θ covers the range $\theta \in (17°, 150°)$ for the detector.

5.2.1 Interaction Region

The interaction region is the region inside the accelerator vacuum where the two beam pipes of the HER and the LER merges into one pipe. The precise information of the decay vertices is very important. There are two challenges at the IP: the large beam background due to Coulomb scattering and the heat produced by the beam pipes. Although it is best to put the SVD as close to the IP as possible, it is not quite accomplished due to the construction of a double wall beryllium pipe for minimising beam background. This is a 0.5 mm wall which is mounted on the aluminium pipes which results in the extension of the IP from $z = 4.6$ cm to $z = 10.1$ cm, having a radius of $r = 2.5$ mm. The gap induced in the pipes is filled with Helium gas which is constantly flowing through the gap. This wall not only reduces the Coulomb scattering background but also provides cooling to the beam pipes. Several additional horizontal covers have been installed to protect the IP from beam background.

5.2.2 Silicon Vertex Detector (SVD)

The SVD is the inner most detector and consists of a Double Sided Silicon Detector (DSSD) [46]. The DSSD has 1280 silicon strips on each side to detect particles passing through it by measuring the charges collected on the strips. The DSSD covers a solid angle of $17° < \theta < 140°$. The three layers are the inner, middle and outer layer with 8, 10 and 14 ladders, respectively. Some internal alignment among the sensors is done using these ladders in the $r - \phi$ plane. The signals coming from each layer of the DSSD are read out by circuits which are mounted on the ceramic hybrids. These circuits are VA1 front end integrated circuits with high performance ($200e^- + 8e^-/pF$) and good radiation tolerance (200 kRad). The DSSD is based on a pn junction, and to reach full depletion it works reverse biased. When a charged particle passes through the junction, electrons from the valence band move into the conduction band which creates an electron-hole pair. The purpose of these electron-hole pairs is to start the flow of current in p^+ and n^+ strips, which are located on the opposite sides of the DSSD.

At the time of installation of the Belle detector (1998), the SVD consisted of a 3 layered

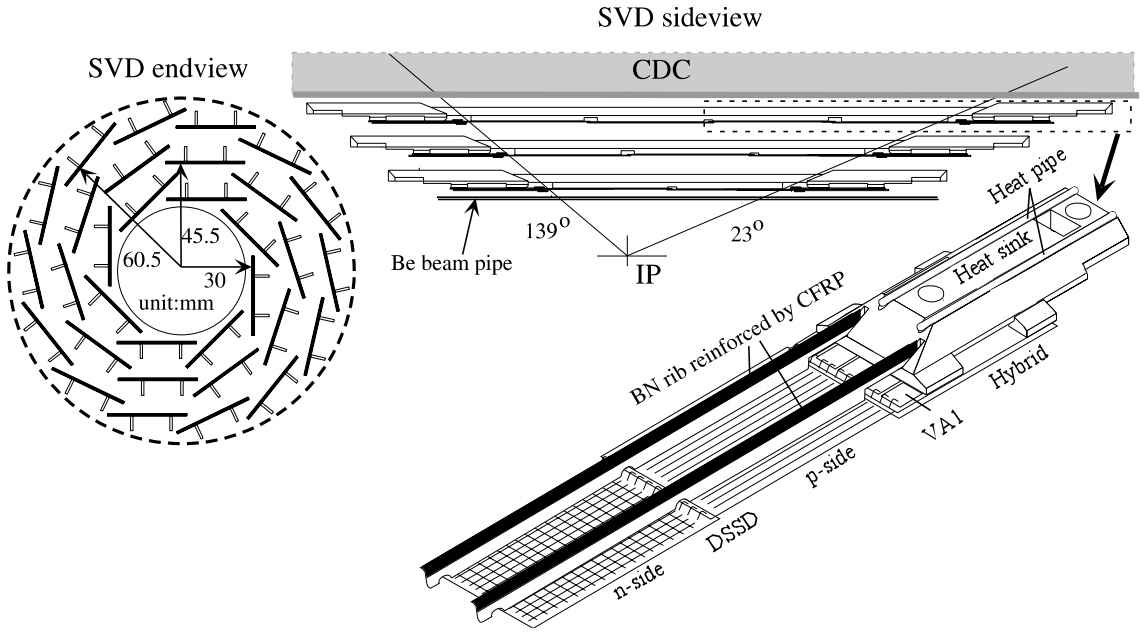

Figure 5.5: Silicon vertex detector, side view of SVD2 [5].

DSSD with an acceptance region of $\theta \in (23°, 139°)$, but after an upgrade in 2003 the three layered DSSD was replaced by a four layered DSSD. The installation of the fourth layer increased the polar angle coverage to $\theta \in (17°, 150°)$. This new configuration is refferred as SVD2. and the former as SVD1. The upgrade also increased the radiation tolerance and the spatial resolution was highly improved.

The purpose the SVD serves is to identify the decay vertices of the B mesons which is important for the study of CP violation since we need to know the difference between life times of each B mesons. This is achieved by measuring the distance between the decay vertex of the B meson pair in the z-direction. We can measure this distance as precisely as $\sim$100 μm, which is shorter than the average flight distance of B mesons is 200 μm at Belle. Apart from vertex measurement, the SVD gives information for racking of charged particles. The performance of SVD1 and SVD2 is summarised in Table 4.1 and Figure 5.5. Parameters such as the signal-to-noise ratio, impact parameter resolution and efficiency are shown. The resolution for the impact parameters dz and dρ was obtained from cosmic rays measured during the collision data taking.

5.2.3 Central Drift Chamber (CDC)

Accurate momentum information for charged tracks is crucial. Charged particles are identified by the precise measurement of their momentum and by reconstructing the tracks of

Table 5.1: Comparison between characteristics of two SVD configurations.

Variables	SVD1	SVD2
Signal-to-noise ratio S/N	>17	>16
Mean occupancy in layer 1 (%)	~ 6	~ 10
Matching efficiency (%)	98	98
Impact parameter resolution for dz (p = 1 GeV/c, $\theta = 90°$)	61 μm	42 μm
Impact parameter resolution for dρ (p = 1 GeV/c, $\theta = 90°$)	57 μm	42 μm

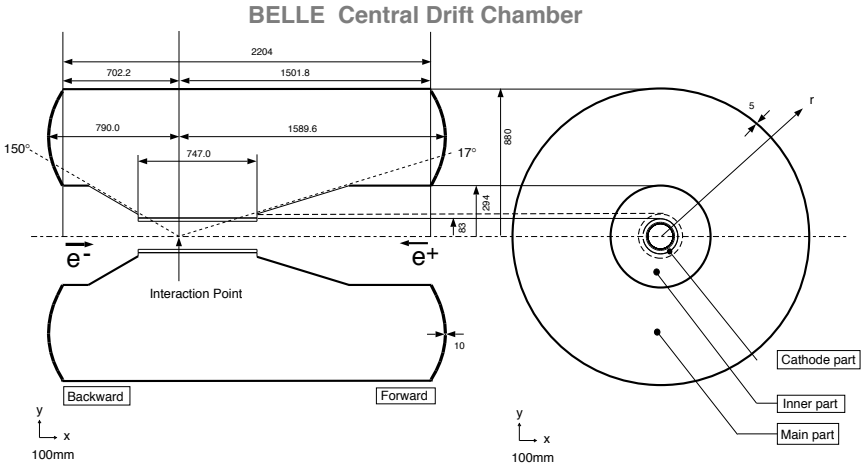

Figure 5.6: Schematic of the central drift chamber in side (left) and frontal (right) projections [6].

charged particles. Outside the SVD, a drift chamber is installed in the Belle detector. The CDC is operated in such a way that it reconstructs the trajectories of the charged particles on the principle of ionisation of the gas when particles passing through the material inside the detector. The energy loss, dE/dx, information from the particle during the ionisation process is used for particle identification and in trigger system. The momentum resolution for high momentum charged particles in the region ($17° \leqslant \theta \leqslant 150°$) is approximately

$$\sigma_{|p_t|} \sim 0.005\sqrt{1 + |\mathbf{p}_t|}, \tag{5.6}$$

where, p_t is the transverse momentum of the charged track. The CDC consists of 52 cylindrical layers, each of which is arranged in 13 stereo and axial super-layers between 8.5 cm and 90 cm in radius. 8400 drift cells have been installed in the Belle CDC. The cathode strips are used to obtain very efficient z-trigger information in the chamber layers. Three

layers are used for each stereo super layers and four layers for the three outermost stereo super-layers. Stereo angles in each stereo super layer are determined by maximising the z-measurement capability while keeping the gain variations along the wire below 10%. The ionized particles are accelerated until they reach a optimal velocity where energy gained from the electric field equals the average energy loss due to interaction with surrounding gas. This leads us to a simple relation between the time taken by the particle to reach the cathode plate and the velocity of the charged particle. Hence, the position of creation of the particle is determined accurately. The trajectory of the charged particle is measured by taking several measurements of the location of the incident particle. Since the magnet provides a homogeneous field, the track will follow a helical shape and its curvature will be inversely proportional to the momentum of the particle. Another important feature of the CDC is its asymmetric construction. This is done to account for the non-zero momentum in the center-of-mass frame in the z direction, resulting from the asymmetric beam energies at KEKB.

Like in the SVD, the CDC also suffers from beam background. Minimising the Coulomb scattering effect in the CDC is also very important. In order to reduce this effect, low Z gas is used and hence, the momentum resolution is improved.

5.2.4 Aerogel Čerenknov Counter (ACC)

The identification of kaons and pions is very important at Belle. The ACC plays a vital role in the identification of charged kaons and pions. Located outside CDC, Čherenknov counters have been installed at Belle. Čherenknov radiation is emitted when a particle is travelling faster than the speed of light in a medium and is emitted at a fixed angle with respect to its direction of travel. The particle must achieve a threshold velocity in a medium of refractive index n,

$$v > v_{\min} = 1/n. \tag{5.7}$$

Two charged particles are identified by emission of different types of Čherenknov radiation even when their momentum is same. From this, we know that the particle masses and the velocity with which they travel are different. Given that pions and kaons have different masses, for a certain refractive index of the material and particles of the same momentum, pions emit light while kaons do not. Particle identification is then extended beyond the measurement of dE/dx by the CDC. Additionally, the particles energy remains unaffected

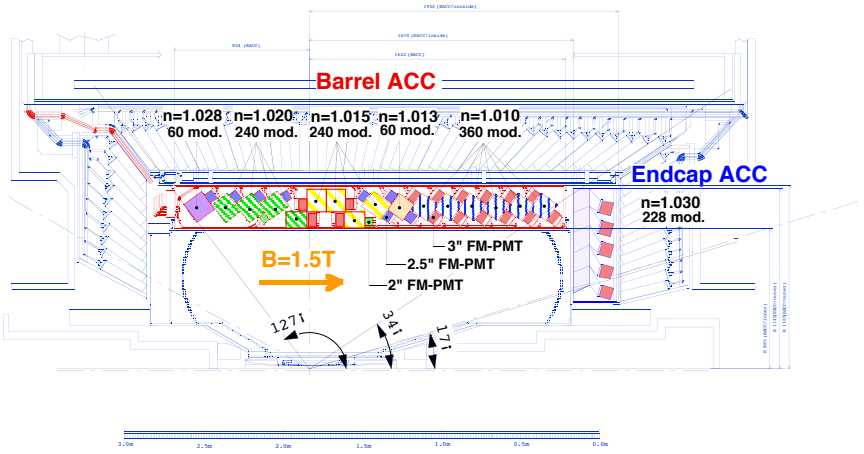

Figure 5.7: The configuration of the ACC. [7].

by the Čerenknov radiation, and minimally affected by the ACC material.

In terms of construction, there are two regions of the ACC, the barrel and the forward endcap. The barrel consists of 960 counters, segmented into 60 cells in the ϕ direction, and the forward end cap consists of 228 counters, arranged into 5 concentric layers. The refractive index is chosen on the basis of the polar angle and hence the K/π discrimination is performed by the choice of specific medium of suitable refractive indices. These refractive indices cover the range of momenta, n = 1.01 to 1.03. Two mesh type photo-multiplier tubes (FM-PMT) are used to distinguish the Čerenknov light. Like the CDC, the ACC is also under the influence of a strong magnetic field which affects the counting of the Čerenknov photons, but the FM-PMTs, maintain the accurate counting of the Čerenknov photons. These FM-PMTs are calibrated by μ-pairs for various pulse heights. A total of 10 to 20 photo electrons are detected in the barrel ACC, whereas 25 to 30 are detected in the forward endcap ACC. The polar angle coverage of the ACC is $17° < \theta < 140°$. Hence, the ACC provides good separation between kaons and pions with a kaon efficiency more than 80% and a pion fake rate (i.e. a pion misidentified as a kaon) of less than 10%.

5.2.5 Time of Flight Counter (TOF)

Charged particles in the momentum range of 0.8 GeV/c to 1.2 GeV/c are identified using the TOF. It gives precise measurements of timing for the incident particles by using plastic scintillation counters, which have time resolution of 100 ps for 1.2 m flight path (particles originating at the IP passing through the scintillator). Particles produced by an $\Upsilon(4S)$

have momenta below 1.2 GeV/c and comprise 90% of the particles produced at Belle.

In terms of construction, the TOF consists of 64 modules which are concentrically arranged around the z-axis at a radius of 1.2 m. Each module is made up of two types of counters which are separated by a radial distance of 1.5 cm: TOF counters and one Trigger Scintillation Counter (TSC). These cover a radial angle of $34° < \theta < 120°$. Scintillation light coming from the TSC is collected by the FM-PMTs where the PMTs are used to optimise gain in the magnetic field. Another FM-PMT is used by the TOF counter for triggering purposes [47]. For a given path length (L), the mass of the detected hadron can be calculated from the time needed to reach the TOF using the equation,

$$mass^2 = (\frac{1}{\beta^2} - 1)P^2 = \left[\left(\frac{cT}{L} - 1\right)\right]P^2, \tag{5.8}$$

where P is the momentum of the particle determined from CDC track fit and T is the time walk corrected observed time. Figure.5.8 shows the distribution of the mass for the detected tracks where the peaks in the figure corresponds to pion, kaons and protons.

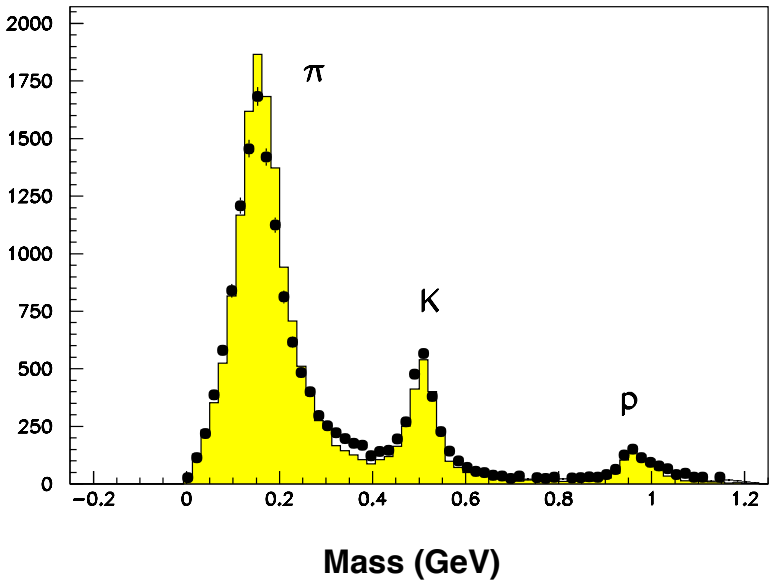

Figure 5.8: Calculated mass for detected tracks using TOF timing information for particle of momentum < 1.2 GeV/c. The points are taken from data and the coloured histogram is from MC.

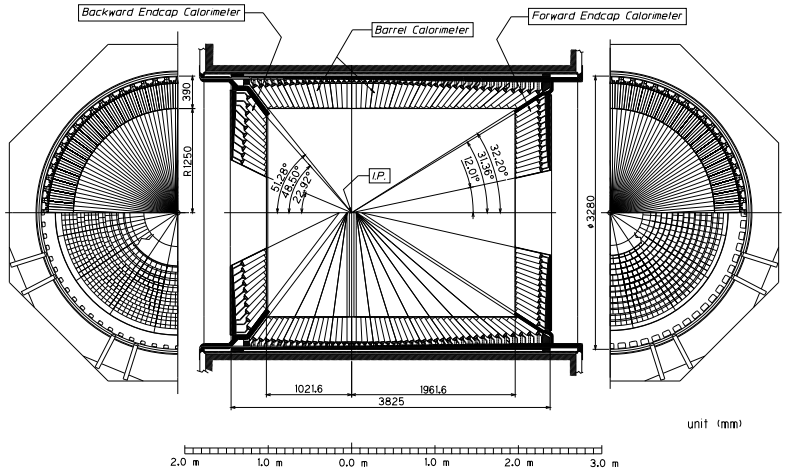

Figure 5.9: ECL Configuration [4].

5.2.6 Electromagnetic Calorimeter (ECL)

The ECL absorbs the energy of traversing particles such that the total energy can be measured for electromagnetic interaction and electrons can be separated from hadrons using electromagnetic shower E/p. The main purpose of the ECL is to measure the energy of the electrons and photons produced in collisions. The ECL plays a vital role in electron identification. The high energy photons and electrons that enter the ECL interact with its material and produce radiation via bremsstrahlung and electron-positron pair production phenomenon. The neutral pion decays to two photons ($\pi^0 \rightarrow \gamma\gamma$) with energy as high as 4 MeV/c^2, so good resolution is required to minimise background. It is important to separate the photons produced by these processes and hence, to determine of opening angle between final state photons.

In terms of construction, the ECL consists of a 3.0 m barrel, with an inner radius of 1.25 cm, a forward endcap at $z = +2.0$ m and a backward endcap at $z = -1.0$ m, with polar angle coverage of $32.2° \leqslant \theta \leqslant 128.7°$, $12.0° \leqslant \theta \leqslant 31.4°$ and $130.7° \leqslant \theta \leqslant 155.7°$, respectively. It consists of 8736 highly segmented Thallium doped Caesium Iodide (CsI(TI)) scintillator crystals. Thallium is used because it has an ability to shift the crystal excitation light into visible light which is then detected by a pair of photodiodes placed at the back end of each crystal. The crystals used in the barrel and the endcaps vary in size with measurements of 55×55 (front), 65×65 (back) for barrel while the forward endcap and backward endcap measurements vary from 44.5 mm to 70.8 mm and from 54 mm to 82 mm respectively and weighs 43 tons. In addition to particle identification, the ECL

provides information for luminosity measurement.

5.2.7 K_L and μ Detector (KLM)

This sub detector is the outermost part of the Belle detector. As is evident from its name, it assists with particle identification of K_L mesons and muons since both particles are the long lived and highly penetrating. It can identify muons and K_L mesons that have momenta greater than 600 MeV/c. These particles are very stable and they typically don't decay inside the interior detector layers. The barrel covers an angular region of $45^\circ < \theta < 125^\circ$ and the end cap covers $22^\circ < \theta < 150^\circ$.

In terms of construction, it consists of double-gap resistive plate counters (RPC) and 4.7 cm thick iron plates. There are 15 detector layers and 14 iron layers in the octagonal barrel region and 14 detector layers in each of the two end caps. These iron plates provide 3.9 radiation length of material. The K_L particles interact with these iron plates and produce hadrons which help determine the direction of travel. The range and direction of non-showering charged particles are used to differentiate muons from charged kaons and pions. The double-gap produces an efficiency in the super-layer of more than 98%, which is greater than the case with a single RPC layer. The angular resolution from the interaction point is better than 10 mrad. For muons with a momentum greater than 1.5 GeV/c, the muon identification efficiency is greater than 90% with a misidentification rate of less than 5%.

5.2.8 Solenoid Magnet

The solenoid at Belle provides a magnetic field of 1.5 T which covers a cylindrical volume of diameter 3.4 m and 4.4 m of length. This magnet covers all the sub-detectors except for the KLM. A strong magnetic field bends charged tracks and allows for the measurement of their momenta and to distinguish their charges.

5.3 Offline Reconstruction/Monte Carlo (MC)

Analysis of data requires a detailed understanding of detector effects, possible background components and the interpretation of results. A large sample of Monte Carlo (MC) simulation is used, (usually corresponding to several times the amount of data collected). In

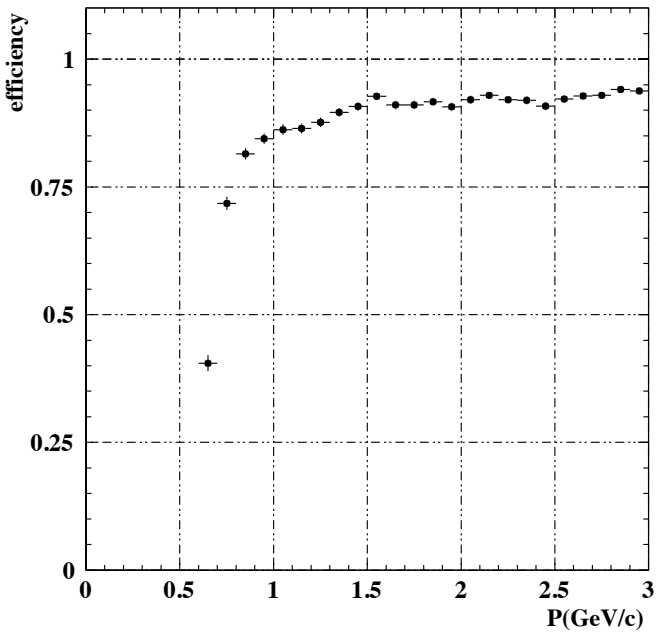

Figure 5.10: Muon identification efficiency versus momentum in the KLM detector [4]

these simulations the theoretical understanding of physical processes in observed decays and our knowledge of detector effects is incorporated. Two levels of MC production are present: one focused on the physics of decays (generation) and the other on simulation of the interaction of particles with the detector (simulation). Events with a $B\bar{B}$ pair are generated using EvtGen [48]. For the continuum $e^+e^- \to q\bar{q}$ ($q = u, d, s, c$) events, the initial quark pair is hadronised by PYTHIA, and hadron decays are modelled by EvtGen. The final-state radiation from charged particles is added using PHOTOS [49]. Detector responses are simulated with GEANT3 [50].

5.4 Charged/Neutral Particle Reconstruction

5.4.1 Particle Identification (PID)

The PID is performed using the information received from several sub detectors including: SVD, CDC, TOF, ECL and KLM. The dE/dx information is provided by the CDC where as the TOF measures the time taken by the charged particle from IP to the TOF which gives the velocity of the particle.

5.4.1.1 Electron Identification

Electrons are identified using information received from the ECL, ACC and CDC. The ECL provides electromagnetic shower shape information as electrons lose all the energy in the ECL (contrary to other charged particles as kaons and pions) so the E/p ratio for electron is approximately 1 for the high momentum electrons. Hence the electrons are easily identified as compared to heavier charged particles particularly hadrons. For low momentum tracks the E/p value is smaller than 1 which makes the distribution appear similar to that of other particles. Another variable which is helpful in identification of electrons is E_9/E_{25}: the ratio of energy deposited in a 3×3 square of CsI crystals to energy deposited in a 5×5 square and is close to 1 for electrons. The CDC and the ACC provide energy deposition information (dE/dx) and velocity difference. At Belle, the threshold momentum required for charged track reconstruction is 50 MeV/c whereas Čherenknov radiation is emitted from electrons of momenta > 4 MeV/c. The electron identification probability is found by

$$\mathcal{P}_e = \frac{\prod_{i=1}^{5} \mathcal{L}_i^e}{\prod_{i=1}^{5} \mathcal{L}_i^e + \prod_{i=1}^{5} \mathcal{L}_i^\pi}, \tag{5.9}$$

where the index i runs over all variables used for the identification of electrons. Figure 5.11 shows the efficiency for electron identification based on measurements of radiative Bhabha events. Hadron fake rates are near 0.2%.

5.4.1.2 Muon Identification

Charged tracks are identified as muons by using information received in the KLM from the CDC and the SVD. The muon tracks are extrapolated to the muon detector which are originate from the CDC with associated hits found within 25 cm of the extrapolated track. Muon identification is performed using two variables:

(1) ΔR: the difference between the measured and expected range of the tracks

(2) χ_r^2: the normalised transverse deviations of all hits associated with the track

Muons are then selected from the probability ratio using:

$$\mathrm{Prob}(\mu) = \frac{\mathrm{p}_\mu}{\mathrm{p}_\mu + \mathrm{p}_\pi + \mathrm{p}_\mathrm{K}}, \tag{5.10}$$

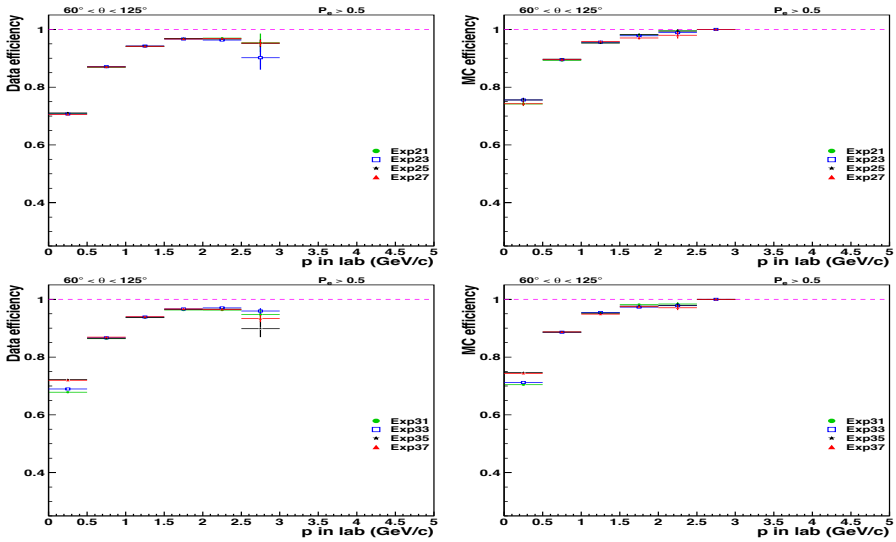

Figure 5.11: Electron identification efficiency for data (left) and MC (right), in $60° < \theta < 125°$ region (barrel), for $Prob(e) > 0.5$. Top and bottom plots correspond to SVD1 and SVD2 respectively. [8]

where p_μ is the muon momentum, p_π is the π momentum, and p_K is the Kaon momentum.

5.4.1.3 K/π Identification

Charged hadron tracks are identified by using the ionisation energy deposition information (dE/dx) from the CDC, velocity information from the TOF and the number of photo-electrons in the ACC. The likelihood of the particle is calculated using the products of likelihoods from each sub detector as

$$\mathcal{L}_{hyp} = \mathcal{L}_{ACC} \times \mathcal{L}_{TOF} \times \mathcal{L}_{dE/dx}. \tag{5.11}$$

The hadrons are then separated using the probability of a signal particle hypothesis. This probability is defined as

$$Prob(sig/bkg) = \frac{\mathcal{L}(\text{signal})}{\mathcal{L}(\text{signal}) + \mathcal{L}(\text{background})}. \tag{5.12}$$

5.5 SuperKEKB and Belle II Detector

A successor to the Belle and KEKB facility is currently under construction, namely Belle II and SuperKEKB, and will be ready for its first high luminosity physics run in 2019

following a commissioning run in 2018. The SuperKEKB collider project was founded in 2008 and the ground breaking was in 2011. Its design peak luminosity is 8×10^{35} cm^{-2} s^{-1} owing to a redesigned final focusing system called a “nano-beam" scheme as well as higher currents. In 2018 SuperKEKB achieved a luminosity of 5×10^{33} cm^{-2} s^{-1} during commissioning, close to the KEKB design. The Belle II detector is expected to collect ∼50 ab^{-1} data, primarly at the $\Upsilon(4S)$ like Belle. Belle II is tasked to perform high precision measurements and to search for rare and forbidden flavour transitions. The designed 40

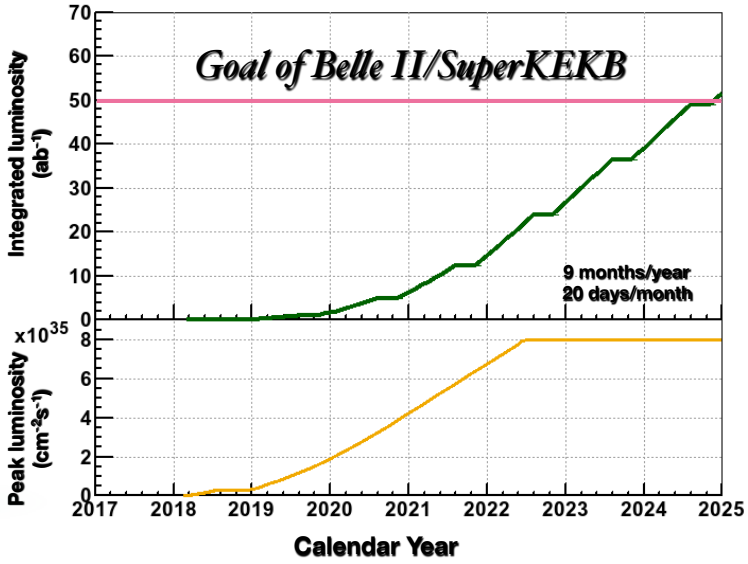

Figure 5.12: Luminosity profile of the next generation B factory, Belle II at SuperKEKB.

times increase in luminosity also brings in higher more bnd, leading toackgrou detector occupancy, pile-up, fake hits, increased trigger and DAQ rates, and radiation damage. Most of the Belle detector has been replaced with components more suited to the much higher readout rate, and to improve the particle reconstruction performance. Some of the impacts on physics analyses are highlighted below.

Owing to the use of pixel detectors at very small radius, the impact parameter and vertex resolution should improve by a factor of ∼ factor 2. Due to the larger radius of the silicon strip detectors, the acceptance of K_S decays is expected to increase by ∼ 30%. A larger radius of the central drift chamber implies a larger level arm for track reconstruction, hence approximately 30% better invariant mass resolution on $D^0K\pi$. New tracking algorithms that are based on silicon only information improve slow π^+ reconstruction efficiency. Belle II has fast signal shaping and waveform fits of electromagnetic calorimeter signals to preserve good energy resolution in the higher beam background environment.

Replacement of the time of flight with a time of propagation Cerenkov imaging detector leads to better K/π separation: reducing $\pi \to K$ fake rates by ~ 2.5.

6. Analysis Procedure

6.1 Event Sample

The data sample used in this measurement is based on the full Belle $\Upsilon(4S)$ data set, which has an integrated luminosity of 711 fb^{-1} (equivalent to 772 M $B\bar{B}$ pairs). Continuum data taken 60 MeV below the $\Upsilon(4S)$ resonance is used to model the non-$B\bar{B}$ background, equal to 88 fb^{-1}. Due to reliance on slow pion tracking, the data sample is divided into two parts: experiments 7-27 which is based on the tracking algorithm of SVD1 (three layered SVD), consisting of 140 fb^{-1}. Experiments 31-65 are based on the new tracking of SVD (four layered SVD), with better efficiency for slow pion momentum reconstruction. Figure 6.1 shows the generated and reconstructed slow pion momentum distributions, normalised. One can see that tracks with momenta below 100 MeV are reconstructed with lower efficiency. Throughout the entire analysis, the samples are analysed separately

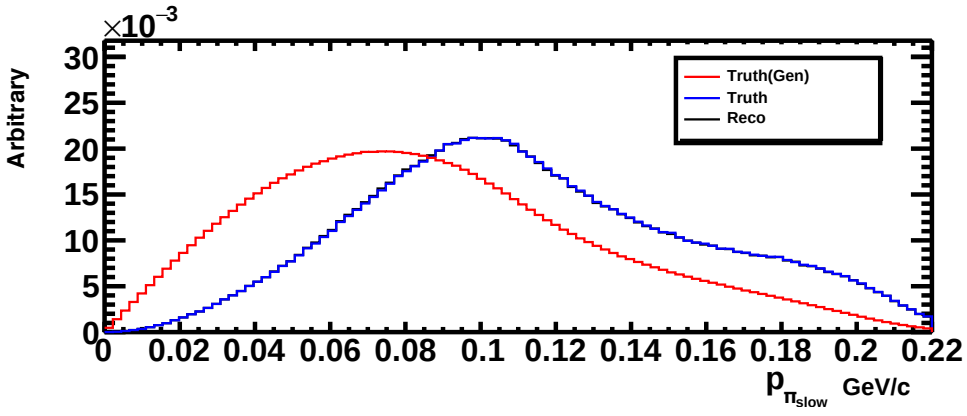

Figure 6.1: Normalised distribution of slow pion momentum comparing generated (red), generated after signal reconstruction (blue), and reconstructed momentum (black) distributions.

based on lepton flavour (electrons and muons). Lepton flavour universality of the weak

interaction predicts that the results should be compatible.

Monte Carlo simulated events are used to determined the analysis selection criteria, study and estimate the background contribution, and estimate the signal reconstruction efficiency. Run dependent detector and beam background conditions are used for all simulations.

6.2 SM Study of $B^0 \to D^{*-}\ell^+\nu_\ell$ Decay

There are three form factors that contribute to the $B^0 \to D^{*-}\ell^+\nu_\ell$ decay in the CLN formalism. The uncertainties on the free parameters $(\rho^2, R_1(1), R_2(1))$ have a non-negligible impact on decay kinematics modelling. The values of the parameters used in this part of the analysis are the world average (WA) values taken from the Heavy Flavour Averaging Group (HFLAV) where $\rho^2 = 1.207 \pm 0.028$, $R_1(1) = 1.401 \pm 0.033$ and $R_2(1) = 0.854 \pm 0.020$. Variations to these parameters modify the kinematics of the decay. The helicity functions defined in Chapter 3.3.3, modify the kinematics of $B^0 \to D^{*-}\ell^+\nu_\ell$ decays which are investigated with 3σ ($\pm 3\sigma$) deviations of each form factor, with respect to world averages. Figures 6.2, 6.3, and 6.4 show that the observables are most sensitive to variations in ρ^2 and $R_2(1)$, and that w and $\cos\theta_\ell$ are particularly sensitive.

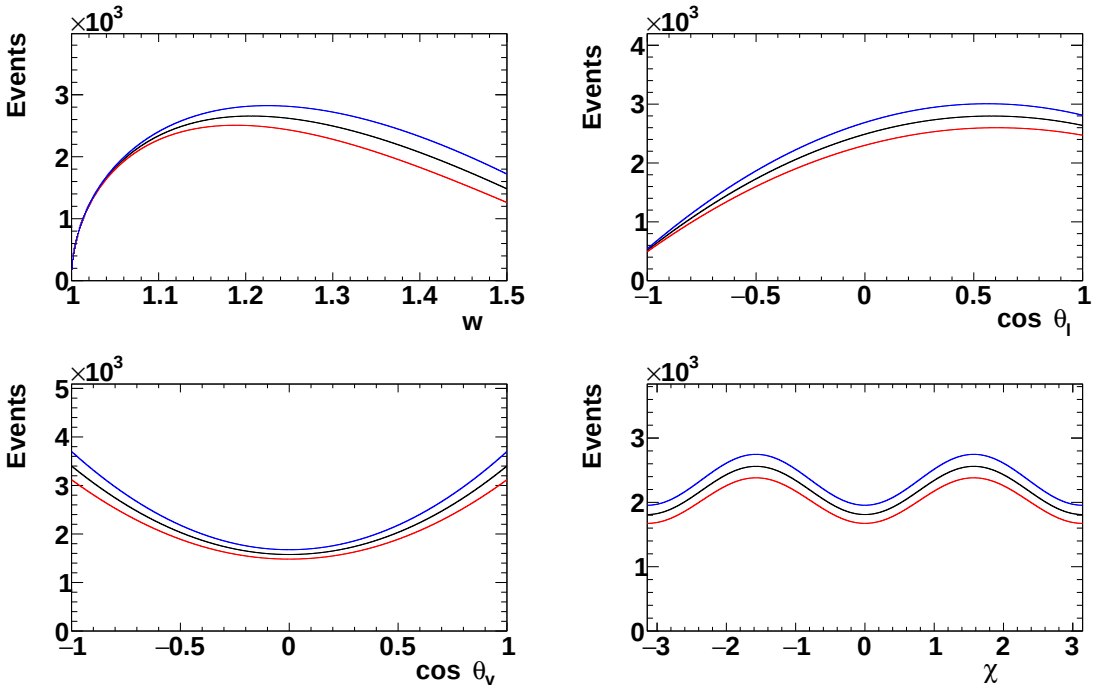

Figure 6.2: Observables modified by varying ρ^2 by $\pm$ 3σ.

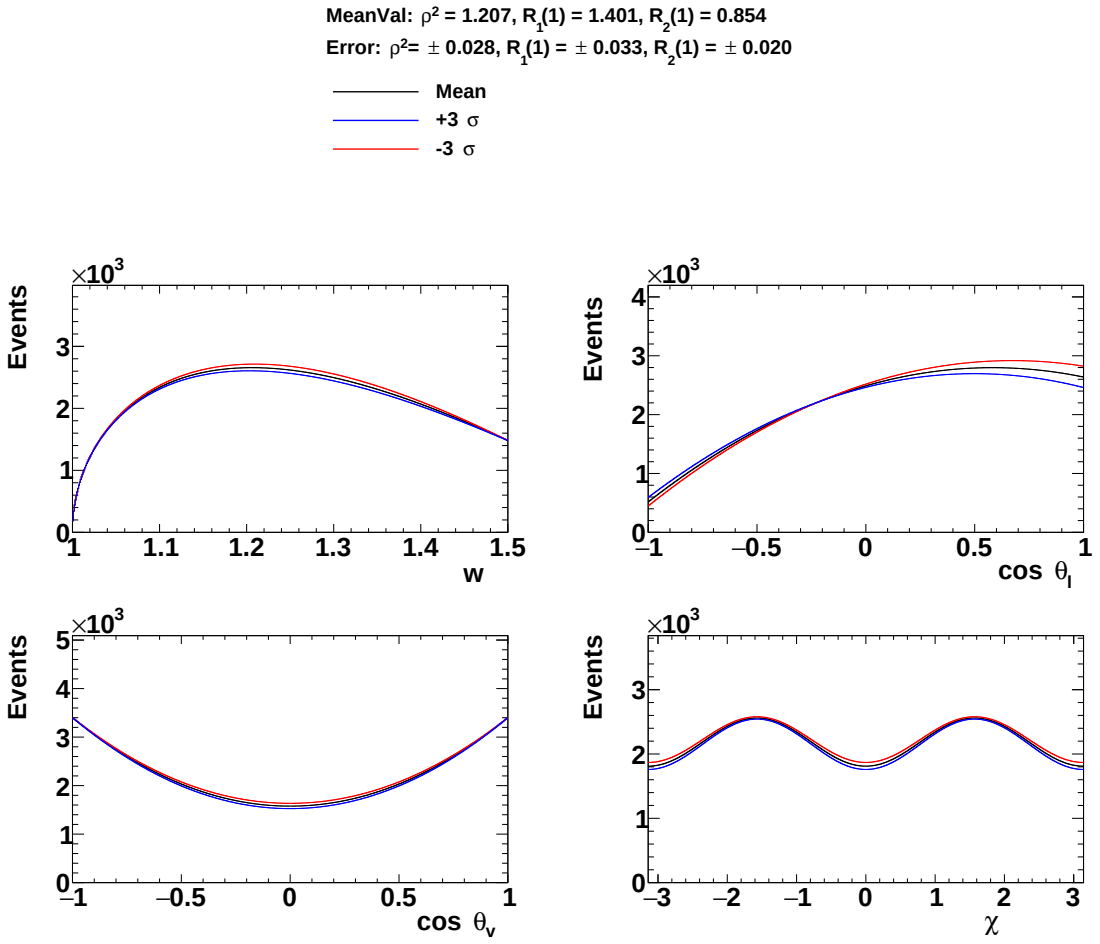

Figure 6.3: Observables modified by varying $R_1(1)$ by $\pm\, 3\sigma$.

6.3 Study of $B^0 \to D^{*-}\ell^+\nu_\ell$ Decay with NP

We furthermore examine the impact of new sources of left and right-handed operators. These studies are based on the models discussed in Chapter 4.2. The kinematic observables are examined after variations to the helicity amplitudes due to the presence of both V_L and V_R couplings. We consider real couplings only.

Figure 6.5 shows that the angular observables, $\cos\theta_\ell$ and $\cos\theta_v$, are most sensitive to the addition of positive and negative (real) right handed couplings. The shape of the recoil w distribution is more affected by a positive addition of a right handed coupling as compared to a negative addition. The amplitude of the oscillating term in the$|\chi|$ distribution can vary substantially. A combined analysis of all dimensions should allow for simultaneous fitting of form factors and new physics operators. One can also compare results separately for electrons and muons.

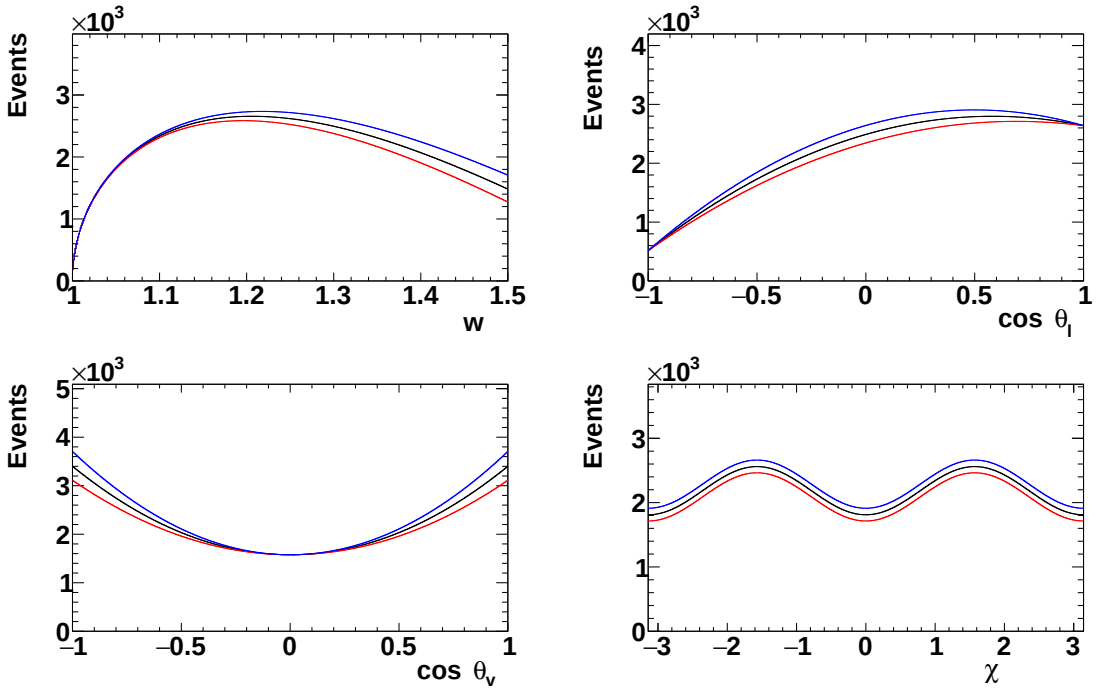

Figure 6.4: Observables modified by varying $R_2(1)$ by $\pm$ 3σ.

6.4 Reconstruction of g$B^0 \to D^{*-}\ell^+\nu_\ell$ Decays

We reconstruct the signal in the decay chain, $B^0 \to D^{*-}\ell^+\nu_\ell$ with $D^{*-} \to D^0\pi_s^-$, $D^0 \to K^-\pi^+$ while the lepton ℓ should be either a muon or an electron. This is the highest purity charm decay mode, which is critical as this is ultimately a systematics dominated analysis.

There are two charged pions in the decay; one is emitted from the D^* meson decay and is referred to as a "slow" pion, while the other is from D^0 decay. The final state particles to be reconstructed are two pions, a high momentum kaon and a light lepton. The Belle detector detects and identifies the flavour of both charged pions, one charged kaon, and leptons(e, μ) with high efficiency. These particles are reconstructed using the Belle Analysis Software Framework (BASF) [51].

Hadronic event selection is required to mitigate background events due to beam background, radiative Bhabha and other QED processes with lower track multiplicity than $B\bar{B}$ events. The criteria are based on the multiplicity of charged tracks in these events, and the visible energy deposited in the calorimeter. $B\bar{B}$ is furthermore separated from $e^+e^- \to q\bar{q}$, by applying requirements on event shape variables such as Fox-Wolfram Moments. They describe energy flow from high-energy particle collision events, introduced

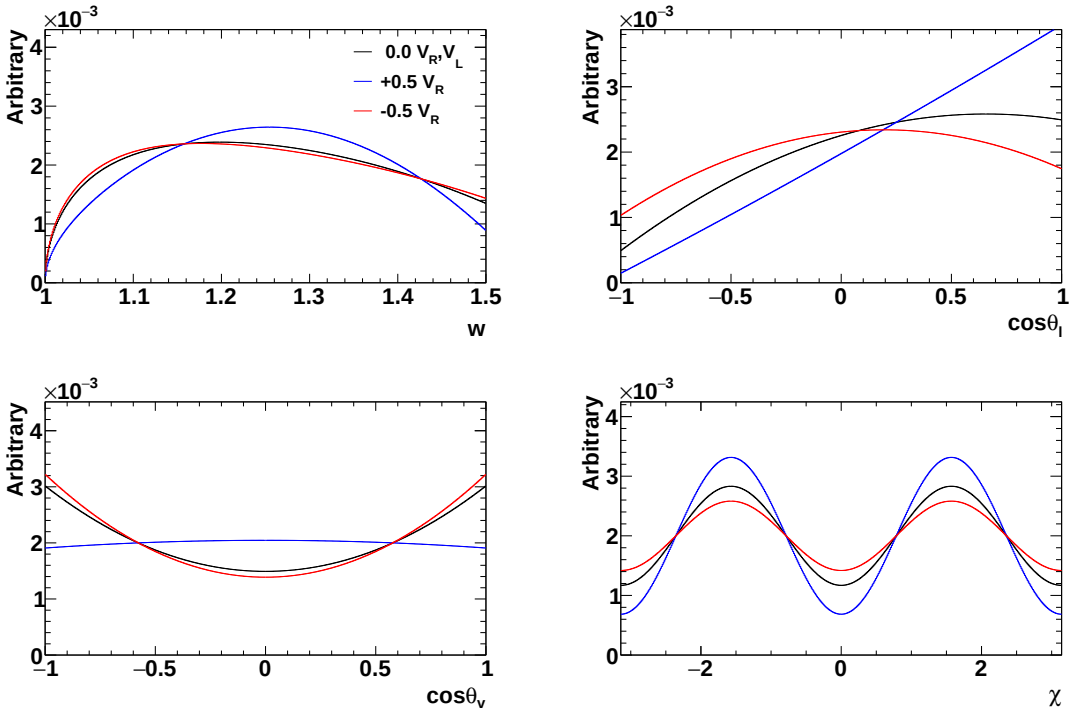

Figure 6.5: Observables modified in the presence of right-handed contributions in helicity functions.

to describe e^+e^- annihilation event shapes. A requirement is applied on the ratio of the second to zero Fox-Wolfram moments (R_2), which must be less than 0.4 [52].

6.4.1 B^0 Background

The background can be broken down into the following components.

- **Fake leptons**: processes where a hadron is misidentified as an electron or muon and is combined with a true or a fake D^*.
- **Fake** D^*: mis-reconstructed D^* combined with a true lepton.
- D^{**}: $B \to \bar{D}^{**}\ell^+\nu$ decays where $\bar{D}^{**} \to D^*n\pi$ or $B \to D^*\pi\ell\nu$ via non-resonant decay. These decay modes have charm D mesons (D, D^0, D^*, D^{**}). The excited state of charmed meson, D^{**}, is actually orbitally excited four resonances $D_0^*, D_1, D_1^{'}, D_2^*$. It has the same quark content as D meson and decay into either charged or neutral D meson(s).
- **Correlated background**:processes where a lepton and D^* come from the same

mother and decays to $B^0 \to D^{*-}\tau^+\nu$, $\tau \to \mu^+\nu\nu$ plus any other type of decay which is not signal and D^{**} background.

- **Uncorrelated background**: processes where a correctly reconstructed D^* is combined with a true lepton but they do not originate from the same B^0 meson.
- **Continuum**: processes where $D^*\ell$ candidates originate from $e^+e^- \to q\bar{q}$. The continuum is determined using off-resonance data.

6.4.2 D^0 and D^* Reconstruction

Charged particle tracks are required to originate from the interaction point, and to have good track fit quality. The criteria for the track impact parameters in the $r-\phi$ and z directions are: dr <2 cm and $|dz| < 4$ cm, respectively. In addition we require that each track has at least one associated hit in any layer of the SVD detector. For pion and kaon candidates, we use particle identification likelihoods determined using Cherenkov light yield in the ACC, the time-of-flight information from the TOF, and dE/dx from the CDC. Likelihoods for kaons and pions are considered: Kaon candidates must have a likelihood, with respect to the pion, of greater than or equal to 0.6 and the pion candidates must have likelihood, with respect to the kaon, of less than 0.6.

Neutral D^0 meson candidates are reconstructed only in the clean $D^0 \to K^-\pi^+$ decay channel. The daughter tracks are fit to a common vertex using a Kalman fit algorithm, with a χ^2-probability requirement of greater than 10^{-3} to reject background. The corresponding p-value distribution is shown in Figure 6.6. The reconstructed D^0 mass is required to be in a window of ± 13.75 MeV/c^2 from the nominal D^0 mass of 1.865 GeV/c^2, corresponding to a width of 2.5 σ determined from data.

To reconstruct the D^* candidate, the D^0 candidate is combined with a charged slow pion, (π_s^+). This slow pion is reconstructed with low efficiency, due to its very low momentum it does not pass through the whole CDC: it is therefore required to satisfy only loose impact parameter criteria, and is not required to have an associated SVD hit. To minimise prompt charm from $e^+e^- \to c\bar{c}$ continuum, the CM frame momentum of the D^* must be less than 2.45 GeV/c, as shown in Figure 6.14. The invariant mass difference between the D^* and the D candidates, $\Delta M = m_{D^*} - m_D$, is first required to be less than 165 MeV/c^2 for the background fit, and further tightened for the signal yield determination, to lie between 0.144 and 0.147 GeV/c^2. Figure 6.8 shows the ΔM distribution.

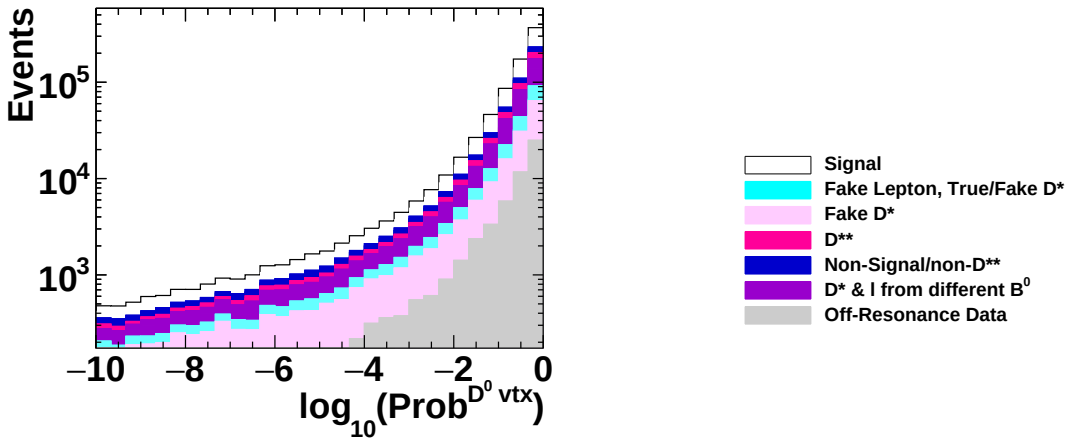

Figure 6.6: Distribution of vertex probability at D^0 vertex for selection of K and π candidates.

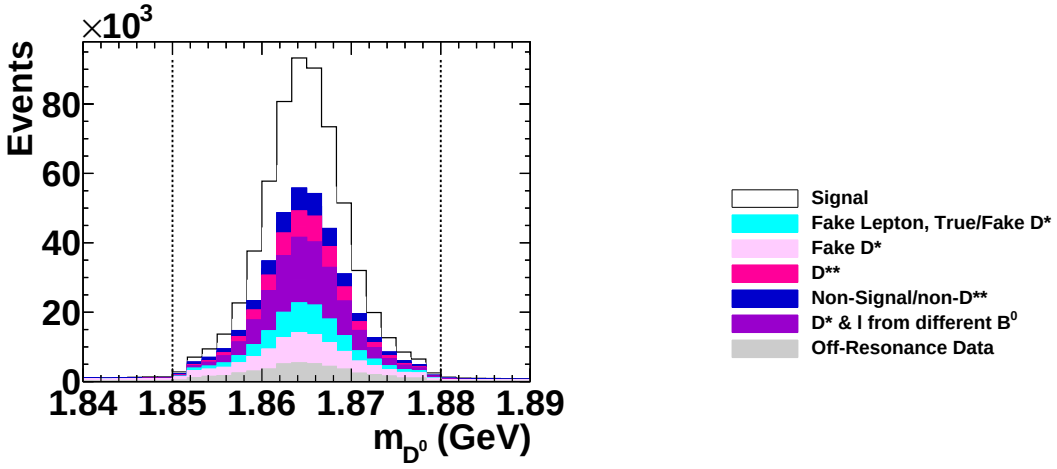

Figure 6.7: Reconstructed D^0 mass distribution distribution and the dashed line indicates 3σ mass window.

6.4.3 B^0 Candidate Selection

Candidate B mesons are reconstructed by combining D^* candidates with an oppositely charged electron or muon. Electron candidates are identified using the ratio of the energy detected in the ECL to the momentum of the track, the ECL shower shape (E9/E25), the distance between the track at the ECL surface and the ECL cluster centre, the energy loss in the CDC (dE/dx) and the response of the ACC. For electron candidates we search for nearby bremsstrahlung photons in a cone of 3 degrees around the electron track, and sum the momenta with that of the electron. Muons are identified by their penetration range and transverse scattering in the KLM detector. The angular acceptance region corresponds

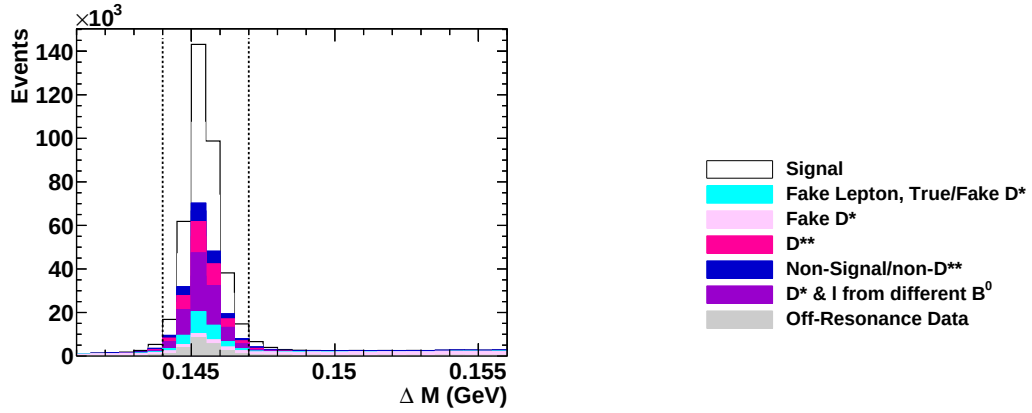

Figure 6.8: Distribution of Δ M where the dashed line indicates the signal selection. The colour scheme is defined in the Figure 6.7.

to that of the CDC, which covers the range $[17°, 150°]$ for electrons. A charged track is identified as an electron if the electron likelihood value is greater than 0.9 as shown in Figure 6.9.

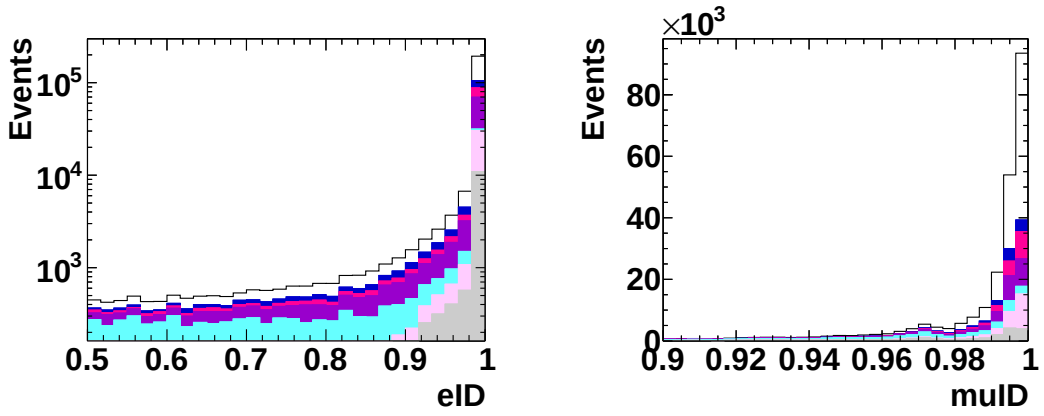

Figure 6.9: The distribution of electron and muon ID. The colour scheme is defined in Figure. 6.7.

In the momentum region relevant to this analysis, charged leptons are identified with an efficiency of about 90%, while the probabilities to misidentify a pion as an electron or muon is 0.25% and 1.5% respectively.We impose lower thresholds on the momentum of the leptons, such that they reach the respective particle identification detectors for good hadron fake rejection, as shown in Figure 6.10. To minimise the continuum background contribution, the center-of-mass frame momentum of leptons must be less than 2.4 GeV/c as shown in Figure 6.14. Tighter thresholds are applied later in the analysis procedure.

A final vertex fit is performed to reconstruct the B^0, where $D^{*+}\ell^-$ candidates are

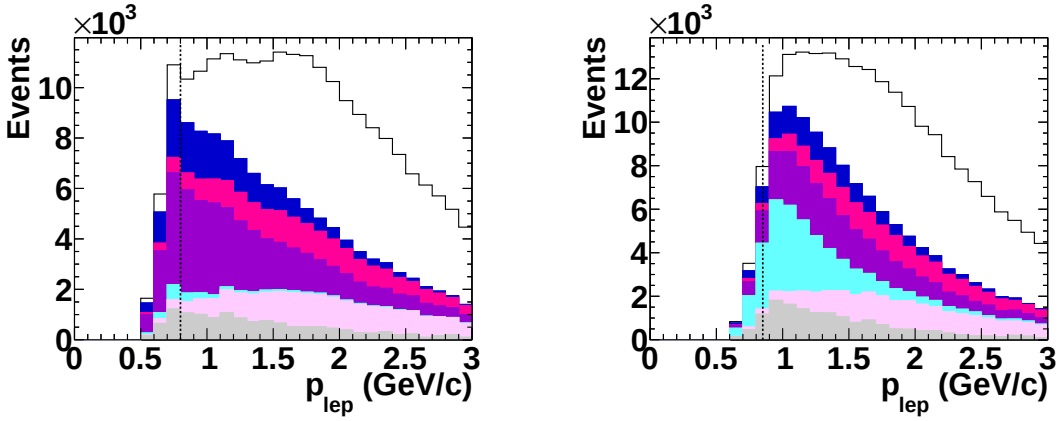

Figure 6.10: Lepton momentum distribution in the lab frame and the dashed line shows the region for signal selection. The plot on the left is for electrons and the plot on the right is for muons. The colour scheme is defined in Figure. 6.7.

rejected if the vertex probability is less than 10^{-3}. The corresponding $p-$value distribution is shown in Figure 6.11. If there are multiple B^0 candidates, the candidate with maximum vertex probability is chosen such that there is only one candidate per event.

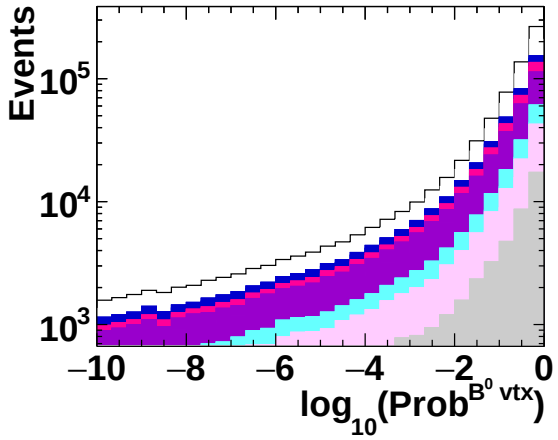

Figure 6.11: Distribution of vertex probability at B^0 vertex for $D^{*+}\ell$ candidates. The colour scheme is defined in Figure. 6.7.

6.5 Determination of the B^0 Rest Frame

To calculate the B^0 momentum, we require information about the neutrino four-momentum, but of course neutrinos are not detected in Belle, and instead we must constrain the four-vector using information about the full $\Upsilon 4(S)$ decay and known CM energy. The B^0 momentum, (p_B), can be estimated from the total momentum in the event and its direc-

tion is constrained to lie on a cone centred on the $D^{*-}\ell^+$ momentum vector as shown in Figure 6.12. The opening angle of this cone, $\theta_{B^0,D^{*-}\ell^+}$ is computed for each event. The cosine of the angle $\theta_{B^0,D^{*-}\ell^+}$ is determined by applying conservation of momentum of the $B^0 \to D^{*+}\ell^-$ decay,

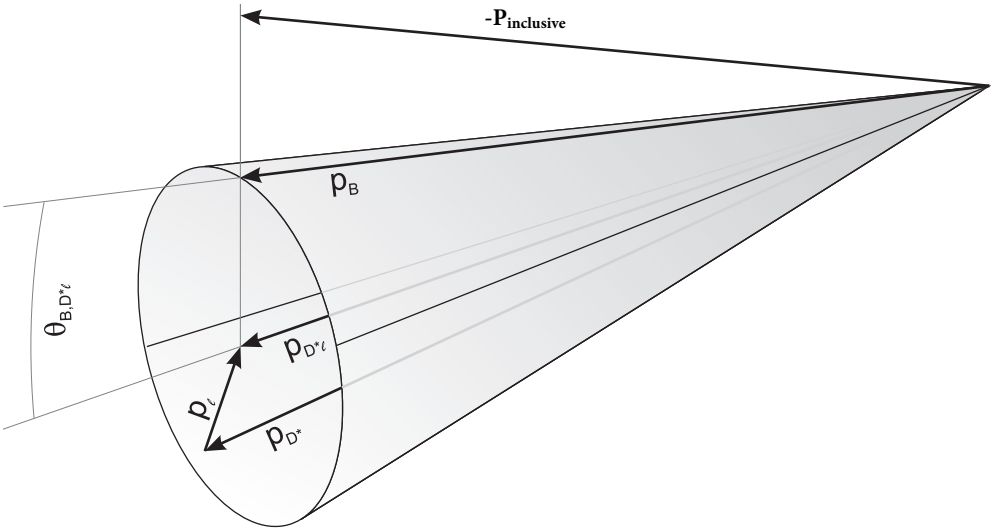

Figure 6.12: Illustration of the B^0 reconstruction technique.

$$p_B = p_{D^*} + p_\ell + p_\nu, \tag{6.1}$$

$$p_\nu = (p_B - p_{D^*\ell}). \tag{6.2}$$

By squaring Equation. 6.2 and setting $p_\nu = 0$, we get

$$\begin{aligned} 0 &= m_B^2 + m_{D^*\ell}^2 - 2\,(p_B \cdot p_{D^*\ell}), \\ 0 &= m_B^2 + m_{D^*\ell}^2 - 2\,(E_B E^*_{D^*\ell} - \vec{p^*_B}\vec{p^*}_{D^*\ell}\cos\theta_{B,D^*\ell}), \end{aligned} \tag{6.3}$$

and obtain an expression for $\cos\,\theta_{B,D^*\ell}$ as

$$\cos\theta_{B,D^*\ell} = \frac{2E^*_B E^*_{D^*\ell} - m_B^2 - m_{D^*\ell}^2}{2|\vec{p^*_B}||\vec{p^*}_{D^*\ell}|}. \tag{6.4}$$

In the above equation, the energies, masses and momenta of the D^* and the ℓ are found through particle reconstruction and E^*_B is taken from the known beam energy, $E_{\rm beam}$. The beam energy information is used to calculate the mass, energy and momentum of the B^0. The $(*)$ indicates quantities calculated in the CM frame. This is a very important variable for discriminating between signal and background, and is later used in a fit to measure the background yields.

6.5.1 Rest-of-Event and Neutrino Reconstruction

The B^0 momentum can not be reconstructed without information about the neutrino in the decay. The B^0 rest frame must be determined for accurate calculation of the kinematic variables defined in Chapter 3.3.3. The B^0 momentum is calculated using the inclusive information we derive from the rest of the event. The tracks and clusters from the other side of the decay are selected by applying the following criteria.

- **Neutral Particle Selection:** lower energy thresholds are required to mitigate beam background, which is more abundant in the forward and backward endcap regions.

E_γ **(MeV)**	θ
> 100	$\theta < 32^\circ$ (forward)
> 150	$\theta > 130^\circ$ (backward)
> 50	$32^\circ < \theta < 130^\circ$ (barrel)

- **Charged Particle Selection:** Impact parameter requirements are applied on charged tracks to ensure they originate from near the collision origin, $|dr|$ >0.4 cm and $|dz|$ >2 cm. Additional criteria are applied to reject duplicate tracks: we reject charged tracks that have a momentum difference of Δp <100 MeV/c with p_T <275 MeV/c with another track in the event. The relative angle should be $\theta < 15^\circ$ and $\theta > 165^\circ$ of the charged track and hence the track with larger value of $(5\Delta r)^2 + (\Delta z)^2$ is selected.

The inclusive momentum vector is defined as

$$\vec{p}_{\text{inclusive}} = \vec{p}_{beam} - \sum_i \vec{p}_i, \tag{6.5}$$

where $\vec{p}_{\text{beam}}$ is the total beam energy of the colliding beams it is defined as is the sum of momenta of $\vec{p}_{\text{HER}}$ and $\vec{p}_{\text{LER}}$ and $\sum_i \vec{p}_i$ is the sum of momenta of all the particles that pass the criteria discussed above. The momentum of the remaining events which are not associated with signals are shown in Figure 6.13

To estimate the four-momentum vector of the B^0, its energy component is set to be equal to $E_B^* = \sqrt{s}/2$ when transforming the $\vec{p}_{\text{inclusive}}$ vector into the CM frame. The direction of the B^0 momentum is unknown and is chosen in such a configuration where

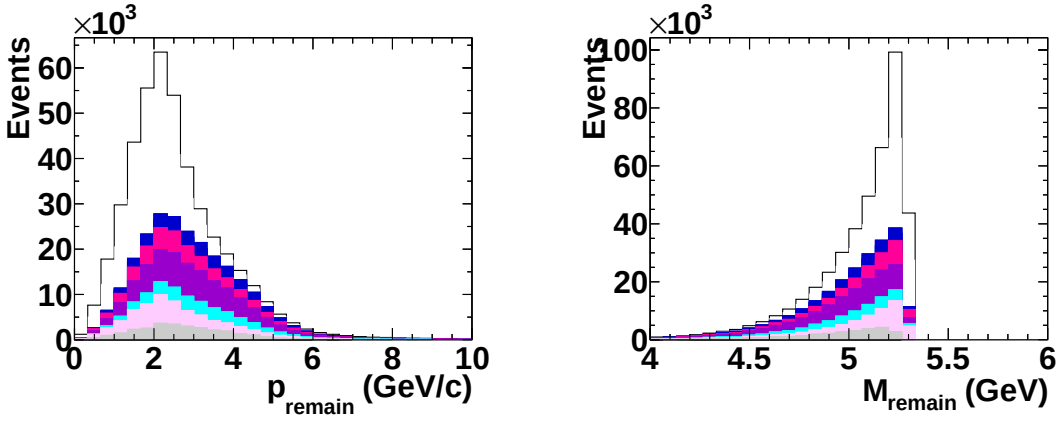

Figure 6.13: The figure on the left shows momentum of the recoil B^0. The figure on right shows the mass of the recoil B^0. The colour scheme is defined in Figure 6.7.

p_{B^0} is closest to the $\vec{p^*}_{\text{inclusive}}$ vector on a cone, as depicted in Figure 6.12. The step by step procedure to determine the signal B^0 momentum vector is described as follows.

Magnitude of recoil B^0 momentum

First we calculate the 3-momentum of the non-signal B^0 with the rest of event information in the lab frame ($\vec{r}_{\text{lab}}$) by summing momenta of all charged tracks and clusters which are not associated with signal. Calculate a boost vector from the total beam energy of the system and calculate its energy component E_{lab}. Extract the four-vector of the rest of event ($\vec{r}_{\text{lab}}$) by setting E_{lab} as its energy component in the laboratory frame. Convert the ($\vec{r}_{\text{lab}}$) four-vector to the $\Upsilon(4S)$ frame i.e. CM frame. Invert the spatial coordinates of ($\vec{r}_{\text{lab}}$) to determine the hypothesis of signal B^0 momentum four-vector.

Direction of signal B^0

We determine the axis of rotation in order to find the direction of B^0 momentum. The procedure is as follows. First consider the momentum vector $\vec{a}$ of the $D^*\ell$ system i.e. $\vec{a} = \vec{p}_{D^*\ell}$. Find a unit vector of ($\vec{a}$) where ($\hat{\mathbf{a}}$) is parallel to the spatial momentum of the $D^*\ell$ system i.e. $\hat{\mathbf{a}} = \frac{\vec{a}}{|a|}$ and $\vec{c} = \vec{r}_{\text{lab}} - (\vec{r}_{\text{lab}} \cdot \vec{a}) \times \vec{a}$. Vectors $\vec{b}$ and $\hat{\mathbf{c}}$ are orthogonal to vector $\vec{a}$ i.e. $\vec{b} = \vec{a} \times \vec{c}$ and finally the angle $\theta_{B,D^*\ell}$ is implemented via a ($\hat{\mathbf{a}}$) rotation around ($\vec{b}$).

Determination of the signal B^0 momentum

We take $\vec{a}$ as above, multiplied by the momentum 3-vector of the beam i.e. $\vec{a} \times \vec{p^*_{B^0}} = \vec{p}_{B^0}$ to derive the spatial component of the momentum vector. Then we convert $\vec{p}_{B^0}$ to a four-

vector by inserting the CM energy as the energy component of the p_{B^0}. This now provides us with the information to derive all kinematic observables for the angular analysis.

6.6 Background Estimation and corrections to the simulation

The residual background in the event is measured through a fit procedure to PDFs derived from Monte Carlo and off-resonance data. The MC background events are based on an inclusive sample of B^0 and B^+ meson decays. The branching ratios of these decays in the MC may be different to the true, measured values. Therefore, in order to ensure accurate estimation of these simulated background decays, scale factors for the simulated events are obtained by performing a fit to real data.

The simulated events are corrected for various effects. The lepton identification efficiency is corrected with weights based on $ee \to ee\gamma$, $ee \to \mu\mu(\gamma)$, and $J/\psi \to \ell^+\ell^-$ control studies, binned in lepton momentum, and polar angle [53]. The shape of the fake lepton background is corrected for both electrons and muons using misidentification probabilities measured in $D^* \to D^0\pi,\ D^0 \to K\pi$ events in bins of lepton momentum and polar angle. Efficiency corrections for low momentum tracks, specifically slow pions from D^{*+} decays are also applied, based on control studies in a dedicated $B \to D^*\ell\nu_\ell$ sample in real data [54].

To model the $B \to D^{**}\ell\nu$ component, which is comprised of four P-wave resonant modes (D_1, D_0^*, D_1', D_2^*) for both neutral and charged B decays, we correct the branching ratios and form factors. The P-wave charm mesons are categorised according to the angular momentum of the light constituent, j_ℓ, namely the $j_\ell^P = 1/2^-$ doublet of D_0^* and D_1' and the $j_\ell^P = 3/2^-$ doublet D_1 and D_2^*. The shapes of the $B \to D^{**}\ell\nu$ q^2 distributions are corrected to matched the predictions of the LLSW model [55]. An additional contribution from non-resonant modes is considered, although the rate appears to be consistent with zero in recent measurements.

After applying all the known corrections to the MC, background enhanced regions of the observables $\cos\theta_{B,D^*\ell}$, $\Delta m = m_{D^*} - m_{D^0}$, and lepton momentum are used to determine the background yields. In the $\cos\theta_{B,D^*\ell}$ distribution, the signal process should lie in interval $(-1, 1)$ while the region outside this interval i.e. $(-10, 5)$ is used to determine

the background contributions. ΔM should lie in the region between 0.144 and 0.147 GeV/c^2, while the region outside of this range is used to determine the background from fake D^* candidates. The momentum of the lepton is an important variable to determine fake lepton background. p_ℓ is defined in the range with minimum value of 0.3 (0.6) GeV/c for electron (muon) and maximum value of 3.0 GeV/c in the lab frame. Events are required to have lepton momenta greater than 0.8 GeV/c for electrons and greater than 0.85 GeV/c for muons. This criterion greatly reduces the contamination from pions and kaons misidentified as leptons.

6.6.1 Continuum background

Prior to the fit to determine the background yield, the continuum background is subtracted using off-resonance data collected 60 MeV below the $\Upsilon(4S)$. The normalisation of this component is calculated using the on-to-off resonance luminosity ratios separately for the SVD1 and SVD2 samples, which have a 1% systematic uncertainty. The normalisation ratio is further corrected for the CM energy dependence of the cross section for $e^+e^- \to q\bar{q}$. The on-to-off ratio is examined in the event sphericity distribution, R_2 (0 is spherical, 1 is jet-like), and in the momentum distribution of D^* (in the CM frame). This is shown in Figure 6.14. In the B decay depleted regions, $R_2 > 0.25$ and $p^*_{D^*} > 2.5$ GeV/c there is excellent agreement between on- and off-resonance data.

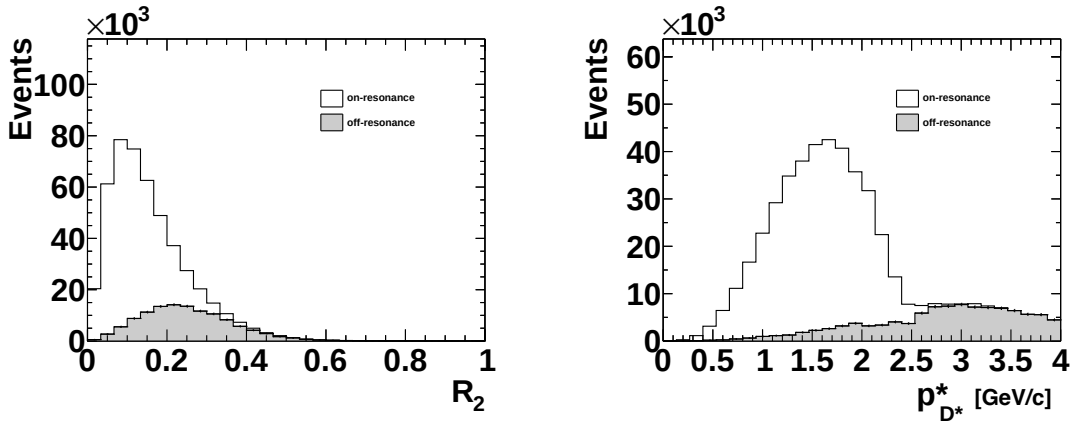

Figure 6.14: The distribution of R_2 and momentum of D^* show good agreement between on- and off-resonance data.

6.6.1.1 Continuum Calibration

While the expected number of events from off-resonance appears to be correct, the kinematic distributions differ slightly due to the difference in centre of mass energies. We derived weight factors in all kinematics bins and in $\cos\theta_{D^*\ell}$, to correct for these differences, which are most prominent at $\cos\theta_\ell$ near -0.5 and at large hadronic recoil w. Figure 6.15 shows the $\cos\theta_{D^*\ell}$ and w distributions of the MC expectation for the continuum on-resonance and off-resonance, with the off-resonance data overlaid, for the region $-0.6 < \cos\theta_\ell < -0.4$.

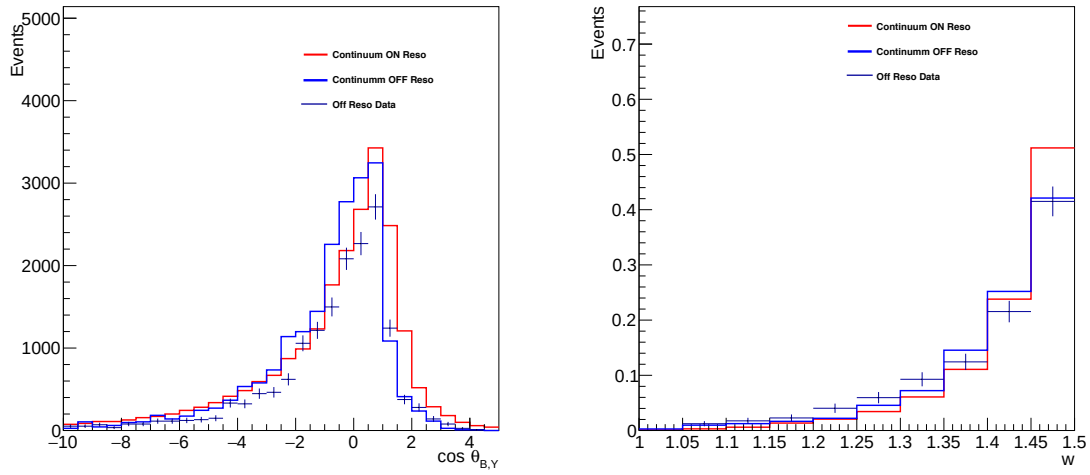

Figure 6.15: The $\cos\theta_{B,D^*\ell}$ and w distributions (normalised) showing on-resonance MC, off-resonance MC and off-resonance data of the SVD1 electron sub-sample.

6.7 Background fit

A three dimensional (3D) distribution of the observables ($\cos\theta_{B,D^*\ell}$, Δm, p_ℓ) is used to fit the background yields using RooFit [56]. A binned extended maximum likelihood fit is performed using signal and background histogram PDFs. These PDFs are modelled using MC simulation with ten times the expected yield in real data. Continuum $q\bar{q}$ is modelled using off resonance data therefore it is not floated in the fit and is subtracted from the on resonance data before the fit is performed. Signal, and the remaining background components are floated in the fit to extract the yield. The mass difference Δm is a powerful discriminator between fake and true D^*, $\cos\theta_{B,D^*\ell}$ separates out background

from $B \to D^{**}\ell\nu$ and $D*$ and ℓ from different B, while p_ℓ provides a constraint on the fake ℓ yield (which is relatively small). The bin ranges are as follows:

- Δm: 5 equidistant bins in the range [141, 156] MeV/c^2.
- $\cos\theta_{B,D*\ell}$: 15 equidistant bins in the range [−10, 5].
- p^*_ℓ: 2 bins in the ranges [0.6, 0.85, 3.0] GeV/c for muons and [0.3, 0.80, 3.0] GeV/c for electrons.

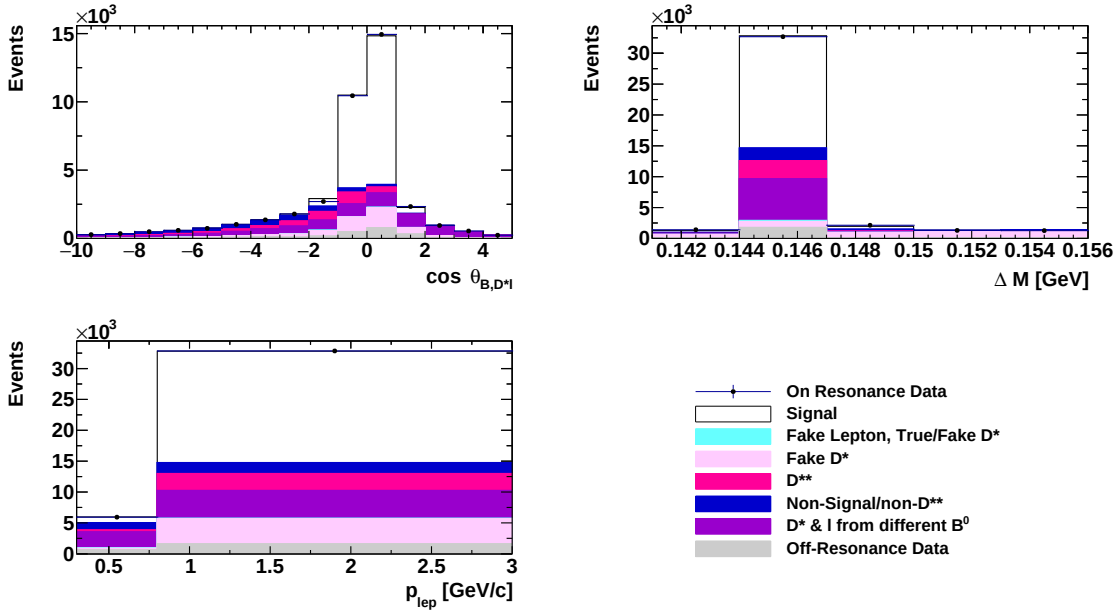

Figure 6.16: The projections of the ($\cos\theta_{B,D^*\ell}$, Δm, p_ℓ) distributions after the fit, for the sample SVD1(e).

Figures 6.16 to 6.19 show the projections of the fit results after performing the fit to data for four subsamples: SVD1, SVD2 for electron and muon modes respectively. Using the signal and background yields from the fit, scale factors are calculated based on the ratio of fitted yield to the MC expected yield of each component. These scale factors are later used to correct the background yield expectation in the analysis of the kinematic variables ($w, \cos\theta_\ell, \cos\theta_v, \chi$) for the measurement of $|V_{cb}|$ and form factor parameters. The scale factors are listed in Table 6.1. The signal and background fractions are determined in the signal window of the fitted distributions: $-1 < \cos\theta_{B,D^*\ell} < 1$, 144 MeV/$c^2$ $< \Delta M <$ 147 MeV/c^2, and $p_\ell > 0.8$ GeV.

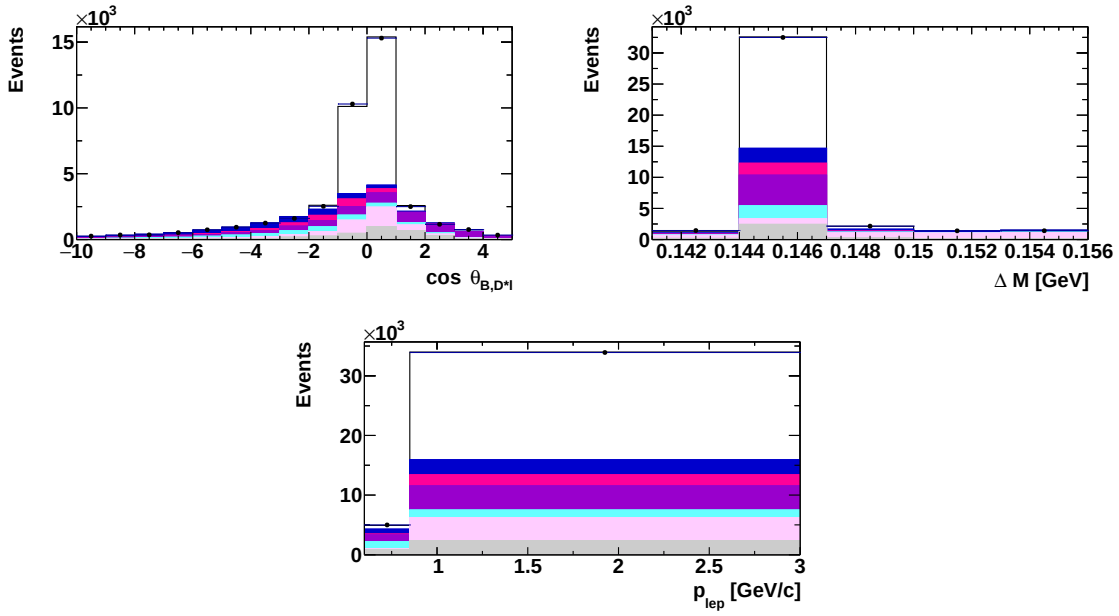

Figure 6.17: The projections of the ($\cos\theta_{B,D^*\ell}$, Δm, p_ℓ) distributions after the fit, for the sample SVD1(μ). The colour scheme is defined in Figure 6.16.

Table 6.1: Signal and background scale factors from fit in the signal region. The errors on the scale factors are calculated from the fit.

	SVD1(e)	**SVD1(μ)**	**SVD2 (e)**	**SVD2 (μ)**
Signal Events	0.949 ± 0.007	0.947 ± 0.006	0.949 ± 0.002	0.938 ± 0.002
Fake ℓ	0.432 ± 0.806	0.456 ± 0.204	0.380 ± 2.984	0.356 ± 0.119
Fake D^*	0.973 ± 0.023	0.922 ± 0.019	1.034 ± 0.005	1.004 ± 0.005
D^{**}	0.801 ± 0.056	0.574 ± 0.035	0.714 ± 0.019	0.511 ± 0.012
Signal Corr.	0.833 ± 0.223	1.265 ± 0.244	0.944 ± 0.048	1.476 ± 0.089
Uncorrelated	0.810 ± 0.070	0.806 ± 0.094	0.769 ± 0.023	0.929 ± 0.045

6.7.1 Validation of the Background Fit

Tests are performed to validate the fit procedure, error evaluation and to determine any possible bias, namely a pull test and a “stream test", which are described in turn.

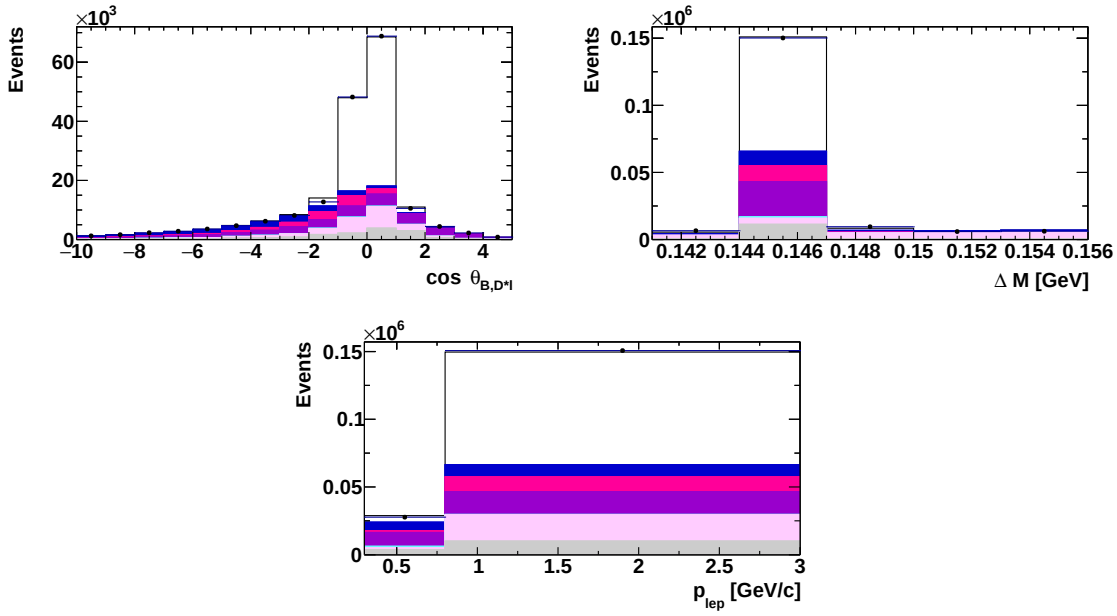

Figure 6.18: The projections of the ($\cos\theta_{B,D^*\ell}$, Δm, p_ℓ) distributions after the fit, for the sample SVD2 (e). The colour scheme is defined in Figure 6.16

Table 6.2: Signal and background fractions (%) for events selected in the signal region of ($|\cos\theta_{B,D^*\ell}|<1$, $0.144 < \Delta m < 0.147$, $p_e > 0.80$, $p_\mu > 0.85$)

	SVD1(e)	**SVD1(μ)**	**SVD2 (e)**	**SVD2 (μ)**
No. of Signal Cand.	19318	19748	88622	87060
Signal Events	83.31 ± 0.60	83.84 ± 0.54	84.80 ± 0.19	84.20 ± 0.21
Fake ℓ	0.10 ± 0.17	1.16 ± 0.73	0.10 ± 0.82	1.21 ± 0.40
Fake D^*	3.17 ± 0.10	3.02 ± 0.06	3.08 ± 0.014	2.96 ± 0.02
D^{**}	6.07 ± 0.42	4.19 ± 0.25	5.32 ± 0.14	3.82 ± 0.09
Signal Corr.	1.29 ± 0.35	2.08 ± 0.40	1.49 ± 0.07	2.52 ± 0.15
Uncorrelated	6.05 ± 0.52	5.23 ± 0.61	5.19 ± 0.15	5.27 ± 0.26
Continuum	4.29 ± 0.67	4.64 ± 0.77	4.68 ± 0.40	5.43 ± 0.47

6.7.1.1 Pull Test

The pull of a variable is defined as

$$\text{pull} = \frac{\text{Fitted value - Expected value}}{\text{Fit Error}}. \tag{6.6}$$

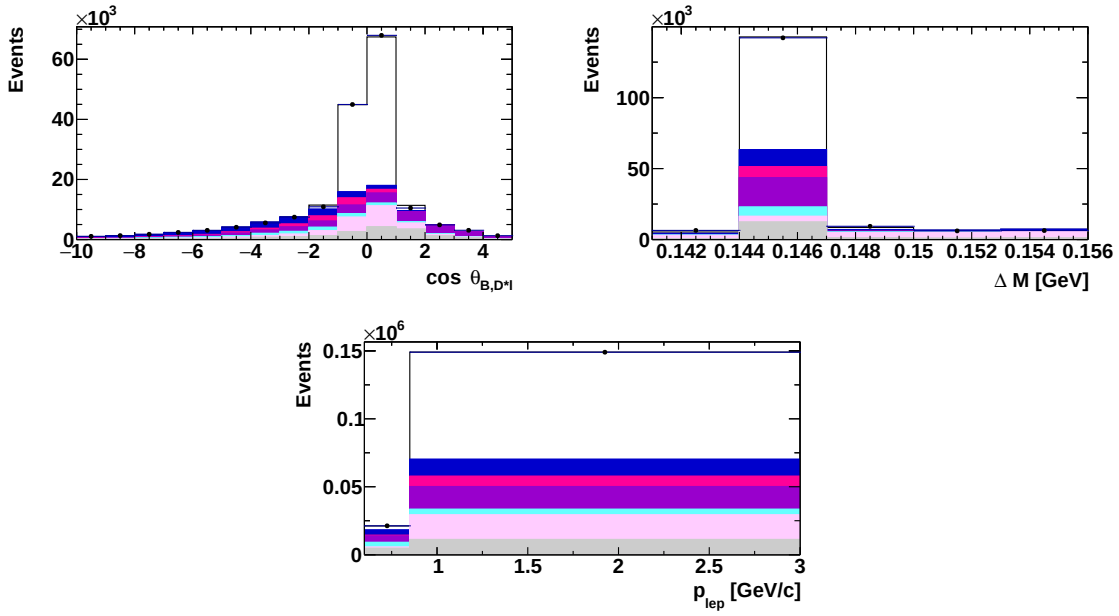

Figure 6.19: The projections of the ($\cos\theta_{B,D^*\ell}$, Δm, p_ℓ) distributions after the fit, for the sample SVD2 (μ). The colour scheme is defined in Figure 6.16

The pull is determined separately for each sub sample (SVD1e, SVD1μ, SVD2e, SVD2μ) by building 2000 toy MC samples, taking the original histogram PDFs. The pull distributions are then fitted with single Gaussians. Figures 6.20, 6.21, 6.22 and 6.23 show the pull distributions for all samples. The distributions show that the mean is consistent with 0, and the width (σ) is consistent with 1 for the signal and each the background components. The pull test also shows that the fitting procedure is reliable and there is no indication of bias.

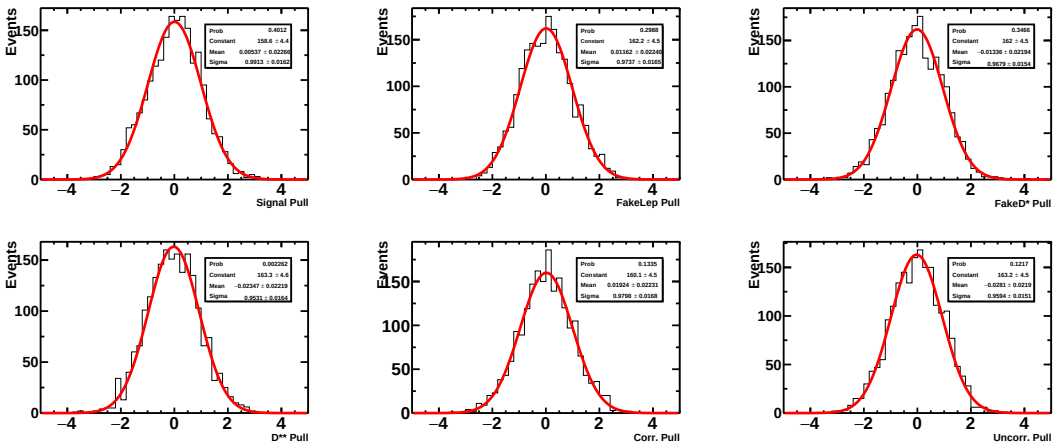

Figure 6.20: The pull distributions of the sample SVD1 for (e) mode.

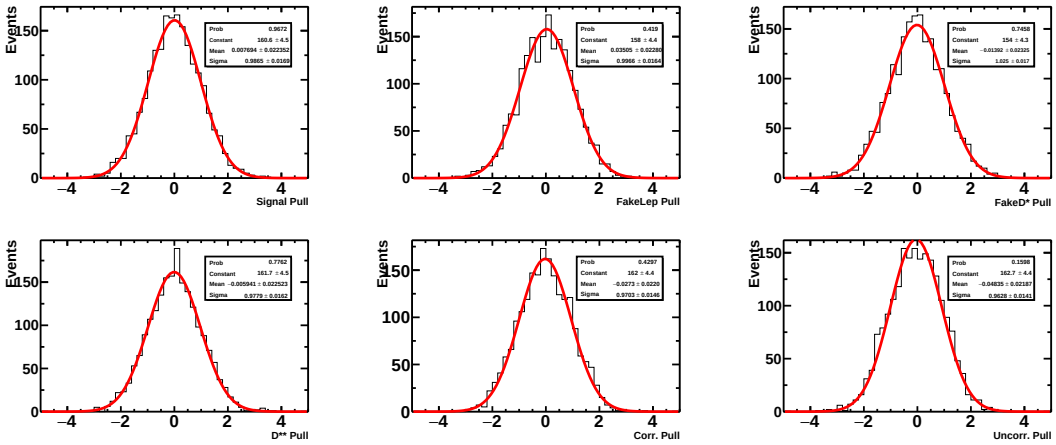

Figure 6.21: The pull distributions of the sample SVD1 for (μ) mode.

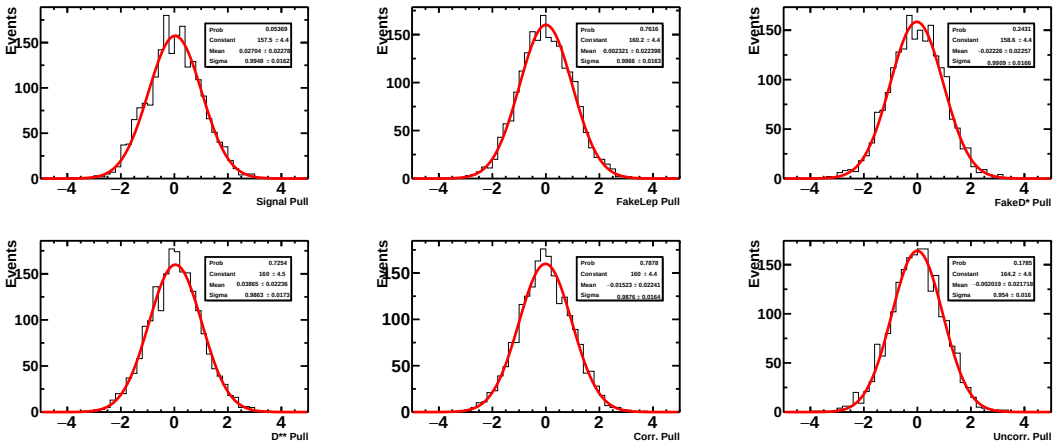

Figure 6.22: The pull distributions of the sample SVD2 for (e) mode.

The mean and the standard deviations from the pull results are summarised in Figure 6.24. The results for all the subsamples are consistent within their respective errors, with just a slight tendency to overestimate uncertainties in the fit by around 1-2% on average. This has negligible impact on the final results.

6.7.1.2 Stream Test

A so called “stream test" is performed to check the fit procedure for any possible bias using the MC data. In this procedure, one stream of MC data, which is equal to the total integrated luminosity of the real data, is taken as pseudo data to perform the fit while the remaining 9 streams are used to model the background PDFs in the fit. The fit should give the same normalisation factors for each component with each stream, within uncertainty. The ratio of signal and background components from the fit and the MC should be 1.0,

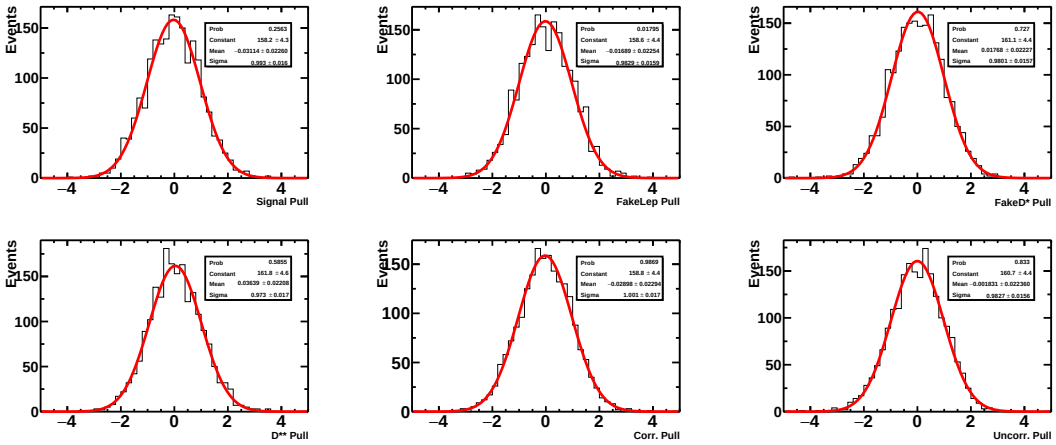

Figure 6.23: The pull distributions of the sample SVD2 for (μ) mode.

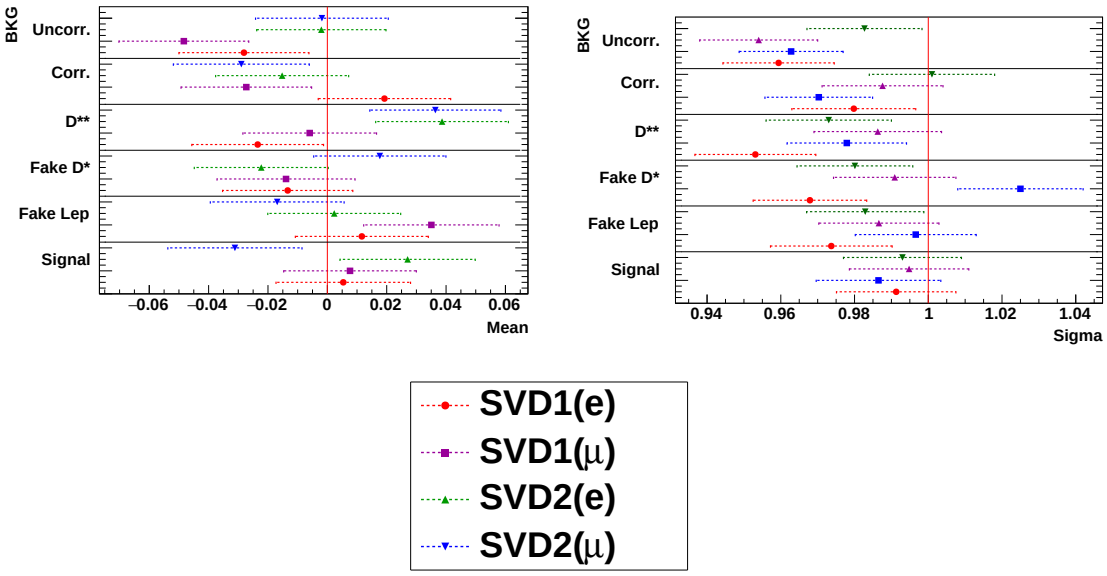

Figure 6.24: Mean and standard deviation from the pull test for all sub samples.

which would show perfect agreement between MC in each stream sub-sample as well as show fit stability.

$$\text{Normalisation} = \frac{\text{Fit Value}}{\text{MC Expectation Value}} \approx 1.0. \tag{6.7}$$

Figures 6.25 to 6.28 show the results for the stream test for all samples. There is no indication bias in the stream test for all the samples. This implies the fit method is stable. All the data samples are statistically independent and statistically consistent results are obtained from all the fits.

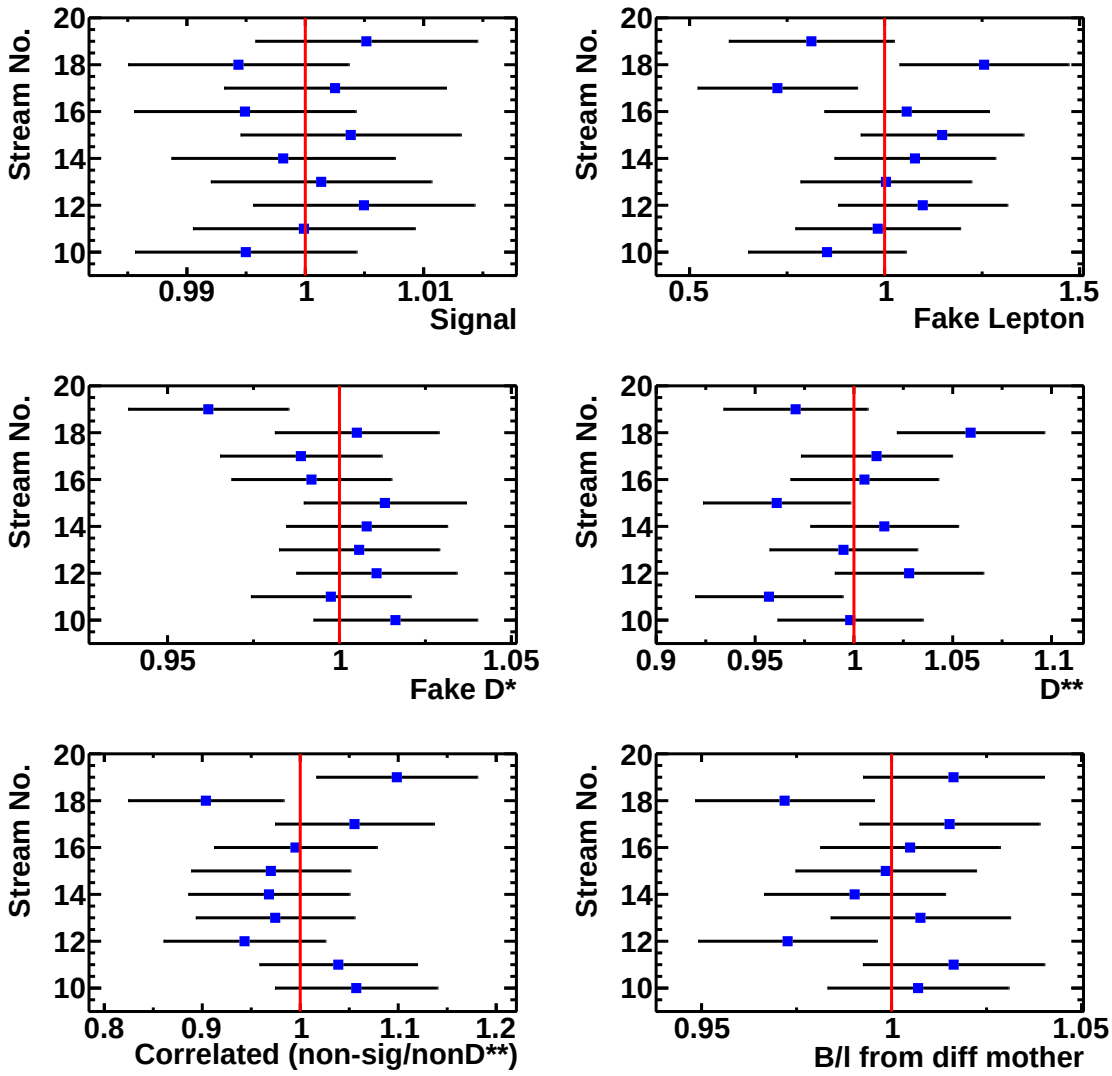

Figure 6.25: Stream Test for SVD1(e). Definitions of the background are in Section. 6.4.1

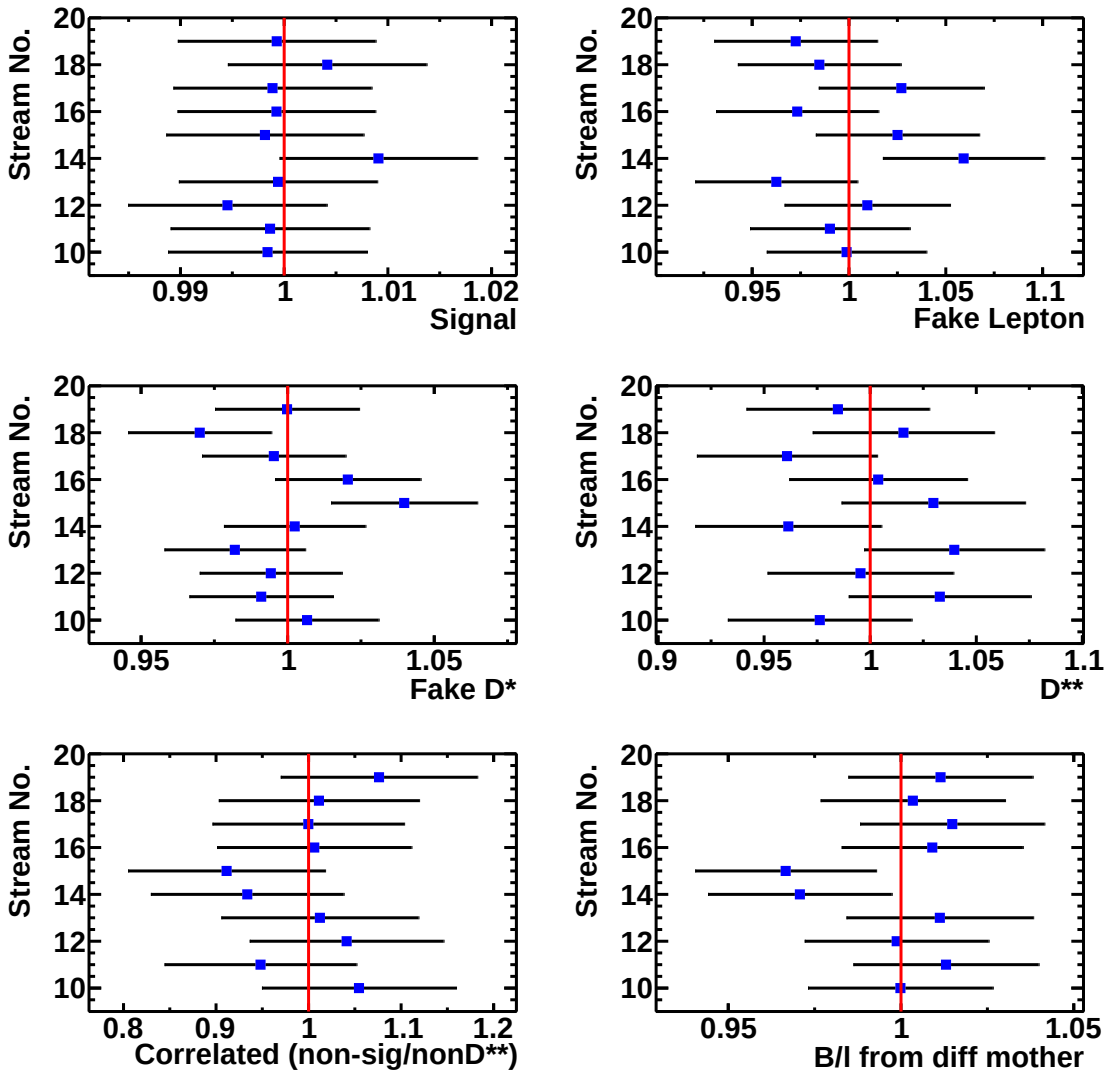

Figure 6.26: Stream Test for SVD1(μ). Definitions of the background are in Section. 6.4.1

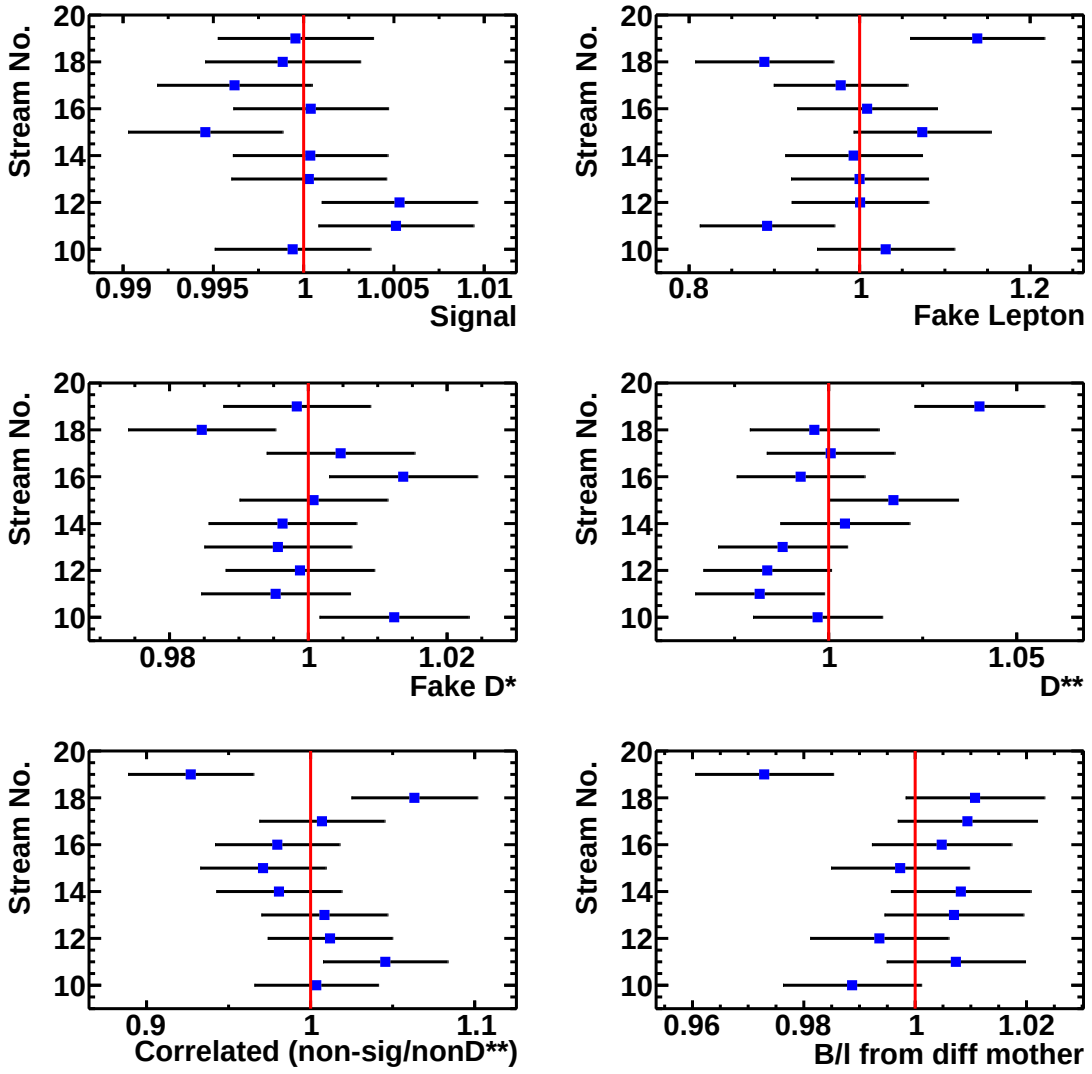

Figure 6.27: Stream Test for SVD2(e). Definitions of the background are in Section. 6.4.1

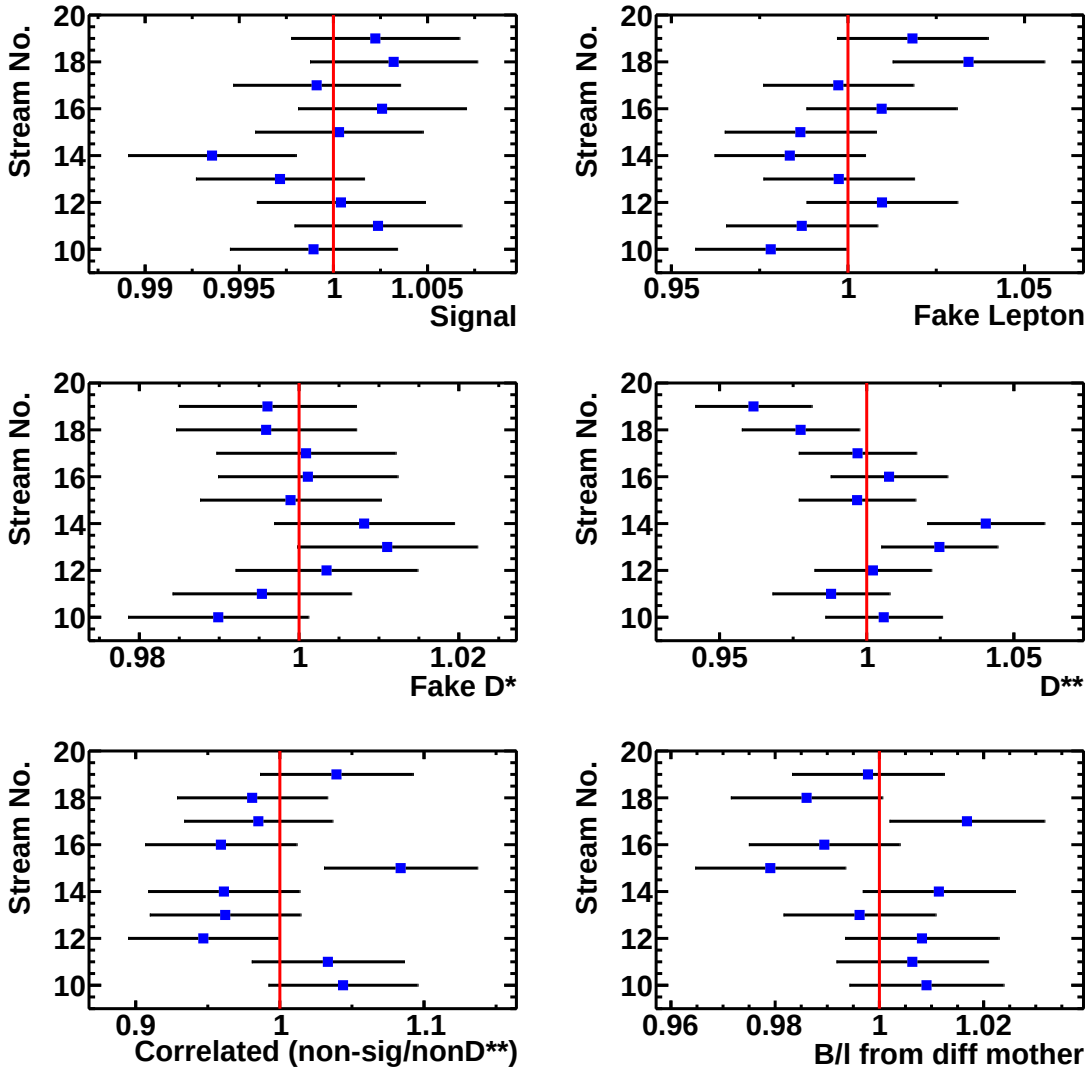

Figure 6.28: Stream Test for SVD2(μ). Definitions of the background are in Section. 6.4.1

6.7.2 Resolution of Kinematic Variables

Resolution is defined as $\delta = v^{rec} - v^{true}$, where the v^{rec} is the reconstructed value of the variable and v^{true} is the true value. The resolution tells us how effective the reconstruction algorithm is at measuring the decay distributions. A crude quantitative measure of resolution is obtained by fitting the δ distribution with a (double) gaussian distribution. Resolution is small compared to the bin width of each observable $(w, \cos\theta_\ell, \cos\theta_{\rm v}, \chi)$ which tells us that bin migration is reasonably small. The resolution for SVD2 is slightly better than SVD1 $\cos\theta_{\rm v}$ due to better slow pion tracking. The weighted average width is

determined for each sample, defined as follows,

$$\sigma_{total} = \sqrt{\frac{f_1}{(f_1+f_2)}\sigma_1^2 + \frac{f_2}{(f1+f_2)}\sigma_2^2}. \tag{6.8}$$

Using the above equation the resolutions for the kinematic variables are tabulated in Table 6.7.2 and the fitted resolution plots are shown in the Figure 6.29 and 6.30 for SVD1 and SVD2 respectively. SVD1 and SVD2 have identical resolution except $\cos\theta_{\rm v}$ which is sensitive to slow pion reconstruction.

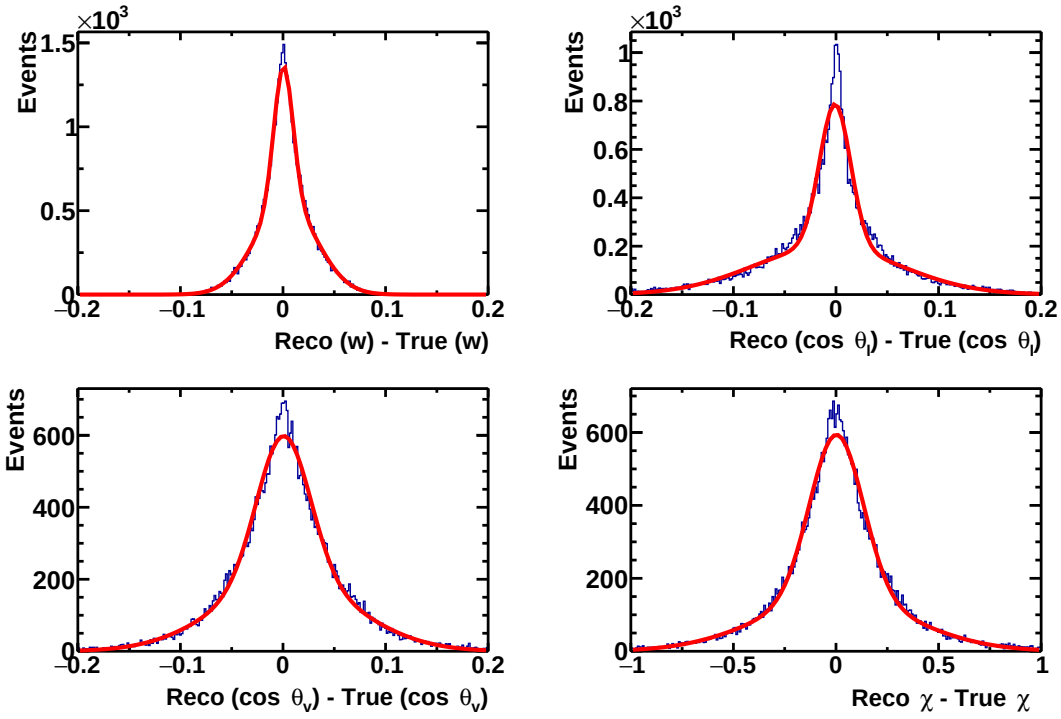

Figure 6.29: Resolution of kinematic variables for SVD1($e+\mu$) Sample.

Table 6.3: Resolution of the kinematic variables w, $\cos\theta_\ell$, $\cos\theta_{\rm v}$ and χ.

Variable	Bin Width	SVD1($e+\mu$)	SVD2 ($e+\mu$)
w	0.05	0.020	0.020
$\cos\theta_\ell$	0.20	0.038	0.038
$\cos\theta_{\rm v}$	0.20	0.044	0.043
χ	0.63	0.210	0.210

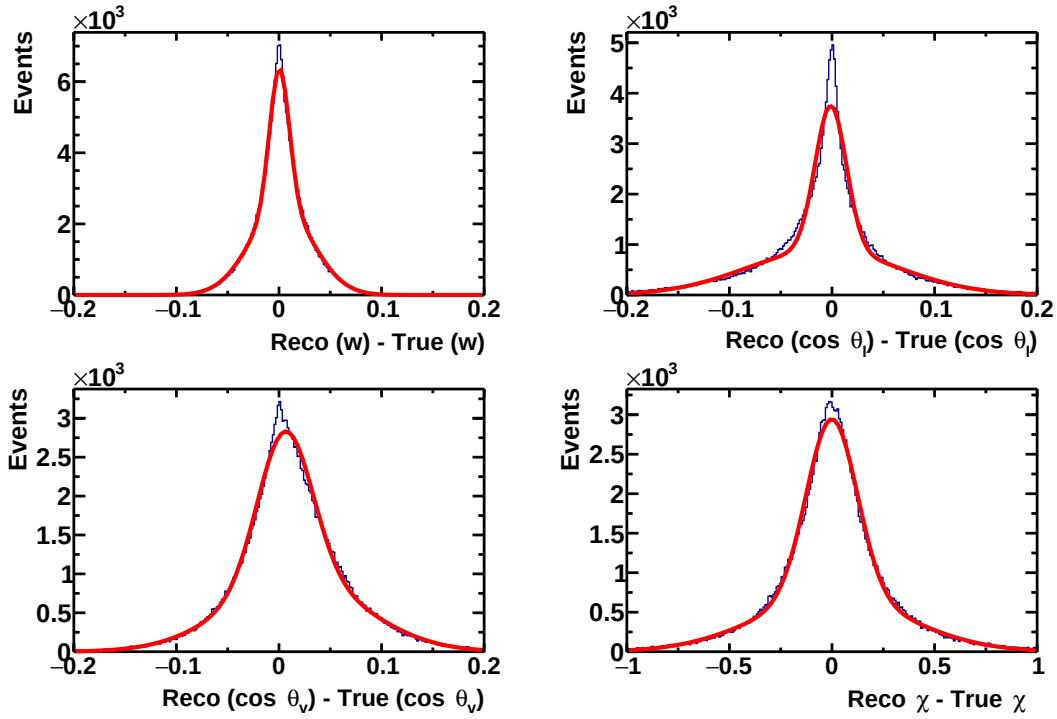

Figure 6.30: Resolution of kinematic variables for SVD2($e + \mu$) Sample.

6.7.3 Efficiency

Efficiencies are calculated separately for each subsample, defined as

$$\text{Efficiency} = \frac{\text{No. of Events After Signal Selection}}{\text{Total Generated Events}}, \tag{6.9}$$

and summarised in Table 6.4. Electrons and muon modes are reconstructed with similar efficiencies. The efficiency for the SVD2 sub-sample is higher by approximately 10% owing to the additional silicon detector layer.

Table 6.4: Efficiency in each sample, where the error is due to finite MC statistics.

Data Sample	Efficiency Value
SVD1 (e)	0.0821 ± 0.0007
SVD1 (μ)	0.0831 ± 0.0008
SVD2 (e)	0.0930 ± 0.0003
SVD2 (μ)	0.0913 ± 0.0003

Towards the zero recoil point, $w = 1$, the D^* meson is at rest so the momentum transfer

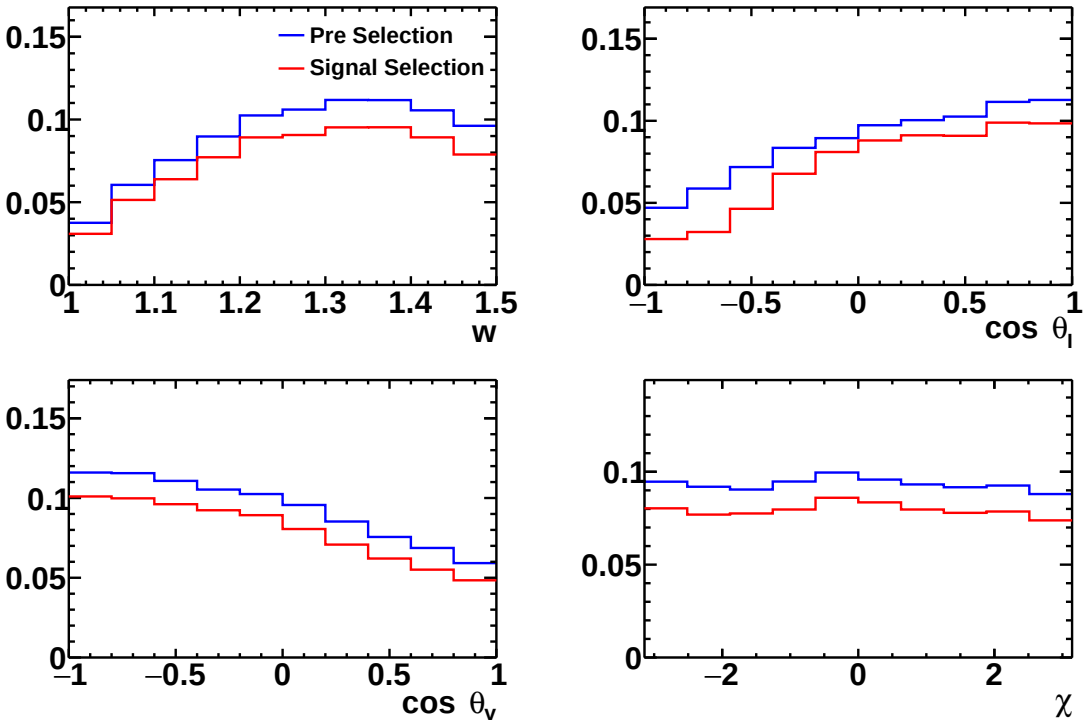

Figure 6.31: Binned efficiencies in the four kinematic variables w, $\cos\theta_\ell$, $\cos\theta_\mathrm{v}$ and χ.

is minimum and the efficiency decreases. In the case of $\cos\theta_\mathrm{v}$, the efficiency drops when the angle between D^* and D^0 meson is zero and the D^* carries minimum momentum. Figure 6.32 shows the high correlation between $\cos\theta_\mathrm{v}$ and slow pion momentum. The drop in efficiency at low $\cos\theta_\ell$ is due to low momentum leptons when the momentum transfer is zero between the W and charged lepton as shown in Figure 6.32. The efficiency remains flat in χ before and after the signal selection criteria, which suggests that acceptance is flat across this spectrum. After correct background estimation and calculation of efficiencies for all sub-samples, we will establish the fit procedure to extract $\mathcal{F}(1)|V_{cb}|$ and form factor parameters in two parameterisation schemes.

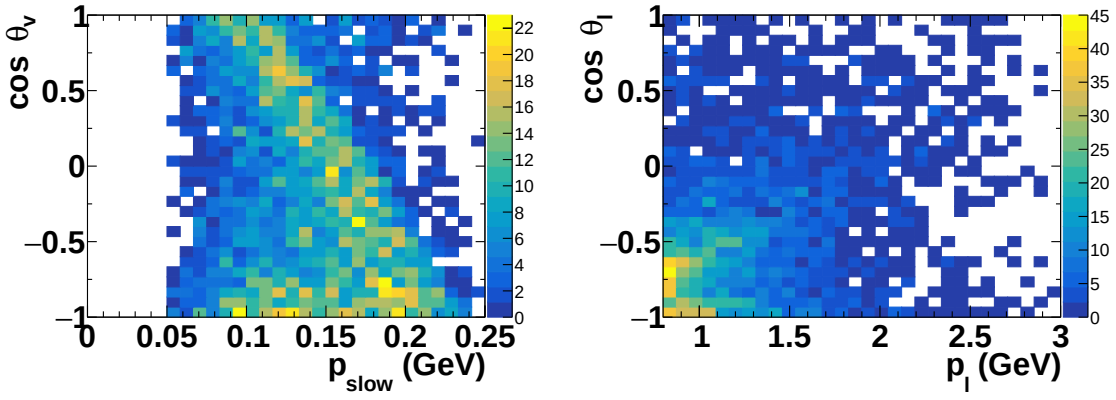

Figure 6.32: Two dimensional distribution of D^* decay angle and slow pion momentum (left) in the reconstructed signal MC. Two dimensional distribution of lepton helicity angle and lepton momentum (right).

7. Fit for $\mathcal{F}(1)|V_{cb}|$ in the CLN scheme

7.1 Fit Procedure

This chapter describes the fit procedure used to extract the CLN form factor parameters $(\rho^2, R_1(1), R_2(1))$ and $\mathcal{F}(1)|V_{cb}|$. A similar procedure is applied in a later chapter to fit to the BGL scheme. In both schemes, the parameters of interest are extracted using a binned χ^2 fit (with ROOT TMinuit), to the one-dimensional projections of kinematic variables w, $\cos\theta_\ell$, $\cos\theta_v$ and χ. Bin to bin correlations are taken into account. Each variable is divided into 10 bins such that there are a total of 40 bins in the χ^2 fit. The events produced in each bin are calculated as follows [37],

$$N_i^{\text{prod}} = N_{B^0}\,\mathcal{B}(D^{*+} \to D^0\pi^+)\,\mathcal{B}(D^0 \to K^-\pi^+)\,\tau_{B^0}\,\Gamma_i, \tag{7.1}$$

where Γ_i is the differential decay width calculated in that specific bin by integrating Equation 3.42 in the kinematic variable corresponding to the bin i from the lower to the upper boundary of that bin, while integrating the remaining variables over their full range. N_{B^0} is the number of B^0s in the data sample. $\mathcal{B}(D^{*+} \to D^0\pi^+)$ and $\mathcal{B}(D^0 \to K^-\pi^+)$ are branching ratios of D^* and D^0 meson respectively and τ_{B^0} is the lifetime of B^0. The bin index "i" refers to the bins of variable w from $i = 1$ to $i = 10$, $\cos\theta_\ell$ from $i = 11$ to $i = 20$, $\cos\theta_v$ from $i = 21$ to $i = 30$ and χ from $i = 31$ to $i = 40$ for variable. The CLN parameterisation of the form factors is described in Chapter 3.3.2, which is used to extract $(\rho^2, R_1(1), R_2(1))$ and $\mathcal{F}(1)|V_{cb}|$ from the fit. The normalisation of the form factor $h_{A_1}(w)$ at zero recoil, $h_{A_1}(1) = \mathcal{F}(1)$, is taken from from unquenched lattice QCD calculations [57],

$$\mathcal{F}(1) = 0.906 \pm 0.004 \pm 0.012. \tag{7.2}$$

Here the first error is statistical and the second is the sum of all systematic errors in quadrature. The number of expected events in each bin are calculated as follows,

$$N_i^{\rm exp} = \sum_{j=1}^{40} R_{ij}\,\epsilon_j\,N_j^{\rm th} + N_i^{\rm bkg}, \tag{7.3}$$

where $R_{i,j}$ is the detector response matrix (the probability of finding a true generated value in a given reconstruction bin) and ϵ_j is the binned signal efficiency. Both these quantities are calculated with MC samples corrected for imperfections in the simulation, as described in the previous Chapter. The background in each bin is calculated as described in Chapter 6.7. The events thats are generated in this decay can be calculated as,

$$N^{\rm Events} = N_{B^0}\mathcal{B}(D^0 \to K^-\pi^+)\,\mathcal{B}(D^{*+} \to D^0\pi^+)\,\mathcal{B}(B^0 \to D^{*+}\ell\nu_\ell). \tag{7.4}$$

The input variables and their values that enter in the fit are given in Table 7.1.

Table 7.1: Values of the input variables for the fit.

Variable	**Value**
Γ	2.05129×10^{-14}
N_{B^0}(SVD1)	152×10^6
N_{B^0}(SVD2)	620×10^6
$\mathcal{B}(B^0 \to D^{*-}\ell^+\nu_\ell)$	(4.93 ± 0.11) %
$\mathcal{B}(D^{*+} \to D^0\pi^+)$	(67.7 ± 0.5) %
$\mathcal{B}(D^0 \to K^-\pi^+)$	(3.93 ± 0.04) %
τ_{B^0}	$(1.52 \pm 0.005)\times 10^{-12}$ s
$\mathcal{G}_\mathcal{F}$	1.166378×10^{-5} GeV^{-2}
m_{B^0}	5279 ± 0.15 MeV
m_{D^*}	2010.26 ± 0.05 MeV
m_{D^0}	1864.83 ± 0.05 MeV
ρ^2	1.301 (Belle MC)
$R_1(1)$	1.181 (Belle MC)
$R_2(1)$	0.710 (Belle MC)

The χ^2 function for the fit is calculated as:

$$\chi^2 = \sum_{i,j} (N_i^{\rm obs} - N_i^{\rm exp}) C_{ij}^{-1} (N_j^{\rm obs} - N_j^{\rm exp}), \tag{7.5}$$

where $N_i^{\rm obs}$ are the number of events in bin i of our data sample, and C_{ij}^{-1} is the inverse of the covariance matrix. The covariance matrix is actually the variance-covariance matrix whose diagonal elements are the variances and the off-diagonal elements are the covariance for elements from the i^{th} and j^{th} position. The covariance is calculated by having the variables w, $\cos\theta_\ell$ and $\cos\theta_{\rm v}$ and χ against each other. The off-diagonal elements are calculated as in Ref. [37],

$$C_{ij} = N\, p_{ij} - N\, p_i p_j \,\forall\, i \neq j, \tag{7.6}$$

where p_{ij} is the relative probability of the two-dimensional histograms (w, $\cos\theta_\ell$), (w, $\cos\theta_{\rm v}$), (w, χ), ($\cos\theta_\ell$, $\cos\theta_{\rm v}$), (χ, $\cos\theta_\ell$) and (χ, $\cos\theta_{\rm v}$) and p_i and p_j give the relative probability of the one dimensional histograms of w, $\cos\theta_\ell$, $\cos\theta_{\rm v}$ and χ. N is the total size of the sample. The diagonal elements are the variances of $N_i^{\rm exp}$ and are calculated with the following approach,

$$\begin{aligned} C_{i,i} \;=\; & \sum_{i=1}^{40} \Big[R_{ij}^2\, \epsilon_j^2\, N_j^{\rm prod} + R_{ij}^2\, \frac{(1-\epsilon_j)}{N_{\rm data}}\, (N_j^{\rm prod})^2 + R_{ij}\, \frac{(1-R_{ij})}{N'_{\rm data}}\, \epsilon_j^2\, (N_j^{\rm prod})^2 \\ & + R_{ij}^2\, \frac{(1-\epsilon_j)}{N_{\rm MC}}\, (N_j^{\rm prod})^2 + R_{ij}\, \frac{(1-R_{ij})}{N'_{\rm MC}}\, \epsilon_j^2\, (N_j^{\rm prod})^2 \Big] + \sigma^2(N_i^{\rm bkgrd}). \end{aligned} \tag{7.7}$$

This expression takes the Poissonian uncertainty of $N^{\rm prod}$ and $N^{\rm exp}$ in each bin, and the last term of the equation gives the total error associated with the background. The errors from the scale factors of the different background components (including continuum) are added linearly.

7.1.1 Comparison between Theory and MC

Before running the fit for $\mathcal{F}(1)|V_{cb}|$ and the form factor parameters it is important to cross-check our theoretical model against the MC expectation. Both should be equivalent as they are are both based on the CLN parameterisation. Therefore, by setting the values of the form factor parameters in our theory model to the values we have in the MC generator, we should expect a good agreement in distributions of the kinematic variables. In Figure 7.1 the normalised distributions of kinematic variables comparing theory and MC are shown.

Very good agreement is found, suggesting that the generator and analytical approaches are consistent. A small difference is found at large values of w, where the finite mass

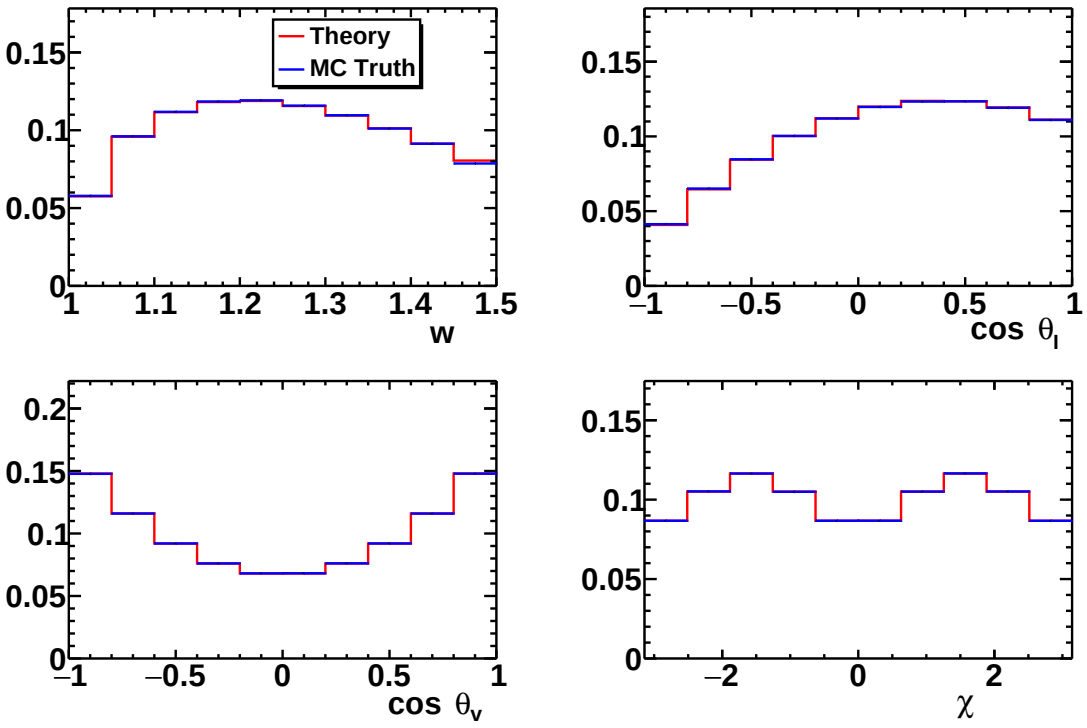

Figure 7.1: Distributions of kinematic variables w, $\cos\theta_\ell$, $\cos\theta_\mathrm{v}$ and χ comparing theory model with MC with $\rho^2 = 1.301$, $R_1(1) = 1.181$, $R_2(1) = 0.710$ for e and μ modes combined [9].

of the muon introduces a potentially measurable difference to the electron mode, shown in Figure 7.2. The analytical approach used in the fit ignores the charged lepton mass. Therefore a bound on the w is set to allow the use of the model that does not account for finite masses. The bin boundaries for the kinematic variables w, $\cos\theta_\ell$, $\cos\theta_v$, χ are chosen within the kinematic allowed limit except for variable w whose maximum value from Equation 3.40 is 1.504 but it is taken to be 1.50 for electrons and 1.49 for muons. The remaining difference in the final muon w bin is much less than 1%.

7.1.2 Detector Response Matrices

The kinematic variables (θ_ℓ, $theta_V$, w, χ) have finite resolution due to detector effects and reconstruction algorithms. This is described in Chapter 6.7.2. This effect leads to bin migration, where true values of the these variables may be reconstructed in one of

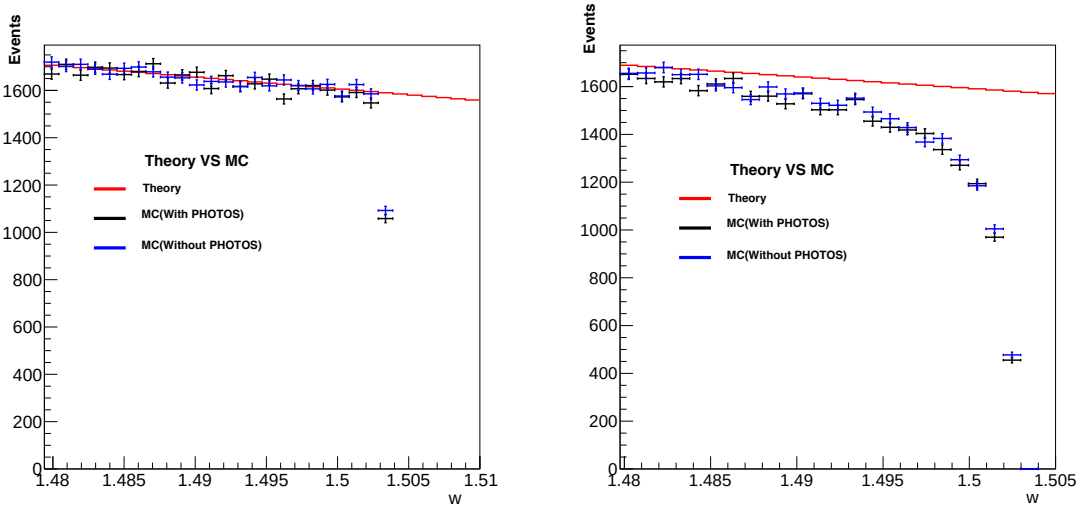

Figure 7.2: The w distribution near the kinematically allowed limit. The figure on left is for the electron mode and figure of right is the muon mode. The red line shows the theoretical model. The blue and black lines are MC predictions with and without considering radiative photons respectively using PHOTOS.

several reconstruction-level bins. The response matrix is hence a two dimensional distribution as a function of the reconstructed and true value of the kinematic variable. The response matrix is calculated from MC where both reconstructed and true values are well known. It is calculated separately for the kinematic variables because the bin migration is only between the truth and reconstruction distribution but no migration between the variables themselves. The response has to be taken into account while calculating the theory prediction in order to include detector effects.

As shown in Table 6.3, the resolution is comparable to the width of the bins such that bin migration is not large. Figures 7.3 and 7.4 show the response matrices for electrons and muons where the x-axis shows reconstructed events and y-axis shows the true events. The matrices are highly diagonal except for χ where resolution is poorer than the other variables.

7.2 Fit Results for $\rho^2, R_1(1), R_2(1)$ & $\mathcal{F}(1)|V_{cb}|$

The fit to the CLN parameterisation is performed for each sub sample. The results for the form factors and $\mathcal{F}(1)|V_{cb}|$ are shown in Table 7.2. The p-valuse of each of the fits is calculated based on the χ^2 per degree of freedom, and it can be seen that all fits have

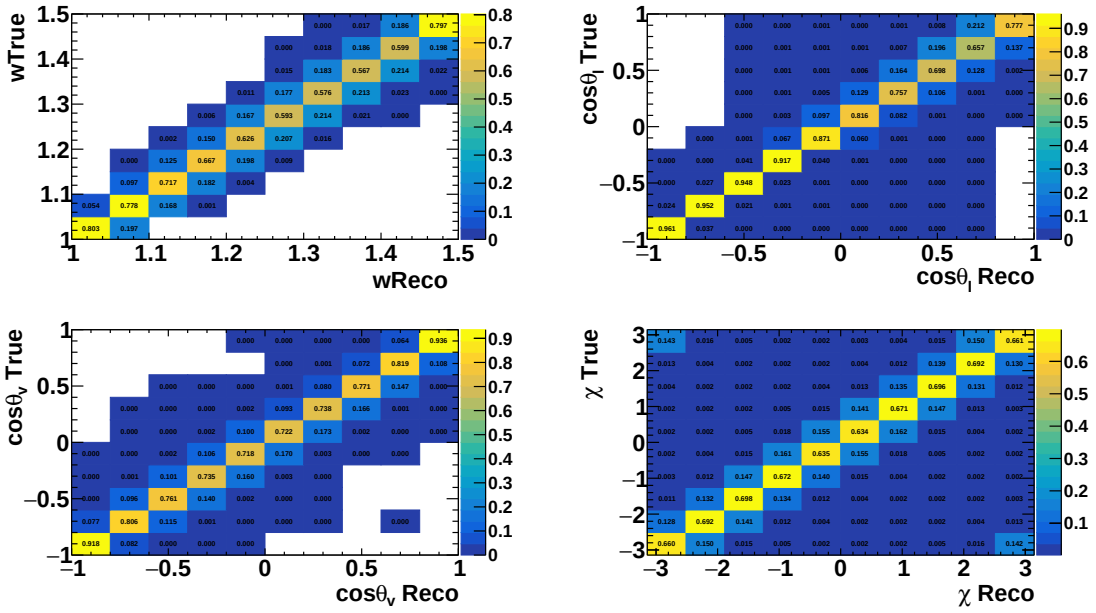

Figure 7.3: Response matrices of four kinematic variables w, $\cos\theta_\ell$, $\cos\theta_\mathrm{v}$ and χ in the e sample.

acceptable values. The results for $\mathcal{F}(1)|V_{cb}|$ are consistent among all samples, as are the branching fractions. The form factors are also quite consistent. Figures 7.5, 7.6, 7.7 and 7.8 are the distributions of the kinematic variable after the fit for four data samples, SVD1(e), SVD1(μ) , SVD2(e), and SVD2(μ) respectively. The linear fit correlation coefficients are given for the four sub-samples in Tables 7.3 to 7.6. There is a high correlation between ρ^2 and $R_2(1)$ but it does not exceed 0.9. The correlation between $\mathcal{F}(1)|V_{cb}|$ and the form factor parameters is reasonable, though highest with ρ^2.

7.2.1 Fit validation

Toy MC samples are performed to validate the fit procedure and compare the parameter values obtained from the fit to the true values of the parameters. The pull for any parameter is defined as

$$\mathrm{pull}_{\mathrm{parameter}} = \frac{\mathrm{fit}^{\mathrm{parameter}} - \mathrm{true}^{\mathrm{parameter}}}{\sigma^{\mathrm{fit}}_{\mathrm{parameter}}}, \tag{7.8}$$

where $\mathrm{fit}^{\mathrm{parameter}}$ is the value of the parameter after the fit and the $\mathrm{true}^{\mathrm{parameter}}$ is the true MC value. A total of 900 toy samples are generated for each sub-sample the using the uncertainty on the number of events in each bin. The distribution is then fitted using

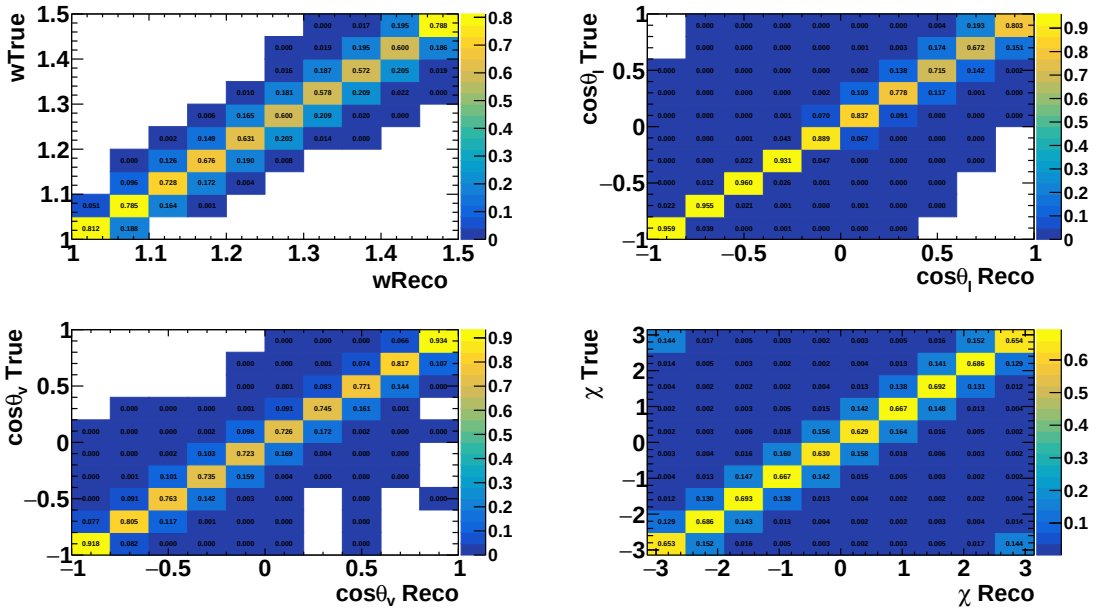

Figure 7.4: Response matrices of four kinematic variables w, $\cos\theta_\ell$, $\cos\theta_\mathrm{v}$ and χ in the μ sample.

ROOT. The pull plots are shown in Figs. 7.9, 7.10, 7.11 and 7.12, and the results from the pull are summarised in Table 7.7. It can been in Table 7.7 that the mean and sigma obtained from the studies are correctly at 0 and 1 respectively. The fitted sigma values for ρ^2 are slightly larger than 1, however this is due to a slightly non-Gaussian distribution of the pull distribution where the Gaussian undershoots the pull in the core.

Table 7.2: Fit Results for the four sub-samples. For reference, the world average values are $\rho^2 = 1.207 \pm 0.028$, $R_1(1) = 1.401 \pm 0.038$, $R_2(1) = 0.854 \pm 0.020$ and $|V_{cb}| = 35.81 \pm 0.11 \times 10^{-3}$.

Variable	**SVD1(e)**	**SVD1(μ)**	**SVD2 (e)**	**SVD2 (μ)**
ρ^2	1.165 ± 0.099	1.165 ± 0.102	1.087 ± 0.046	1.095 ± 0.051
$R_1(1)$	1.326 ± 0.106	1.336 ± 0.102	1.117 ± 0.040	1.289 ± 0.048
$R_2(1)$	0.767 ±0.073	0.777 ± 0.074	0.861 ± 0.030	0.882 ± 0.034
$\mathcal{F}(1)\|V_{cb}\| \times 10^{-3}$	34.66 ± 0.48	35.01 ± 0.50	35.25 ± 0.23	34.98 ± 0.24
χ^2/ndf	35.8/36	36.0/36	44.1/36	43.5/36
p**-Value**	0.48	0.47	0.17	0.18
B.F [%]	4.84 ± 0.06	4.91 ± 0.06	4.88 ± 0.03	4.82 ± 0.03

Table 7.3: Statistical correlation matrix of the fit parameters in the SVD1(e) sample.

	ρ^2	$R_1(1)$	$R_2(1)$	$\mathcal{F}(1)\|V_{cb}\|$
ρ^2	1.000	0.615	-0.887	0.608
$R_1(1)$		1.000	-0.717	-0.100
$R_2(1)$			1.000	-0.215
$\mathcal{F}(1)\|V_{cb}\|$				1.000

Table 7.4: Statistical correlation matrix of the fit parameters in the SVD1(μ) sample.

	ρ^2	$R_1(1)$	$R_2(1)$	$\mathcal{F}(1)\|V_{cb}\|$
ρ^2	1.000	0.617	-0.888	0.625
$R_1(1)$		1.000	-0.706	-0.100
$R_2(1)$			1.000	-0.240
$\mathcal{F}(1)\|V_{cb}\|$				1.000

Table 7.5: Statistical correlation matrix of the fit parameters in the SVD2(e) sample.

	ρ^2	$R_1(1)$	$R_2(1)$	$\mathcal{F}(1)\|V_{cb}\|$
ρ^2	1.000	0.578	-0.882	0.711
$R_1(1)$		1.000	-0.664	-0.010
$R_2(1)$			1.000	-0.338
$\mathcal{F}(1)\|V_{cb}\|$				1.000

Table 7.6: Statistical correlation matrix of the fit parameters in the SVD2(μ) sample.

	ρ^2	$R_1(1)$	$R_2(1)$	$\mathcal{F}(1)\|V_{cb}\|$
ρ^2	1.000	0.551	-0.877	0.714
$R_1(1)$		1.000	-0.645	-0.011
$R_2(1)$			1.000	-0.331
$\mathcal{F}(1)\|V_{cb}\|$				1.000

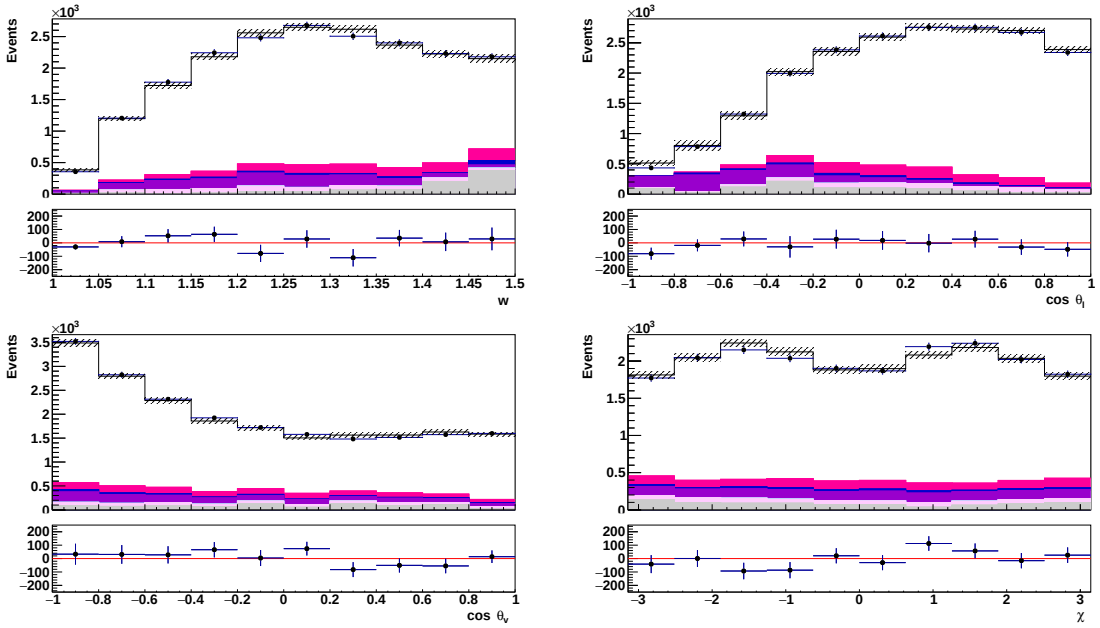

Figure 7.5: Projections of w, $\cos\theta_\ell$ and $\cos\theta_\mathrm{v}$ and χ after the fit to the CLN scheme for data sample SVD1 (e). The colour scheme in Figure. 6.16.

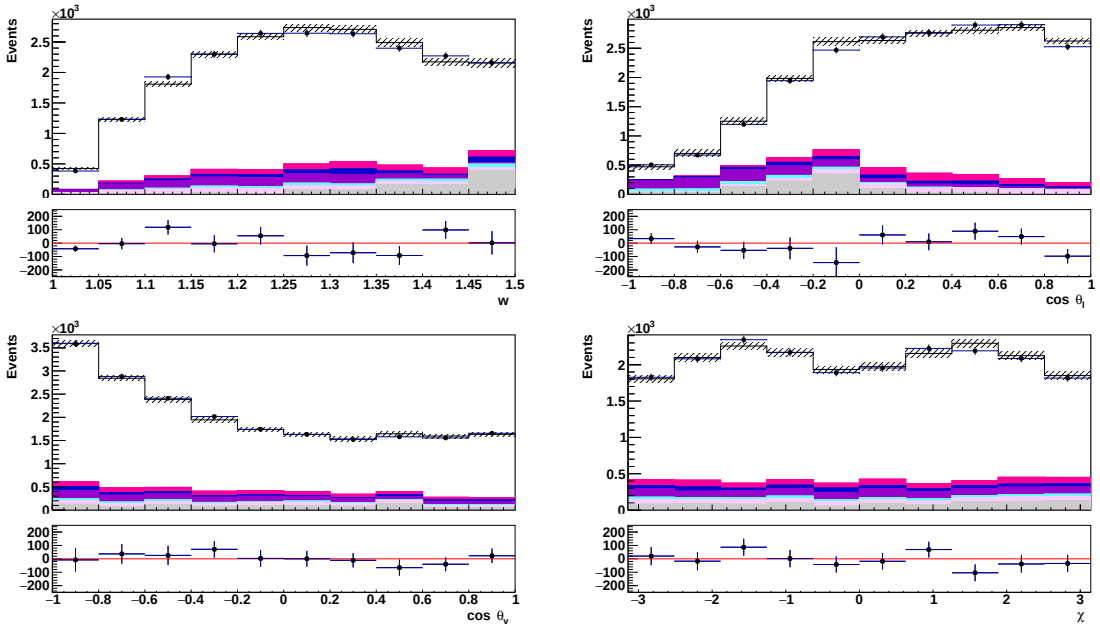

Figure 7.6: Projections of w, $\cos\theta_\ell$ and $\cos\theta_\mathrm{v}$ and χ after the fit to the CLN scheme for data sample SVD1 (μ). The colour scheme in Figure. 6.16.

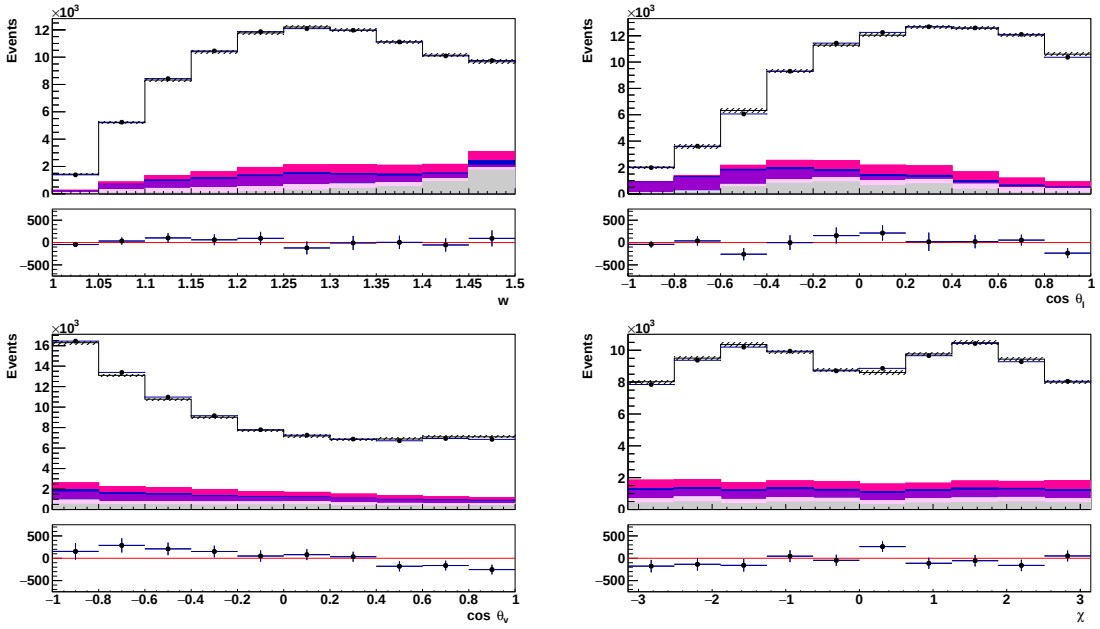

Figure 7.7: Projections of w, $\cos\theta_\ell$ and $\cos\theta_\mathrm{v}$ and χ after the fit to the CLN scheme for data sample SVD2 (e). The colour scheme Figure. 6.16.

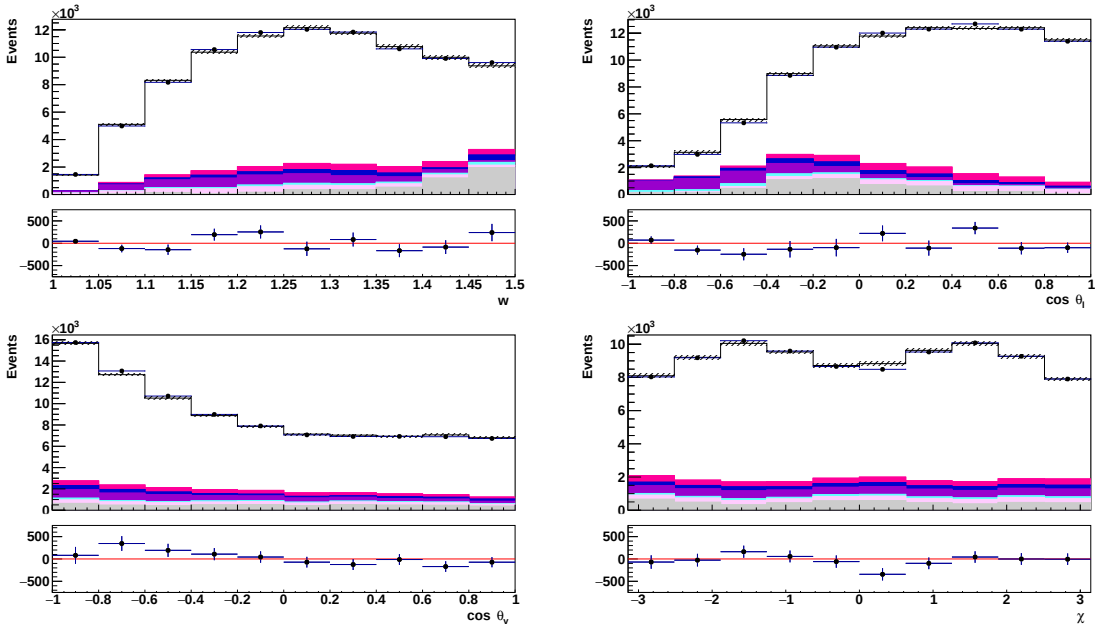

Figure 7.8: Projections of w, $\cos\theta_\ell$ and $\cos\theta_\mathrm{v}$ and χ after the fit to the CLN scheme for data sample SVD2 (μ). The colour scheme 6.16.

Table 7.7: Results from the pull study for the parameters ($\rho^2, R_1(1), R_2(1)$ and $\mathcal{F}(1)|V_{cb}|$)

		SVD1(e)	SVD1(μ)	SVD2(e)	SVD2(μ)
ρ^2	Mean	0.042 ± 0.038	0.015 ± 0.035	-0.007 ± 0.040	0.034 ± 0.037
	Sigma	1.082 ± 0.031	1.035 ± 0.025	1.162 ± 0.030	1.081 ± 0.030
$R_1(1)$	Mean	-0.010 ± 0.035	-0.029 ± 0.033	-0.002± 0.035	0.022 ± 0.035
	Sigma	1.010 ± 0.030	0.945 ± 0.024	1.033 ± 0.024	1.002 ± 0.025
$R_2(1)$	Mean	-0.033 ± 0.035	0.042 ± 0.033	-0.013 ± 0.037	-0.014 ± 0.036
	Sigma	1.019± 0.026	0.932 ± 0.024	1.061± 0.029	1.033 ± 0.025
$\mathcal{F}(1)\|V_{cb}\|$	Mean	0.026 ± 0.033	0.027± 0.034	-0.050 ± 0.038	0.003 ± 0.035
	Sigma	0.968 ± 0.027	0.983 ± 0.025	0.967± 0.025	1.012 ± 0.025

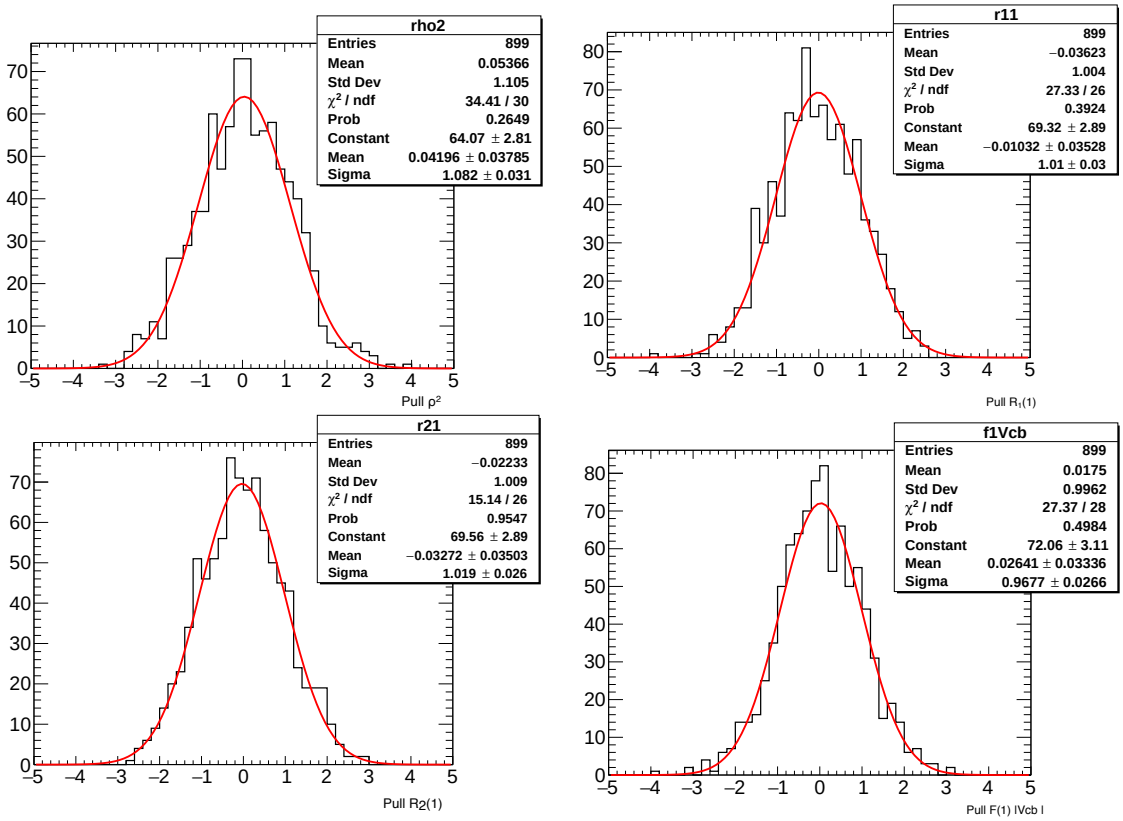

Figure 7.9: Pull distributions for the CLN fit in the SVD1(e) subset.

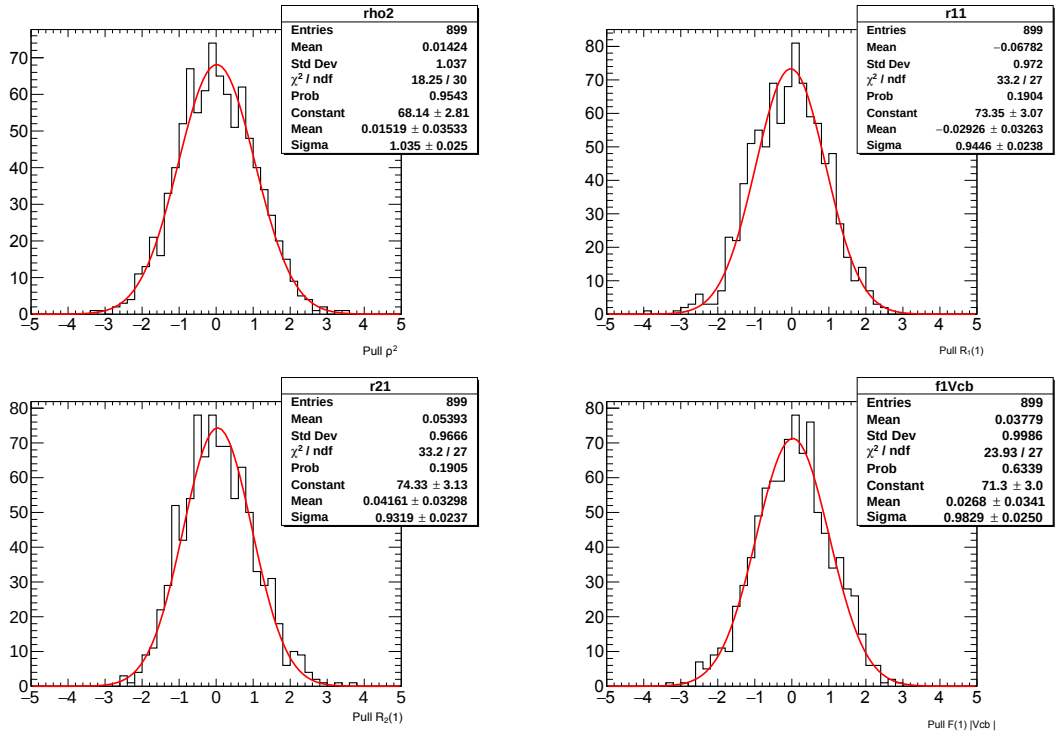

Figure 7.10: Pull distributions for CLN fit in the SVD1(μ) subset.

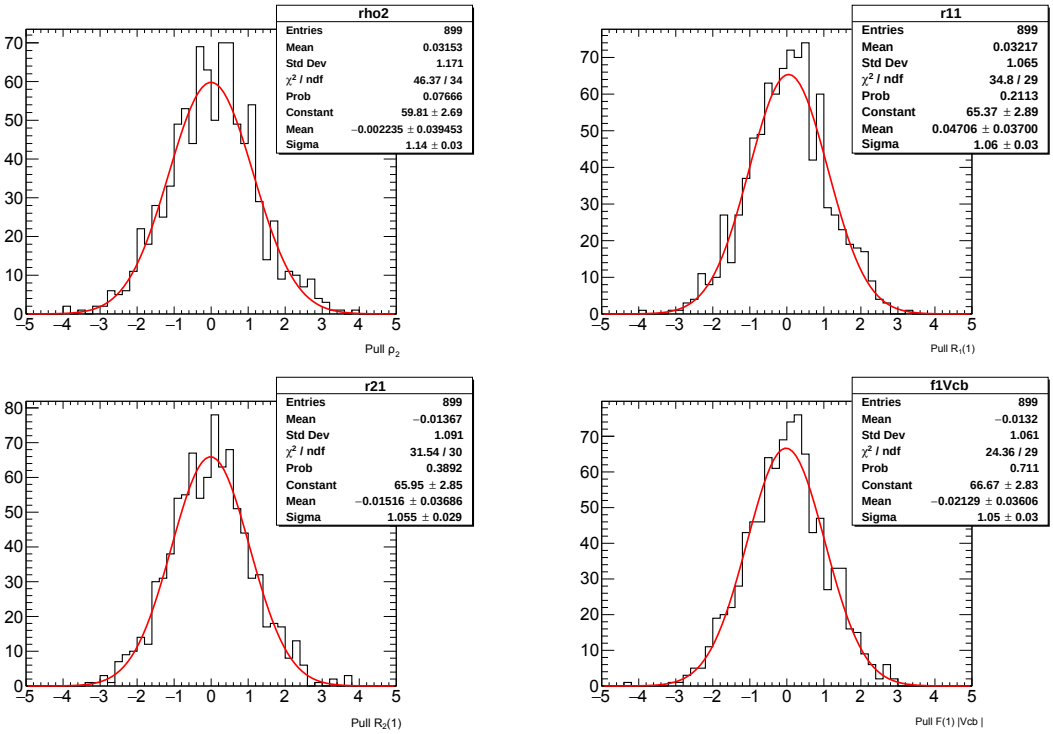

Figure 7.11: Pull distributions for the CLN fit in the SVD2(e) subset.

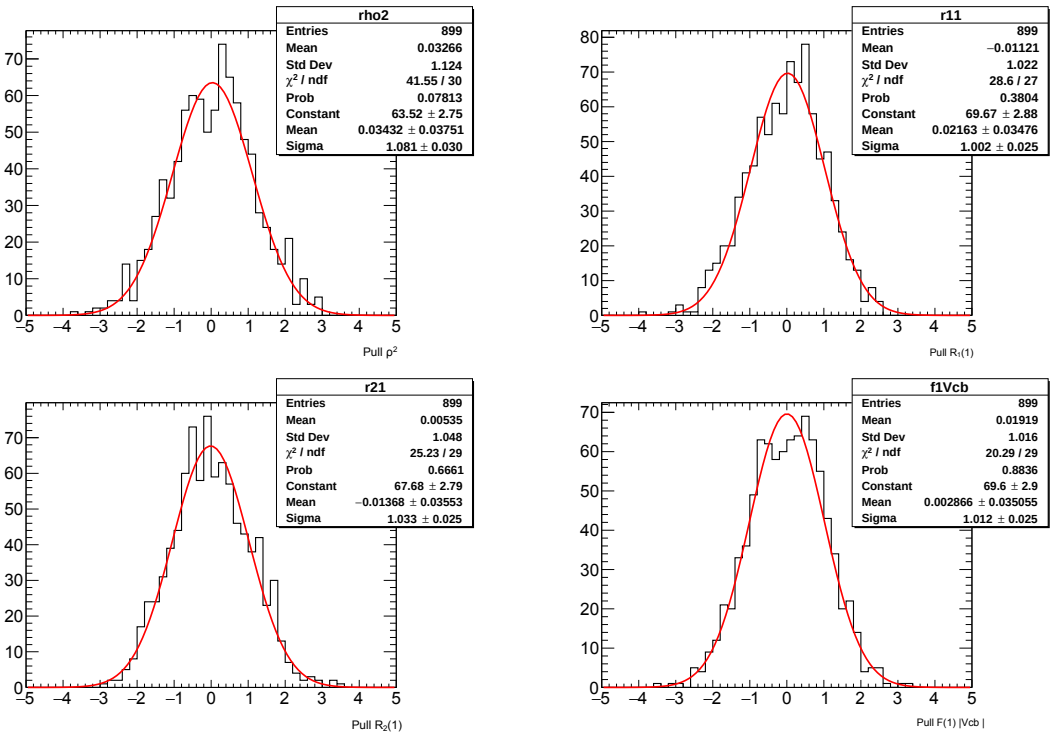

Figure 7.12: Pull distributions for the CLN fit in the SVD2(μ) subset.

8. Systematic Uncertainties and Final CLN results

In the previous chapter, we were able to extract the values of the form factor parameters and $\mathcal{F}(1)|V_{cb}|$ along with the statistical uncertainty associated with them. In this chapter we consider additional sources of uncertainty that are associated with the nature of the measurement, assumptions made in the experiment, or the models used to make inferences based on the observed data. There are number of external sources of errors contributing to the systematic uncertainties.

The systematic uncertainties arises due to following sources:

- tracking efficiencies,
- lepton identification efficiencies,
- lepton fake rate corrections,
- hadron identification efficiencies,
- branching fractions of $\mathcal{B}(D^{*+} \to D^0\pi^+)$ and $\mathcal{B}(D^0 \to K^-\pi^+)$,
- the B^0 life time,
- the total number of $\Upsilon(4S)$ in the data sample,
- the ratio of $B^0\bar{B^0}$ to B^+B^- i.e. $f_{+-}/f_{00} = \mathcal{B}(\Upsilon(4S) \to B^+B^-)/\mathcal{B}(\Upsilon(4S) \to B^0\bar{B}^0)$,
- $B \to D^{**}\ell\nu$ composition, and shape functions as well as D^{**} branching fractions.

Note that the errors from the background fit are already propagated into the fit/statistical uncertainty, as are the uncertainties due to finite MC statistics. The latter are very low due to the use of 10 streams of signal MC.

8.1 Sources of Systematic Uncertainties

8.1.1 High momentum tracking

There are four charged tracks in the decay, two pions and a kaon along with a charged lepton. The track finding uncertainty is calculated for all tracks, except for the slow pion from the D^*. The error associated the slow (pions) tracks are calculated separately. The uncertainty associated with each fast track is a constant 0.35% which is multiplied by the number of fast tracks for signal events due as there is 100% correlation.

8.1.2 Slow pion tracking

The uncertainty associated with slow pion tracking is calculated in bins of slow pion momentum in the lab frame. There are three uncertainties associated with the slow pion efficiency correction, one statistical error and two systematic errors. The systematic errors are correlated and therefore added linearly and the total error is calculated using the quadratic sum of the statistical and systematic errors. The errors are calculated with calibration samples for SVD1 and SVD2 samples separately, and therefore combined in inverse quadrature for the full sample.

8.1.3 Hadron identification

There is a small uncertainty associated to the kaon and pion identification criteria used for the daughters of the D^0 candidates. Due to the use of relatively loose criteria, we find that the efficiencies are very high and with very low uncertainty. It is therefore negligible with respect to other sources of uncertainty.

8.1.4 Lepton Identification

The systematic error due to lepton identification efficiency correction is calculated in bins of lepton momentum in the lab frame, and the lepton polar angle. There are three errors associated with the lepton identification table, one statistical error and two systematic errors. The statistical errors among different bins are independent, while the systematic errors should be considered to be 100% correlated and are added linearly. The systematic uncertainty is calculated for electron and muon modes separately combining the SVD1

and SVD2 samples. The total systematic error due to lepton identification efficiency is calculated by inverse quadrature sum of uncertainty due to electron and muon samples.

8.1.5 Lepton fake rates

There is a small probability that the candidate leptons originate from misidentified hadrons. A calibration sample of $D^* \to D^0$, $D^0 \to K\pi$ was studied to determine this probability with data and correct the MC expectation. The uncertainties associated to the statistical error of this calibration sample are propagated into the analysis. The overall uncertainty is small, as the the overall fake rate is anyway floated in the background fit.

8.1.6 $B \to D^{**}\ell\nu$ Branching Ratios and Form Factors

We account for uncertainties in the $B \to D^{**}\ell\nu$ component. The shapes of the $B \to D^{**}\ell\nu$ q^2 distributions are corrected to match the predictions of the LLSW model [55]. The errors on the branching fractions are varied by $\pm$ two standard deviations for both the B and the D^{**} decays. The errors associated with the LLSW form factor parameters are calculated using the procedure described in Ref. [58].

8.1.7 D^* and D^0 Branching fractions

The systematic uncertainty associated with the $\mathcal{B}(D^{*+} \to D^0\pi^+)$ and $\mathcal{B}(D^0 \to K^-\pi^+)$ corrections are calculated as the relative error on the branching fraction.

8.1.8 B^0 yield in the data sample

The B^0 yield is determined with two input parameters: the measured yield of $\Upsilon(4S)$ in the data sample, and the fraction of those $\Upsilon(4S)$ that decay to a $B^0/\bar{B}^0$ pair. The former is measured by the Belle collaboration using the number of hadronic events on and off-resonance and taking the difference. The latter is taken from the world average measurement of the $\Upsilon(4S)$ branching ratio, which is 48.6 ± 1.4 %.

8.1.9 Calculation of Systematics Uncertainties using Toy Samples

We estimate systematic uncertainties by varying each possible uncertainty source such as the PDF shape and the signal reconstruction efficiency with the assumption of a Gaussian error, unless otherwise stated. This is done via sets of pseudo-experiments in which each independent systematic uncertainty parameter is randomly varied using a normal distribution. The entire analysis is repeated for each pseudo-experiment and the spread on each measured observable is taken as the systematic error. This approach also provides the necessary information to determine the systematic uncertainty correlations between each measured observable.

It should be noted that the uncertainties due to fast track reconstruction, number of $\Upsilon(4S)$ in the data sample, $\mathcal{B}(D^{*+} \to D^0\pi_s^+)$,$\mathcal{B}(D^0 \to K\pi)$ and B^0 life time does not effect the form factor parameters.

The breakdown of the systematic error is tabulated in Table 8.1. The total uncertainty is determined from the quadratic sum of all uncertainties.

8.2 Results

The final results combining the subsample results through a weighted average are presented with their respective total statistical and systematic errors are shown in Table 8.2. The value of $\mathcal{F}(1)|V_{cb}| \times 10^{-3}\eta_{\rm EW}$ is found to be less than one standard deviation from the world average, $35.6 \pm 0.1 \pm 0.4$, as is $\mathcal{B}(B^0 \to D^{*-}\ell^+\nu_\ell)$, where the world average is $4.88 \pm 0.01 \pm 0.10$. This work is the most precise evaluation of these quantities to date.

8.3 Lepton flavour universality

After calculating $\mathcal{B}(B^0 \to D^{*-}\ell^+\nu_\ell)$ for both electrons and muons, their respective ratio can be determined. In this ratio most of the systematic uncertainties cancel, with the exception of those associated to lepton identification. This is a very stringent test of lepton flavour universality, showing excellent agreement with unity.

The branching fractions for the electron and muon modes, and their statistical uncer-

Table 8.1: Systematic uncertainty breakdown for $|V_{cb}|$, branching fraction and form factor parameters in the CLN form factor parameterisation. The lepton ID uncertainties are given for the e and μ subsets as well as the combined value.

Systematic Uncertainties	ρ^2	$R_1(1)$	$R_2(1)$	$\mathcal{F}(1)\lvert V_{cb}\rvert$ [%]	B.F. [%]
Slow pion efficiency	0.005	0.002	0.001	0.65	1.29
Lepton ID (e)-sample	0.016	0.026	0.016	0.78	1.49
Lepton ID (μ)-sample	0.001	0.006	0.004	1.13	2.28
Lepton ID combined	0.001	0.006	0.004	0.68	1.38
$\mathcal{B}(B \to D^{**}\ell\nu)$	0.002	0.001	0.002	0.26	0.52
$B \to D^{**}\ell\nu$ Form factors	0.003	0.001	0.004	0.10	0.22
f_{+-}/f_{00}	0.001	0.002	0.002	0.52	1.06
Fake e/μ	0.004	0.006	0.001	0.11	0.21
Norm. continuum	0.002	0.002	0.001	0.01	0.06
Fast track efficiency	-	-	-	0.53	1.05
N($\Upsilon(4S)$)	-	-	-	0.68	1.37
B^0 life time	-	-	-	0.13	0.26
$\mathcal{B}(D^{*+} \to D^0\pi_s^+)$	-	-	-	0.37	0.74
$\mathcal{B}(D^0 \to K\pi)$	-	-	-	0.51	1.02
Total Systematic Error	0.008	0.009	0.007	1.55	3.11

tainties are as follows.

$$\mathcal{B}(B^0 \to D^{*+}e^-\nu) = (4.87 \pm 0.03)\%$$

$$\mathcal{B}(B^0 \to D^{*+}\mu^-\nu) = (4.84 \pm 0.03)\%$$

The ratio of branching fractions for (e/μ) is calculated as follows:

$$\mathcal{B}(B^0 \to D^{*+}\ell^-\nu) = \frac{\mathrm{N}_{\text{signals after fit}}}{\epsilon \times \mathcal{B}(D^{*+} \to D^0\pi_s) \times \mathcal{B}(D^0 \to K\pi) \times N_{B^0}}.$$

The results for the lepton flavour universality test are as follows.

$$\mathcal{R}_{e/\mu} = \frac{\mathcal{B}(B^0 \to D^{*+}e^-\nu_e)}{\mathcal{B}(B^0 \to D^{*+}\mu^-\nu_\mu)} = 1.01 \pm 0.01 \pm 0.03.$$

Table 8.2: Results for the full sample in the CLN scheme.

Parameters	**Values**
ρ^2	$1.106 \pm 0.031 \pm 0.008$
$R_1(1)$	$1.229 \pm 0.028 \pm 0.009$
$R_2(1)$	$0.852 \pm 0.021 \pm 0.007$
$\mathcal{F}(1)\lvert V_{cb}\rvert \times 10^{-3}\eta_{\rm EW}$	$35.1 \pm 0.2 \pm 0.5$
$\mathcal{B}(B^0 \to D^{*-}\ell^+\nu_\ell)$	$(4.86 \pm 0.02 \pm 0.15)\%$

9. Fit for $\mathcal{F}(1)|V_{cb}|$ in the BGL scheme

To perform the fit to the BGL parameterisation we follow the approach described in Ref. [59]. We similarly truncate the series in the expansion for a_f and a_g terms at $\mathcal{O}(z^2)$ and order $\mathcal{O}(z^3)$ for F_1. This results in five free parameters (one more than in the CLN fit), defined as $\tilde{a}_i^f = |V_{cb}|\eta_{\rm EW}\ a_i^f$, and $\tilde{a}_i^g = |V_{cb}|\eta_{\rm EW} a_i^g$ where $i = 0, 1$ and $\tilde{a}_i^{F_1} = |V_{cb}|\eta_{\rm EW}\ a_i^{F_1}$, where $i = 1, 2$. This number of free parameters can describe the data well, while higher order terms will not be well constrained unless additional information from lattice is introduced. We found that there can be very high correlations (much greater than 90%) in the six-parameter fit between $\tilde{a}_0^g$ and $\tilde{a}_1^g$, and decided therefore not to use the second order in the a_i^g term. We apply a unitarity bound as in Ref. [59], and described in Chapter 3.

We perform a χ^2 fit to the data with the same procedure as for the CLN fit described in Chapter 8. The resulting value for $|V_{cb}|$ is larger than that from the CLN parameterisation, and consistent with the inclusive approach. The fit results are given in Table 9.1 and Fig. 9.1. Correlations are generally high in this fit approach, and would greatly benefit from further LQCD points away from zero recoil. For this reason it was not possible to reliably fit the SVD1 subsets, and instead the combined SVD1 and SVD2 samples are fit. We find very good agreement for $|V_{cb}|$ in in the electron and muon modes. The fit correlation matrices are given in Table 9.3 and Table 9.4 for electron and muon modes respectively.

Table 9.2 shows the results for the combination of the electron and muon modes. Finally the systematic uncertainties are evaluated with the same procedure as described in Chapter 8.

The result for $\mathcal{F}(1)|V_{cb}|\eta_{\rm EW}$ is 10% larger in the BGL than in the CLN approach, and with a larger uncertainty owing to the larger number of free parameters. Both sets of fits give acceptable χ^2/ndf for the data-subsets, however the BGL fit does have better agreement with the data over the full data set. The larger expected result from BGL was

Table 9.1: Fit Results for the electron and muon sub-samples in the BGL parameterisation where the following parameters are floated:$\tilde{a}_0^f$, $\tilde{a}_1^f$, $\tilde{a}_1^{F_1}$, $\tilde{a}_2^{F_1}$, $\tilde{a}_0^g \times 10^2$ along with $\mathcal{F}(1)|V_{cb}|\eta_{\rm EW} \times 10^3$. The $p-$value corresponds to the χ^2/ndf using the statistical errors only.

	e	μ
$\tilde{a}_0^f \times 10^2$	0.0566 ± 0.0005	0.0561 ± 0.0006
$\tilde{a}_1^f \times 10^2$	0.0758 ± 0.0243	0.0644 ± 0.0281
$\tilde{a}_1^{F_1} \times 10^2$	0.0264 ± 0.0010	0.0288 ± 0.0106
$\tilde{a}_2^{F_1} \times 10^2$	0.2771 ± 0.1866	0.3712 ± 0.2078
$\tilde{a}_0^g \times 10^2$	0.0963 ± 0.0027	0.1110 ± 0.0031
$\mathcal{F}(1)\|V_{cb}\|\eta_{\rm EW} \times 10^3$	38.89 ± 0.34	38.56 ± 0.38
χ^2/ndf	57/35	40/35
p-value	0.01	0.26

also seen in studies in Refs. [59] and [2].

Taking the value of $\mathcal{F}(1) = 0.906 \pm 0.013$ from Lattice QCD [12] and $\eta_{\rm EW} = 1.0066$ from [32], we find the following values for $|V_{cb}|$: $(42.5 \pm 0.3 \pm 0.7 \pm 0.6) \times 10^{-3}$ (BGL+LQCD). Note that we round to one significant figure in the final result.

Table 9.2: Combined results for the full data set in the BGL scheme. Note that the precision on $\mathcal{F}(1)|V_{cb}|\eta_{\rm EW} \times 10^3$ is rounded to one decimal place.

Parameters	Values
$\tilde{a}_0^f \times 10^2$	0.0564 ± 0.0004
$\tilde{a}_1^f \times 10^2$	0.0701 ± 0.0183
$\tilde{a}_1^{F_1} \times 10^2$	0.0276 ± 0.0071
$\tilde{a}_2^{F_1} \times 10^2$	0.3242 ± 0.1388
$\tilde{a}_0^g \times 10^2$	0.1037 ± 0.0020
$\mathcal{F}(1)\|V_{cb}\|\eta_{\rm EW} \times 10^3$	38.7 ± 0.3

Table 9.3: Statistical correlation matrix of the BGL fit parameters in the (e) sample.

	$\tilde{a}_0^f$	$\tilde{a}_1^f$	$\tilde{a}_1^F$	$\tilde{a}_2^F$	$\tilde{a}_0^g$
774 $\tilde{a}_0^f$	1.000	-0.803	-0.774	0.668	-0.035
$\tilde{a}_1^f$		1.000	0.486	-0.425	-0.377
$\tilde{a}_1^F$			1.000	-0.981	0.062
$\tilde{a}_2^F$				1.000	-0.050
$\tilde{a}_0^g$					1.000

Table 9.4: Statistical correlation matrix of the BGL fit parameters in the (μ) sample.

	$\tilde{a}_0^f$	$\tilde{a}_1^f$	$\tilde{a}_1^F$	$\tilde{a}_2^F$	$\tilde{a}_0^g$
$\tilde{a}_0^f$	1.000	-0.776	-0.773	0.667	-0.041
$\tilde{a}_1^f$		1.000	0.458	-0.398	-0.440
$\tilde{a}_1^F$			1.000	-0.981	0.080
$\tilde{a}_2^F$				1.000	-0.067
$\tilde{a}_0^g$					1.000

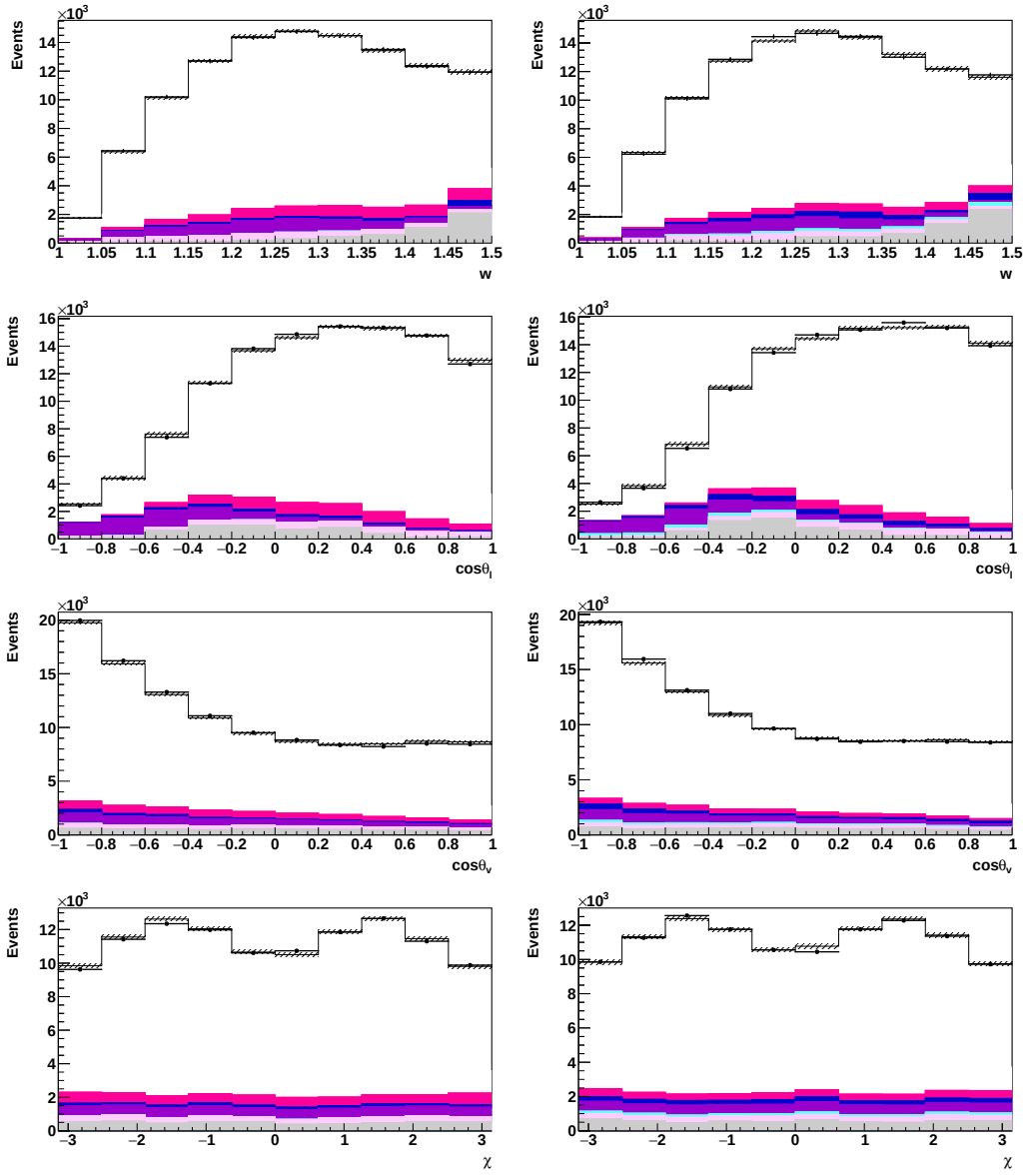

Figure 9.1: Results of the fit with the BGL form factor parameterisation. The results from the SVD1 and SVD2 samples are added together. The electron modes are on the left and muon modes on the right. The points with error bars are the on-resonance data. Where not shown, the uncertainties are smaller than the black markers. The histograms are, top to bottom, the signal component, $B \to D^{**}$ background, signal correlated background, uncorrelated background, fake ℓ component, fake D^* component and continuum.

10. Conclusion

In this thesis we present a new study with data from the Belle experiment of the decay $B \to D^* \ell \nu$. We present the most precise measurement of $|V_{cb}|$ from exclusive decays, and the first direct measurement using the BGL parameterisation. The theoretically favourable BGL parameterisation gives a higher value for $|V_{cb}|$, which is closer to that expected from the inclusive approach [60, 61, 62]. This may be the solution to the long standing tension. This result has implications for semileptonic decay modelling in other studies, such as the measurements of $|V_{ub}|$, and $\mathcal{B}(\mathcal{B} \to \mathcal{D}^{(*)}\tau\nu)$.

We find the following values for $|V_{cb}|$:

$$|V_{cb}| = (38.7 \pm 0.2 \pm 0.6 \pm 0.5) \times 10^{-3} \quad (\text{CLN} + \text{LQCD}) \text{ and} \tag{10.1}$$

$$|V_{cb}| = (42.5 \pm 0.3 \pm 0.7 \pm 0.6) \times 10^{-3} \quad (\text{BGL} + \text{LQCD}). \tag{10.2}$$

We also place stringent bounds on lepton flavour universality violation between electron and muon channels, which has been observed to be consistent with unity.

$$\frac{\mathcal{B}(B^0 \to D^{*+} e^- \nu_e)}{\mathcal{B}(B^0 \to D^{*+} \mu^- \nu_\mu)} = 1.01 \pm 0.01 \pm 0.03 \tag{10.3}$$

The fit with the BGL parameterisation gave p-values that were very good, suggesting a SM description of this decay is most suitable. Limits on new phenomena, such as right handed currents described in this thesis, can be placed using the spectra measured in this thesis and will be the subject of future work.

Bibliography

[1] G. Isidori. Flavour Physics and Implication for New Phenomena. *Adv. Ser. Direct. High Energy Phys.*, 26:339–355, 2016.

[2] D. Bigi et al. A fresh look at the determination of $|V_{cb}|$ from $B \to D^* \ell \nu$. *Phys. Lett.*, B769:441–445, 2017.

[3] *KEKB ring*. Available at `http://belle.kek.jp/belle/slides/KEKB/Bellering4.gif`.

[4] A. Abashian et al. The Belle Detector. *Nucl. Instrum. Meth.*, A479:117–232, 2002.

[5] H. Aihara et al. Status and upgrade plans of the Belle silicon vertex detector. *Nucl. Instrum. Meth.*, A582:709–713, 2007.

[6] S. Uno. The belle central drift chamber. *Nuclear Instruments and Methods in Physics Research Section A: Accelerators, Spectrometers, Detectors and Associated Equipment*, 379(3):421 – 423, 1996. Proceedings of the Sixth International Conference on Instrumentation for Experiments at e^+e^- Colliders.

[7] T. Sumiyoshi et al. Silica aerogel Cherenkov counter for the KEK B factory experiment. *Nucl. Instrum. Meth.*, A433:385–391, 1999.

[8] L.Hinz. Lepton ID efficiency correction and systematic error. *Belle Note.954*, 2006.

[9] B. Aubert et al. Measurement of the $\overline{B}^0 \to D^{*+} \ell^- \bar{\nu}_\ell$ decay rate and $|V_{cb}|$. *Phys. Rev.*, D71:051502, 2005.

[10] I. Bigi and A. I. Sanda. CP violation. 2000. [Camb. Monogr. Part. Phys. Nucl. Phys. Cosmol.9,1 (2009)].

[11] L. Wolfenstein. Parametrization of the Kobayashi-Maskawa Matrix. *Phys. Rev. Lett*, 51, 1945 (1983).

[12] J. A. Bailey et al. Update of $|V_{cb}|$ from the $\bar{B} \to D^* \ell \bar{\nu}$ form factor at zero recoil with three-flavor lattice QCD. *Phys. Rev.*, D89(11):114504, 2014.

[13] C. Patrignani et al. Review of Particle Physics. *Chin. Phys.*, C40(10):100001, 2016.

[14] M. A. Shifman. Quark hadron duality. In *At the frontier of particle physics. Handbook of QCD. Vol. 1-3*, pages 1447–1494, Singapore, 2001. World Scientific, World Scientific. [3,1447(2000)].

[15] M. Lavelle and M. Oleszczuk. The Operator product expansion of the QCD propagators. *Mod. Phys. Lett.*, A7:3617–3630, 1992.

[16] D. J. Gross and F. Wilczek. Ultraviolet behavior of non-abelian gauge theories. *Phys. Rev. Lett.*, 30:1343–1346, Jun 1973.

[17] H. D. Politzer. Asymptotic freedom: An approach to strong interactions. *Physics Reports*, 14(4):129 – 180, 1974.

[18] C-W Xiao et al. Hidden charm states with heavy quark spin symmetry in the local hidden gauge approach. *PoS*, Hadron2013:056, 2013.

[19] N. Isgur and M. B. Wise. WEAK TRANSITION FORM-FACTORS BETWEEN HEAVY MESONS. *Phys. Lett.*, B237:527–530, 1990.

[20] E. Eichten and B. Hill. An effective field theory for the calculation of matrix elements involving heavy quarks. *Physics Letters B*, 234(4):511 – 516, 1990.

[21] N. Isgur. Exclusive versus inclusive semileptonic anti-B decays in the quark model. *Phys. Rev.*, D54:5896–5898, 1996.

[22] I. I. Bigi, M. A. Shifman, N. G. Uraltsev, and A. I. Vainshtein. Pole mass of the heavy quark: Perturbation theory and beyond. *Phys. Rev. D*, 50:2234–2246, Aug 1994.

[23] C. Bourrely, B. Machet, and E. de Rafael. Semileptonic decays of pseudoscalar particles and short-distance behaviour of quantum chromodynamics. *Nuclear Physics B*, 189(1):157 – 181, 1981.

[24] C. G. Boyd, B. Grinstein, and R. F. Lebed. Precision corrections to dispersive bounds on form-factors. *Phys. Rev.*, D56:6895–6911, 1997.

[25] I. Caprini, L. Lellouch, and M. Neubert. Dispersive bounds on the shape of $B^0 \to D^{*-}\ell^+\nu_\ell$. *Nucl. Phys.*, B530:153–181, 1998.

[26] V. M. Braun. Light cone sum rules. In *Progress in heavy quark physics. Proceedings, 4th International Workshop, Rostock, Germany, September 20-22, 1997*, pages 105–118, 1997.

[27] N. Isgur and M. B. Wise. Weak Decays of Heavy Mesons in the Static Quark Approximation. *Phys. Lett.*, B232:113–117, 1989.

[28] M. Neubert. Heavy quark effective theory and weak matrix elements. In Daniel Lellouch, Giora Mikenberg, and Eliezer Rabinovici, editors, *International Europhysics Conference on High Energy Physics*, pages 243–268, Berlin, Heidelberg, 1999. Springer Berlin Heidelberg.

[29] A. Sirlin. Large $m(W)$, $m(Z)$ behaviour of the $\mathcal{O}(\alpha)$ corrections to semileptonic processes mediated by W. *Nuclear Physics B*, 196(1):83 – 92, 1982.

[30] M. Neubert. Heavy quark symmetry. *Phys. Rept.*, 245:259–396, 1994.

[31] P. Abreu et al. Performance of the DELPHI detector. *Nucl. Instrum. Meth.*, A378:57–100, 1996.

[32] R. A. Briere et al. Improved measurement of $|V_{cb}|$ using $\bar{B} \to D^*\ell\nu$ decays. *Phys. Rev. Lett.*, 89:081803, 2002.

[33] J. Abdallah et al. Measurement of |V(cb)| using the semileptonic decay anti-B0(d) —> D*+ l- anti-nu(l). *Eur. Phys. J.*, C33:213–232, 2004.

[34] Bernard Aubert et al. Determination of the form-factors for the decay $B^0 \to D^{*-}\ell^+\nu_l$ and of the CKM matrix element $|V_{cb}|$. *Phys. Rev.*, D77:032002, 2008.

[35] Bernard Aubert et al. Measurement of the Decay $B^- \to D^{*0}e\nu$. *Phys. Rev. Lett.*, 100:231803, 2008.

[36] Bernard Aubert et al. Measurements of the Semileptonic Decays $\bar{B} \to D\ell\nu$ and $\bar{B} \to D^*\ell\nu$ Using a Global Fit to $DX\ell\nu$ Final States. *Phys. Rev.*, D79:012002, 2009.

[37] W. Dungel et al. Measurement of the form factors of the decay $B^0 \to D^{*-}\ell^+\nu_\ell$ and determination of the CKM matrix element $|V_{cb}|$. *Phys.Rev.*, D82:112007, 2010.

[38] A. Abdesselam et al. Precise determination of the CKM matrix element $|V_{cb}|$ with $\bar{B}^0 \to D^{*+}\,\ell^-\,\bar{\nu}_\ell$ decays with hadronic tagging at Belle. 2017.

[39] A. Crivellin and S. Pokorski. Can the differences in the determinations of V_{ub} and V_{cb} be explained by New Physics? *Phys. Rev. Lett.*, 114(1):011802, 2015.

[40] A. Datta, M. Duraisamy, and D. Ghosh. Diagnosing new physics in $b \to c\tau\nu_\tau$ decays in the light of the recent babar result. *Phys. Rev. D*, 86:034027, Aug 2012.

[41] A. Rashed, M. Duraisamy, and A. Datta. Nonstandard interactions of tau neutrino via charged Higgs and W' contribution. *Phys. Rev.*, D87(1):013002, 2013.

[42] A. Crivellin. Effects of right-handed charged currents on the determinations of $|V_{ub}|$ and $|V_{cb}|$. *Phys. Rev.*, D81:031301, 2010.

[43] A. J. Bevan et al. The Physics of the B Factories. *Eur. Phys. J.*, C74:3026, 2014.

[44] S. Kurokawa and E. Kikutani. Overview of the kekb accelerators. *Nuclear Instruments and Methods in Physics Research Section A: Accelerators, Spectrometers, Detectors and Associated Equipment*, 499(1):1 – 7, 2003. KEK-B: The KEK B-factory.

[45] *KEKB/Belle integrated luminosity reached 1000, 2009.* Available at `http://legacy.kek.jp/intra-e/press/2009/KEKBluminosity3.html`.

[46] T. Kawasaki. The Belle silicon vertex detector. *Nucl. Instrum. Meth.*, A494:94–101, 2002.

[47] H. Kichimi et al. The BELLE TOF system. *Nucl. Instrum. Meth.*, A453:315–320, 2000.

[48] D. J. Lange. The EvtGen particle decay simulation package. *Nucl. Instrum. Meth.*, A462:152–155, 2001.

[49] T. Sjostrand, S. Mrenna, and P. Z. Skands. PYTHIA 6.4 Physics and Manual. *JHEP*, 05:026, 2006.

[50] R. Brun, F. Bruyant, M. Maire, A. C. McPherson, and P. Zanarini. *GEANT 3: user's guide Geant 3.10, Geant 3.11; rev. version.* CERN, Geneva, 1987.

[51] R. Itoh. BASF - BELLE AnalysiS Framework. In *Proceedings, 9th International Conference on Computing in High-Energy Physics (CHEP 1997): Berlin, Germany, April 7-11, 1997*, 1997.

[52] K. Abe et al. Measurement of inclusive production of neutral pions from $\Upsilon(4S)$ decays. *Phys. Rev.*, D64:072001, 2001.

[53] *Belle lepton identification table.* Available at `http://belle.kek.jp/group/pid_joint/lid/final/caseB/eid_data-mc_corr_exp31-65-caseB.dat`.

[54] W. Dungel. Systematic investigation of the reconstruction efficiency of low momentum $\pi^{\pm}$ and π^0. *Belle Note.1176*, 2011.

[55] A. K. Leibovich, Z. Ligeti, I. W. Stewart, and M. B. Wise. Semileptonic B decays to excited charmed mesons. *Phys. Rev.*, D57:308–330, 1998.

[56] R. J. Barlow and C. Beeston. Fitting using finite Monte Carlo samples. *Comput. Phys. Commun.*, 77:219–228, 1993.

[57] S. Aoki et al. Review of lattice results concerning low-energy particle physics. *Eur. Phys. J.*, C77(2):112, 2017.

[58] Ch. Oswald, J. Hasenbusch, P. Urquijo, and J. Dingfelder. Modelling of Semileptonic B decays. *Belle Note.1335*, 2014.

[59] B. Grinstein and A. Kobach. Model-Independent Extraction of $|V_{cb}|$ from $\bar{B} \to D^* \ell \overline{\nu}$. *Phys. Lett.*, B771:359–364, 2017.

[60] C. Schwanda et al. Moments of the hadronic invariant mass spectrum in $b \to X_c l \nu$ decays at belle. *Phys. Rev. D*, 75:032005, Feb 2007.

[61] H. Na, C. M. Bouchard, G. P. Lepage, C. Monahan, and J. Shigemitsu. $B \to Dl\nu$ form factors at nonzero recoil and extraction of $|V_{cb}|$. *Phys. Rev.*, D92(5):054510, 2015. [Erratum: Phys. Rev.D93,no.11,119906(2016)].

[62] Giulia Ricciardi. Status of $|V_{cb}|$ and $|V_{ub}|$ CKM matrix elements. *AIP Conf. Proc.*, 1701:050014, 2016.